A slurry model of the F-layer in the Earth's core

Jenny Wong

Submitted in accordance with the requirements for the degree of

Doctor of Philosophy

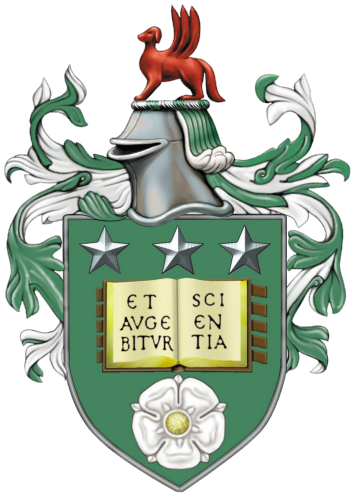

Centre for Doctoral Training in Fluid Dynamics

University of Leeds

November 2018

The candidate confirms that the work submitted is their own, except where work which has formed part of jointly authored publications has been included. The contribution of the candidate and the other authors to this work has been explicitly indicated below. The candidate confirms that appropriate credit has been given within the thesis where reference has been made to the work of others.

Chapters 2, 3 and 6 contain material from the jointly authored publication:

> **Wong, J. , Davies, C.J. , and Jones, C.A.** (2018).
> A Boussinesq slurry model of the F-layer at the base of Earth's outer core, *Geophysical Journal International*, 214(3), 2236 – 2249.

Jenny Wong contributed the code, conducted the simulations and wrote the article. Chris Davies and Chris Jones undertook advisory roles.

"Many cosmogonists now maintain that the Earth was originally cold and has been heating by radioactivity ever since. But I think, as I have said, that some important facts cannot be explained without a fluid stage."
Sir Harold Jeffreys

Acknowledgements

There are many people I would like to thank for their unwavering support and belief in me during my studies. Firstly, I would like to thank my supervisor Chris Davies for his never-ending energy and passion for geophysics that helped expand my scientific horizons. Secondly, I would like thank my co-supervisor Chris Jones for his good humour and incisive advice that always kept me inspired and on the right track.

I am grateful to the EPSRC Centre for Doctoral Training for funding my studies, as well as providing an excellent environment to work in. My thanks go to my colleagues for their shared knowledge and conviviality, to the centre manager, Claire Savy, for there would be chaos without her, and to Peter Jimack and the management team for steering the ship.

It has been a privilege to work at a top-class university such as Leeds where I am able to meet brilliant academics, from the Deep Earth research group in the School of Earth and Environment, to the fluid dynamics seminars delivered by world-leading researchers hosted by the School of Mathematics. I am grateful for funding from SEDI and IPGP to aid with travel to conferences in Canada and France. I would also like to thank Thierry Alboussière, Renaud Deguen, Stéphane Labrosse, and everyone at LGL-TPE for their hospitality during my research placement in Lyon.

I have made my home in Leeds for almost a decade and I have many fond memories shared with friends, old and new. Leeds is also the place where I met Tom, whom I could never thank enough for all his love. Finally, I would like to thank my family: Mum, Dad, Richard, Elise, and Riley, for their incredible support. I dedicate this work to my parents for the great sacrifices they have made for me. I hope I did them proud.

Abstract

Seismic observations suggest that a stably-stratified layer, known as the F-layer, 150–300 km thick exists at the base of Earth's liquid outer core. This contrasts with the density inferred from the Preliminary Reference Earth Model, which assumes a well–mixed and adiabatic outer core. The liquid core is composed primarily of iron alloyed with a light component. We propose that the layer can be explained by a slurry on the liquidus, whereby solid particles of iron crystallise from the liquid alloy throughout the layer. The slurry model provides a dynamically consistent explanation of how light element can pass through a stable layer.

We make two key assumptions, the first of which is fast-melting where the time-scale of freezing is considered short compared to the evolution of the F-layer. The second assumption is that we consider a binary alloy where the light element is purely composed of oxygen, which is expelled entirely into the liquid during freezing.

We present an idealised steady state model of a slurry, where temperature, light element concentration and solid flux profiles are ascertained for various layer thicknesses, inner core heat fluxes and values of the core thermal conductivity, since there is some uncertainty in these parameters. Our solutions demonstrate that the steady state slurry can satisfy the geophysical constraints on the density jump across the layer and the core-mantle boundary heat flux.

A time-dependent model is presented, in which the slurry system is coupled to the evolving global heat balance of the core. Promising results show that the origin of the F-layer and its future long-term development may be probed.

Abbreviations

IC	Inner Core
OC	Outer Core
ICB	Inner Core Boundary
CSB	Core Slurry Boundary
CMB	Core Mantle Boundary
PREM	Prelminary Reference Earth Model
BVP	Boundary Value Problem
ODE	Ordinary Differential Equation

Contents

List of Figures

Chapter 1

Introduction

Contents

1.1 Background and Motivation

1.1.1 Core convection

Understanding the structure and dynamics of the Earth's interior is one of the central goals of geophysics. Paleomagnetic records show that the Earth's magnetic field has persisted over the past 3.5 billion years (Kono & Roberts, 2002; Tarduno *et al.*, 2010). If the core was not actively driven, then the magnetic field would decay away on a $20,000$ year magnetic diffusion time-scale (Glatzmaier & Coe, 2015). Gauss (1877) deduced that the magnetic field must be internal in origin, and Larmor (1919) suggested that self-excited dynamo action is responsible for sustaining the Earth's magnetic field, whereby electric currents are induced by metallic liquid undergoing convection. To drive convection, a large amount of heat was released during core formation and the Earth has been cooling ever since. Heat loss from the surface of the planet is roughly estimated to be 45 TW (Jaupart *et al.*, 2007). Estimates of the fraction of this heat loss through the core-mantle boundary (CMB) vary widely from 5 to 17 TW (Lay *et al.*, 2008; Nakagawa & Tackley, 2007; Nimmo, 2015b). The rate at which heat can be extracted from the core by the mantle ultimately controls core convection and therefore dynamo operation. There is difficulty reaching a consensus about the value of the CMB heat flux since direct temperature measurements of the Earth's deep interior are impossible. Furthermore core conditions are difficult to replicate in the laboratory, with pressures reaching up to 330 GPa (Dziewonski & Anderson, 1981). Seismology is the only tool that allows us to understand the density structure of the Earth's interior, therefore any realistic geophysical model of the core should match the seismic observations.

Heat can be transported through the core by conduction and convection. The heat that cannot be evacuated out of the core by conduction is available to drive convection.

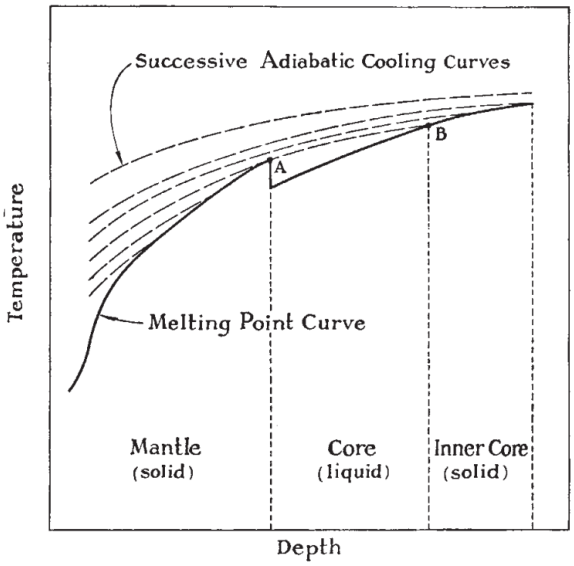

Figure 1.1: The solid inner core grows over time as the core cools. The dashed curves denote the cooling adiabatic temperature at successive times. The ICB is defined at point B where the adiabat crosses the melting curve (solid line). Figure from Jacobs (1953).

Convection can only occur when the temperature gradient exceeds the adiabatic value. Consider a small parcel of material that is displaced vertically upwards in a homogeneous medium. Suppose this happens on a time-scale so rapid that no heat transfer occurs between the parcel and the medium. The temperature of the parcel decreases by adiabatic cooling, where the volume of the parcel expands and work is done on its surroundings. If the temperature of the parcel is the same as its new surroundings, then the medium possesses an adiabatic gradient. If the temperature of the parcel is lower than its surroundings, then the parcel is denser and will sink: the medium has a sub-adiabatic temperature gradient. Conversely, if the temperature of the parcel is greater than its new surroundings, then the parcel is lighter and will continue to rise. In this case the medium is super-adiabatic and unstable, giving rise to convection. Convection is very efficient at advecting heat in a system, therefore the temperature gradient in the core is believed to be very close to adiabatic, and this approximation is key to

estimating many thermal properties of the core (Gubbins *et al.*, 2003).

Fluid velocities inferred from secular variations in the Earth's magnetic field are on the order of 10^{-4} ms^{-1} (Jault & Le Mouël, 1991). Vigorous core motions displace fluid fast enough that the mean temperature in the liquid outer core is assumed to closely approximate an adiabat, except in thin boundary layers. Convection also homogenises the distribution of light elements in the bulk of the core. As the core cools latent heat is released at the inner core boundary (ICB) in which the inner core solidifies from the liquid iron alloy, and the extra latent heat released promotes convection. The inner core freezes out from the centre of the Earth where it is hottest rather than from the CMB where it is cooler. This is because the pressure at the centre of the Earth is extremely high and steepens the melting curve. The melting curve is a phase boundary that characterises the melting behaviour of a material and may be experimentally determined. For iron alloys, the melting curve originally crosses the adiabat at the centre of the Earth, and so the inner core freezes from the centre outwards as the core gradually cools (see Figure 1.1). Freezing the inner core releases buoyant light material at the ICB and promotes compositional convection since light element impurities are incompatible with the solid. The gravitational energy released as a result is a significant source of power for the dynamo.

1.1.2 Core temperature

Knowing the melting behaviour of core iron alloys is important for deducing the temperature structure of the core since direct, physical measurements of the temperature inside the core cannot be made. Theoretical and experimental approaches in mineral physics can provide meaningful insights by constructing phase diagrams of iron alloys at core conditions.

The thermodynamics of first-order phase transitions has been well understood for

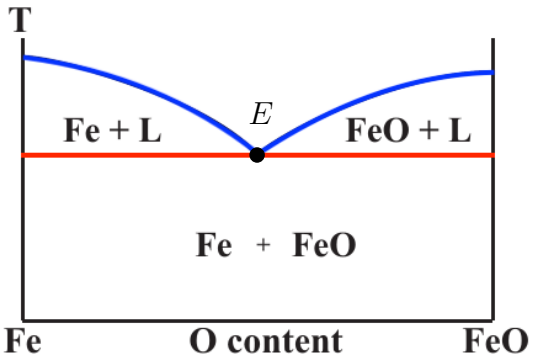

Figure 1.2: Eutectic phase diagrams of an Fe-O alloy at 330 GPa. (Blue) liquidus curve, (red) solidus curve. Symbol L denotes liquid phase and E denotes the eutectic point. Figure modified from Morard *et al.* (2014).

a long time, though a general theory on a macroscopic scale for understanding regions of mixed phases in thermodynamic equilibrium is less clear (Roberts & Loper, 1987). A pure phase contains a single constituent where its physical properties are entirely described by two thermodynamic variables, namely the temperature and pressure. A phase diagram shows the thermodynamically distinct phases that occur and coexist at equilibrium given a set of pressure and temperature conditions.

For a medium that contains two components (e.g. a binary alloy), then the system is divided into two homogeneous bodies that can be in different states but are in contact with one another at the same time. Landau *et al.* (1980) state that for equilibrium between two components, their temperatures, pressure and chemical potentials must be equal. Contrary to a single component medium, the physical state of a binary mixture is described by three thermodynamic variables: temperature, T, pressure, p, and composition, ξ. Figure 1.2 presents a eutectic phase diagram for an Fe-O alloy at 330 GPa (Morard *et al.*, 2014). The liquidus curve is where solidification first starts as material is cooled. The lower solidus curve is when all of the material has completely solidified. The eutectic point, E, shows the lowest melting point of the system where the three phases (one liquid phase, and one solid phase of each component) can coexist.

The eutectic diagram is a cross-section of a three-dimensional surface in p, T, ξ-space, where ξ denotes the light element concentration. The eutectic point, E, therefore lies on a eutectic line that varies with pressure. The Fe-O alloy eutectic diagram in Figure 1.2 represents a typical eutectic system, and increasing the pressure would move the eutectic point to a higher O composition (Komabayashi, 2014). Core composition must fall on the iron-rich side of the eutectic to match the seismic measurements of density and bulk modulus in the core (Melchior, 1986). As the Earth cools over time, the iron that is excess to the eutectic composition solidifies.

Estimating the melting temperature of iron at the ICB is important because it provides an anchor point to extrapolate along the adiabat and determine the temperature profile across the liquid core. High-pressure experiments and first-principles calculations are conducted in an effort to understand the phase diagrams of pure iron and its alloys at the relevant core pressure and temperature conditions. Alfe *et al.* (2004) use *ab initio* calculations to estimate that the melting temperature of pure iron is approximately 6250 ± 300 K at ICB pressures . Figure 1.3 gives an overview of melting curves for pure iron derived from experiments using shock (Brown & McQueen, 1986; Nguyen & Holmes, 2004; Yoo *et al.*, 1993), diamond anvil cell (Boehler, 1993; Jackson *et al.*, 2013; Komabayashi & Fei, 2010; Shen *et al.*, 2004; Williams *et al.*, 1987), fast x-ray diffraction (Anzellini *et al.*, 2013; Ma *et al.*, 2004), and *ab initio* calculations (Alfè, 2009; Alfè *et al.*, 2002c; Belonoshko *et al.*, 2000; Sola *et al.*, 2009). Though consensus between melting curves has been difficult to achieve in the past, recent progress in experimental methods (Anzellini *et al.*, 2013) appears to agree well with *ab initio* calculations for pure iron. Melting data for iron alloys differ from pure iron because light material depresses the melting temperature (see further discussion in Section 1.1.3).

Thermal conductivity, k, is one of the least well-constrained physical properties at

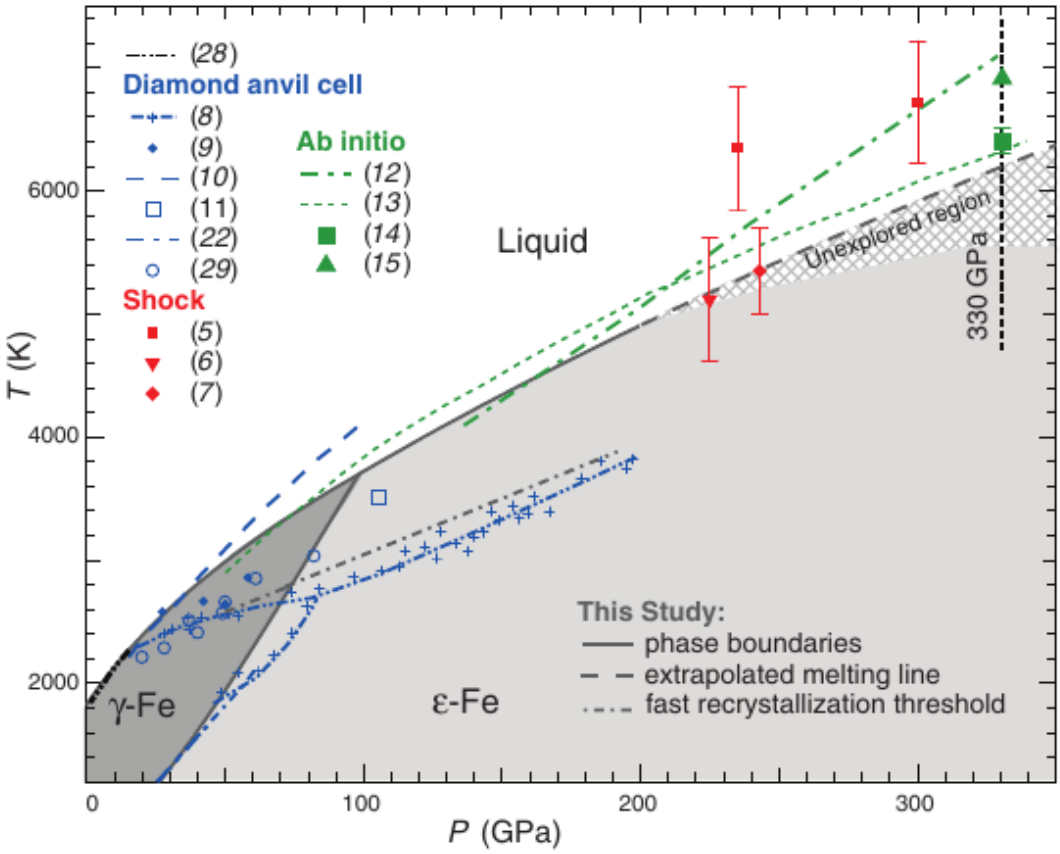

Figure 1.3: Melting curves of pure iron obtained from experiment and *ab initio* calculations. (8) Boehler (1993), (9) Shen *et al.* (2004), (10) Williams *et al.* (1987), (11) Ma *et al.* (2004), (22) Komabayashi & Fei (2010), (29) Jackson *et al.* (2013), (5) Yoo *et al.* (1993), (6) Nguyen & Holmes (2004), (7) Brown & McQueen (1986), (12) Belonoshko *et al.* (2000), (13) Alfè *et al.* (2002c), (14) Alfè (2009), (15) Sola *et al.* (2009). Figure from Anzellini *et al.* (2013).

core conditions. Thermal conductivity is related to the electrical conductivity of the core through the Wiedemann-Franz law (Chester & Thellung, 1961). A higher thermal conductivity increases the ability of the core to conduct heat along the adiabat, which lessens convection and reduces the available power for driving the dynamo. Varying estimates of the thermal conductivity significantly impact estimates of heat flow along the adiabat and thus the inner core age, since heat is conducted from the core more quickly and increases the speed of IC growth (see Figure 1.4). Low k values of 28–46 $\mathrm{Wm^{-1}K^{-1}}$ (Konôpková *et al.*, 2016; Stacey & Anderson, 2001; Stacey & Loper, 2007) predict an older inner core of at least 1 billion years, and high k values of 90–150 $\mathrm{Wm^{-1}K^{-1}}$ (de Koker *et al.*, 2012; Gomi *et al.*, 2013; Ohta *et al.*, 2016; Pozzo *et al.*, 2012) predict a younger inner core of around 500 million years. Estimates are uncertain because the high pressure and temperature conditions of the core are difficult to study in experiments, and the electron-electron interactions in *ab initio* calculations are challenging to model (Pourovskii *et al.*, 2014). Revised estimates of the thermal conductivity significantly impact previous studies of the core that used low k values (Williams, 2018).

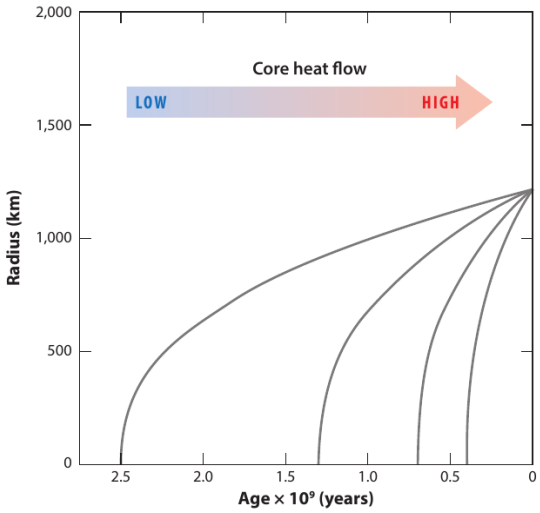

Figure 1.4: Curves showing the radial growth of the inner core over time as a function of core heat flow. Steeper curves correspond with a high thermal conductivity: low k values predict an older inner core of at least 1 billion years and high k values predict a younger inner core of around 500 million years. Figure from Williams (2018).

1.1.3 Core composition

Earth's deep interior is mainly probed by the study of waves triggered by seismic events such as earthquakes. In the early 20$^{\text{th}}$ century Oldham (1906) discovered the core by noticing that the delayed arrival of secondary shear (S) waves was due to a change in physical properties between the mantle and core. Notably, shear waves propagate through solid only and are unsupported by the liquid outer core. Together with studying the Earth's tides, Jeffreys (1926) was able to deduce that the nature of the core was fluid. Lehmann (1936) later determined that the liquid core surrounds a solid inner core, while Birch (1952) noted that the pressure at the centre of the Earth is so high that the inner core is likely to be composed of crystalline iron.

Seismic observations of the density jump at the ICB are important for determining the composition of the core. If the density difference at the ICB cannot be explained by phase change alone then the remainder of the density difference is compositional

in origin, since light elements can enrich the liquid outer core relative to the inner core (Jephcoat & Olson, 1987). Two main types of seismic data are used to determine the density jump at the ICB. Long period normal modes, otherwise known as the free oscillations of the Earth, are triggered by large earthquakes. Short period body waves are compressional and provide a greater resolution than normal modes. Body wave data is not exact, whereas the theory used to calculate normal mode spectra is exact in principle (Deuss, 2014). Masters & Gubbins (2003) performed a normal mode study to show that the density jump at the ICB is $\Delta\rho_{\text{mod}} = 820 \pm 180$ kgm^{-3}. Studies using body wave data give values as low as $\Delta\rho_{\text{bod}} = 520 \pm 240$ kgm^{-3} (Koper & Pyle, 2004) and as high as $\Delta\rho_{\text{bod}} = 1,100$ kgm^{-3} (Tkalčić *et al.*, 2009). Variability in the estimates is due to different sampling techniques and data processing in each study, though a common thread amongst all of the results is that the density difference cannot be explained by phase change alone. This is because the density drop on melting pure iron is 0.24×10^3 kgm^{-3} (Alfè *et al.*, 2002a), which is less than the values of $\Delta\rho_{\text{mod}}$ and $\Delta\rho_{\text{bod}}$ quoted above. Hence the rest of density difference must be attributed to a change in composition.

Cosmochemical and geochemical arguments suggest that the core is composed of an iron alloy with up 5 wt.% nickel (McDonough & Sun, 1995). Light elements must exist in the core because core density is 5–10% smaller than if it were made of pure iron and nickel (Birch, 1964). Candidate light elements include silicon, sulphur, oxygen, hydrogen and carbon (Badro *et al.*, 2014; Hirose *et al.*, 2013; Poirier, 1994). Knowing the partitioning behaviour of the light element during solidification of iron alloys helps to explain the seismic density jump at the ICB, and is therefore essential for understanding how compositional convection is driven in the core. *Ab initio* molecular dynamics simulations are able to characterise partitioning of iron alloys at the relevant core pressures and temperatures. Alfè *et al.* (2002a) study the thermodynamic equi-

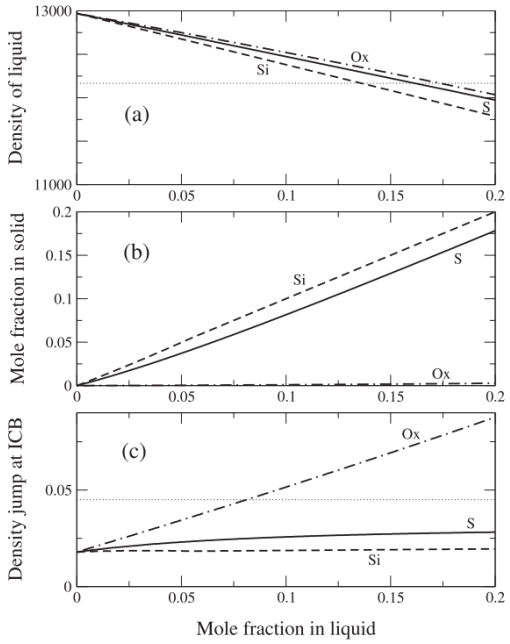

Figure 1.5: *Ab initio* calculations of (a) liquid density, (b) mole fraction in the solid at chemical equilibrium and (c) the relative density jump at the ICB for light elements silicon, sulphur and oxygen. The horizontal dotted lines represent estimates from PREM. Figure from Alfè *et al.* (2002a).

librium between the solid and liquid phases of a binary alloy, in which the chemical potentials of each component must be equal on both sides of the ICB. Figure 1.5 shows significant partitioning of oxygen into the liquid phase compared with the even partitioning of silicon and sulphur into both the liquid and solid phase. According to these calculations, oxygen is not easily retained in a solid crystalline iron lattice because of its smaller atomic radius, thus it is more stable in the liquid phase. Silicon and sulphur substitute with iron freely and are equally stable in both the liquid and solid phase, therefore there are similar concentrations of Si/S in the inner and outer core. Alfè *et al.* (2002a) find that none of the binary systems alone can match the seismic data, though ternary or quaternary alloys of all three impurities can match the seismic data with estimated concentrations of 8.0 ± 2.5 mol.% oxygen and 10 ± 2.5 mol.% silicon and/or sulphur in the liquid, and 0.2 ± 0.1 mol.% oxygen and 8.5 ± 2.5 mol.% silicon

and/or sulphur in the solid. The presence of these light elements depresses the melting temperature at the ICB from $6,350$ K for pure iron to approximately $5,900$ K for an Fe-(Si,S)-O system (Davies *et al.*, 2015). A review by Hirose *et al.* (2013) and further *ab initio* results by Badro *et al.* (2014) also agree that oxygen is an essential component of core chemistry. Umemoto & Hirose (2015) study iron hydrogen alloys using first-principles calculations and rule out that hydrogen can be the only single light element in the core, because the inner core shear velocities could not be reconciled. Nakajima *et al.* (2015) look at iron-carbon alloys using sound velocity measurements, and conclude that the amount of carbon in the core deduced from these measurements is too small to tally with the outer core density deficit.

1.2 The F-layer

1.2.1 Seismic observations of the F-layer

Bullen's nomenclature labelled the layers of the Earth from A to G, with A referring to the crust and G the inner core (Bullen, 1953). The original F-layer indicated that there exists a seismically anomalous transition region between the solid inner core and the liquid outer core, with a density stratification inferred by a slower than expected primary compressional (P) wave velocity (Jeffreys, 1939). Compressional P waves are the only way to sample the liquid core since shear S waves cannot propagate through a liquid. The F-layer thickness was roughly estimated to be 200 km and believed to surround the whole inner core (Jeffreys, 1939).

In the 1970s the original F-layer was shown to be an artefact of scattered waves in the strongly heterogeneous D" layer (Lay *et al.*, 1998) located in the lowermost 200 km of the mantle (Cleary & Haddon, 1972; King *et al.*, 1973). Interest surrounding the F-layer was lost and the region disappeared from subsequent global seismic models and dynamical models of the core. The Preliminary reference Earth model (PREM), shown in Figure 1.6, is a standard one-dimensional seismic model commonly used to describe the density structure of the Earth derived from using both P and S waves (Dziewonski & Anderson, 1981). In this model, the density follows the Adams-Williamson equation, which assumes that the core is homogeneous and approximately follows an adiabatic gradient throughout, since the liquid core is vigorously convecting everywhere except in thin boundary layers.

The modern F-layer emerged when Souriau & Poupinet (1991) noticed that the speed of PKP(bc)[1] waves, which directly sample the lowermost 200 km of the outer

[1] P: longitudinal wave that has passed through the crust and mantle, K: longitudinal wave that has passed through the Earth's outer core, bc: phases that bottom in the lower outer core (Storchak *et al.*, 2003)

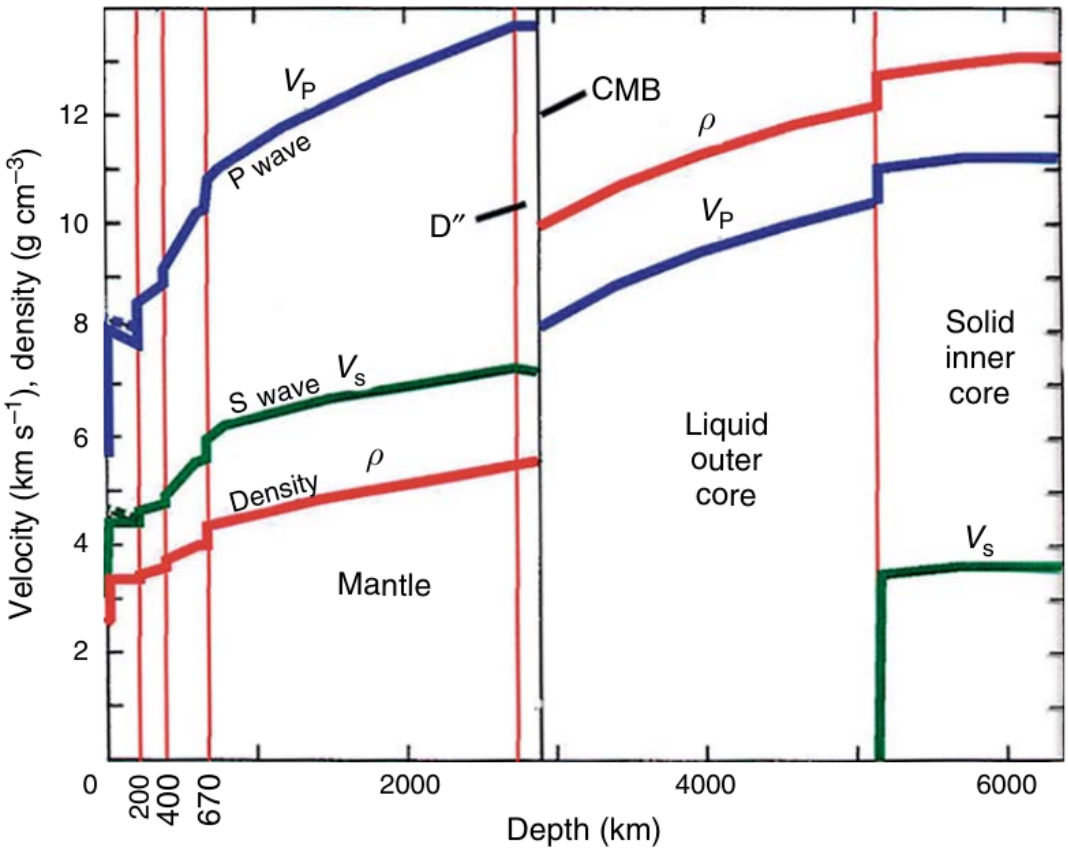

Figure 1.6: The Preliminary reference Earth Model (PREM) (Dziewonski & Anderson, 1981) shows the distribution of seismic velocities and density as a function of depth. This model assumes that the liquid core is well-mixed and adiabatically stratified. Figure from the website of Garnero (Accessed: 04-10-2018).

core, was significantly slower than PREM values. They concluded that this was the result of density stratification (see Figure 1.7). Many following seismic studies confirmed its existence (Adam & Romanowicz, 2015; Ohtaki & Kaneshima, 2015; Zou *et al.*, 2008), and the F-layer was adopted into more recent one-dimensional reference models such as ak135 (Kennett *et al.*, 1995) and PREM2 (Song & Helmberger, 1995). Compared to PREM the P wave velocity is slower by approximately 0.7–0.8% and suggests a stable density stratification because

$$v_p^2 = \frac{K_s}{\rho}, \tag{1.2.1}$$

where v_p is the P wave speed, K_s is the bulk modulus and ρ is the density. At high pressure density varies more than the bulk modulus (Gubbins *et al.*, 2008), therefore a greater density results in a slower P wave speed. Estimates of the layer thickness are variable and generally fall between 150 km (Souriau & Poupinet, 1991) and 350 km (Zou *et al.*, 2008), which is roughly 10% of the radial distance from the ICB to the CMB.

Reconciling the observed F-layer with the conventional view of outer core convection is challenging since buoyant light material excluded from the growing solid inner core and released at the ICB must be able to pass through a stably-stratified layer and into the overlying core. Explaining the F-layer is therefore of great geophysical importance since compositional convection provides significant amounts of gravitational energy to power the geodynamo. Other contributing power sources include secular cooling, latent heat release from core crystallisation, pressure freezing and radiogenic heating (Gubbins *et al.*, 2003). Apart from radiogenic heating these contributions are proportional to the core cooling rate, which is controlled by the rate heat is extracted by the mantle (Gubbins *et al.*, 2003).

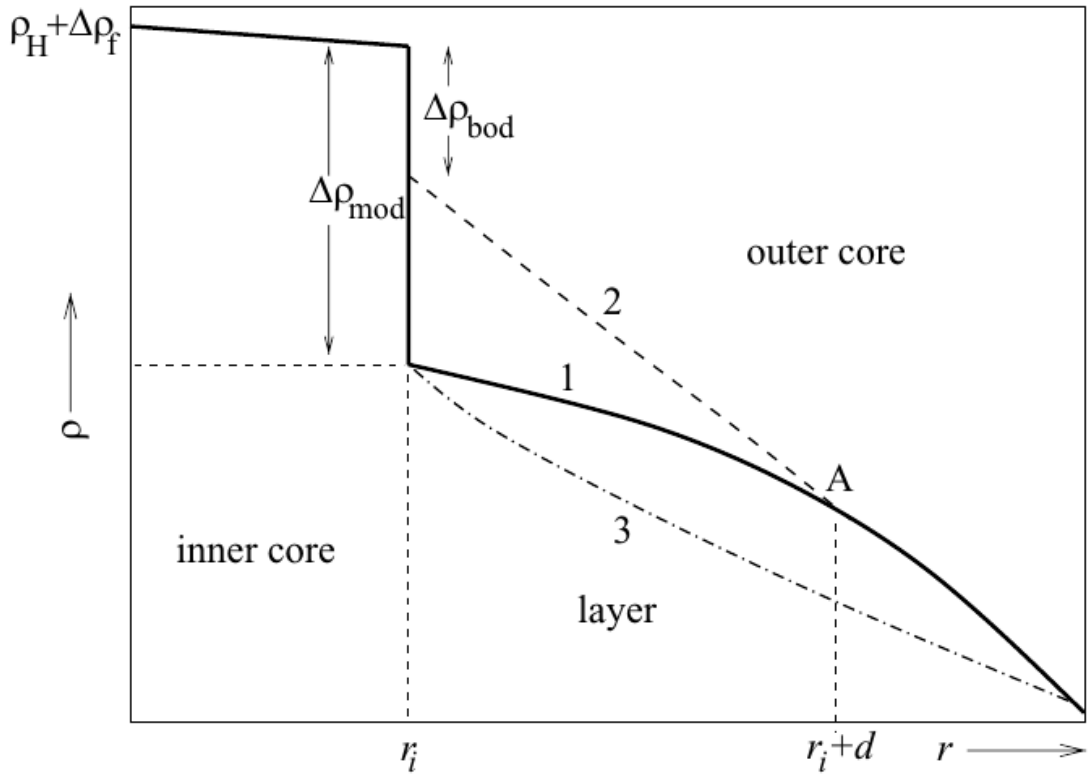

Figure 1.7: A schematic of the density profiles inferred from V_p profiles given by (1) PREM (Dziewonski & Anderson, 1981), (2) Souriau & Poupinet (1991) and (3) Kaneshima *et al.* (1994). Figure from Gubbins *et al.* (2008).

1.2.2 Models of the F-layer

Braginsky (1963) was the first to recognise that the continuous crystallisation of the inner core as the Earth slowly cools could help power the geodynamo and generate the Earth's magnetic field. Heat extracted from the core by the mantle supports mantle convection, which in turn leads to visible surface processes such as volcanism and plate tectonics (Stacey & Davis, 2008). As heat is lost from the surface of the Earth over time, the inner core cools and grows as iron solidifies from the liquid alloy that composes the outer core. Buoyant, light material that is incompatible with the solid inner core is released at the inner core boundary as a result, driving compositional convection in the liquid outer core that sustains dynamo action. To explain the anomalous F-layer, Braginsky's model considered an iron-sulphur core with a sulphur concentration above the eutectic point. Core cooling creates solid particles of sulphur lighter than the surrounding liquid that float to the top of the F-layer, leaving a compositionally stratified layer. It was hypothesised that the excess sulphur rises out of the layer to drive compositional convection in the rest of the liquid outer core.

Classic models of core dynamics assume perfect mixing due to convection in the liquid outer core, except in thin boundary layers (Nimmo, 2015a). The mean temperature profile closely follows an adiabat that is extrapolated from the melting temperature at the ICB, which is dependent on pressure and composition. One may suppose that the F-layer is purely thermal in origin, where slower fluid velocity close to the solid boundary of the inner core inhibits convective mixing in a super-adiabatic, conductive boundary layer. In this conductive boundary layer, the density decreases with depth since material at the bottom of the layer is hotter and more thermally buoyant than at the top. The resulting density stratification in a thermal boundary layer contradicts the density increase with depth inferred from relation (1.2.1), since slower P wave speeds would have been observed, therefore the F-layer cannot be explained by a thermal

boundary layer alone (Gubbins *et al.*, 2008).

Alternatively, a thermochemical, single phase layer composed of liquid iron alloyed with light element was proposed by Gubbins *et al.* (2008). The model contains an updated core chemistry model using an Fe-(Si,S)-O alloy on the iron-rich side of the eutectic rather than a sulphur rich core on the iron-poor side of the eutectic as Braginsky (1963) did. A compositional gradient is imposed on the F-layer *a posteriori* by specifying the light element concentration at the layer boundaries, so that the normal mode data, $\Delta\rho_{\mathrm{mod}}$, matches the concentration at the top boundary and body wave data, $\Delta\rho_{\mathrm{bod}}$, matches the bottom boundary. These conditions enforce the density stratification to be the same as the seismology. The temperature in the layer is assumed to follow the liquidus to avoid producing an F-layer that is completely solid. However, there is no consistent thermodynamic treatment of a solid phase described by the model. Steady state is assumed and modelled by considering a reference frame that is moving at the speed of inner core growth. Growth speed is computed iteratively by balancing the heat flux through the layer with the latent heat release and the specific heat lost by secular cooling. A solution of the thermochemical model is presented in Figure 1.8. Gubbins *et al.* (2008) test the model by computing the heat flux through the ICB and CMB for various layer thicknesses and light element concentration gradients. Solutions produced ICB heat fluxes that match a nominal inner core age of $1\ \mathrm{Ga}$ using a low thermal conductivity, and CMB heat fluxes that fall between 5 and $17\ \mathrm{TW}$ were obtained. However, the model fails to explain the dynamics of how the imposed concentration gradient may be sustained, and how light material can pass through the stably-stratified layer without disturbing it.

Convective translation of the inner core is proposed as another possible mechanism for explaining the F-layer. This particular deformationless mode of motion can arise in convectively unstable conditions and results in inner core freezing in the western hemi-

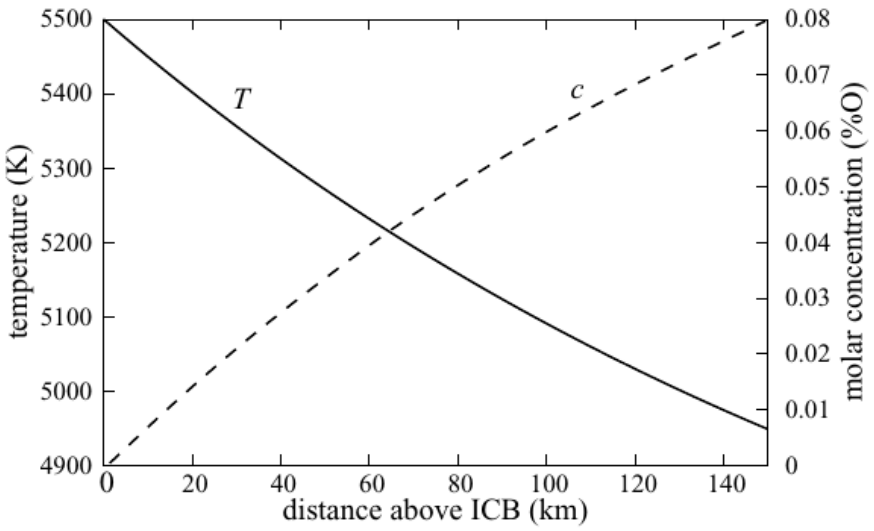

Figure 1.8: A model solution from Gubbins *et al.* (2008) of the temperature (solid) and concentration (dashed) as a function of distance above the ICB. The input parameters are layer thickness, $d = 150$ km, light element concentration $c(d) = 8$ mol.% oxygen at the top of the layer and $c(0) = 0$ mol.% at the base of the layer, which imposes a concentration gradient that matches the seismically determined density jumps $\Delta\rho_{\text{mod}} = 600$ kg m^{-3} and $\Delta\rho_{\text{bod}} = 240$ kg m^{-3}.

sphere and melting in the eastern hemisphere, which produces an iron-rich dense layer that coats the inner core. Alboussière *et al.* (2010) use a low thermal conductivity of 36 W m^{-1} K^{-1} (Stacey & Davis, 2008) that favours superadiabatic conditions for thermal convection in the inner core, and a high critical viscosity on the order of 10^{18} Pa s accommodates convective instability by reducing viscous deformation. The viability of this mechanism may be limited by more recent high thermal conductivity estimates, which implies that the inner core is thermally stratified (Deguen, 2012). Compositional effects have been proposed as an alternative pathway to inner core convection since freshly created solid at the ICB contains less light elements and increases the density with radius over the lifetime of the inner core, which gives rise to unstable stratification as the concentration of iron is progressively refined (Deguen *et al.*, 2013). Gubbins *et al.* (2013) find a weak chemical stratification caused by temperature-dependent partitioning of light elements, though Labrosse (2014) and Lythgoe *et al.* (2015) find that

unstable compositional effects are weaker than the stabilising effect of thermal stratification and so inner core convection is unlikely to occur. More recently Deguen *et al.* (2018) consider the possibility of double-diffusive convection in the inner core owing to the large difference in thermal and chemical diffusivities. They propose that inner core translation is feasible provided that the compositional profile of the inner core is destabilising and that the inner core viscosity is sufficiently large. Though it is possible these conditions were met over the inner core's history, there is uncertainty whether this applies in the present day. Models of convective translation are mainly concerned with explaining the hemispherical asymmetry of the inner core. It is unclear whether the magnitude of this convection can explain an observed global F-layer hundreds of kilometres thick. For example, the layers produced by Deguen *et al.* (2014) fail to envelop the entire inner core.

Other attempts to explain the F-layer include invoking a mushy zone, which consists of a solid matrix of dendritic iron crystals percolated with liquid channels enriched in light elements called 'chimneys' (Hills *et al.*, 1983). Drawing from metallurgical arguments, Fearn *et al.* (1981) suggested that liquid supercooled close to the ICB interface gives rise to a mushy zone, where dendritic growth extends from the solidification front into the liquid outer core. It was even suggested that the depth of this zone may possibly extend to the centre of the Earth, but depending on the liquidus slope used the depth can be $300\ \mathrm{km}$ (Deguen *et al.*, 2007). Around the same time Loper & Roberts (1981) argued that these dendrites are easily broken by convective flow, and advocated for a slurry layer that contains iron crystals forming from the liquid alloy ahead of the ICB.

To form a solid crystal, an activation barrier must be overcome due to the competition between the bulk energy and interfacial energy of the system (Christian, 2002). For conditions in the Earth's core, surmounting this barrier is almost impossible in the

case of homogeneous nucleation because this requires a large amount of supercooling on the order of $1,000$ K (Huguet *et al.*, 2018). The only other alternative pathway to form solid crystals in the core would be through heterogeneous nucleation, in which pre-existing substrates would lower the activation energy.

Subsequent studies have considered inner core growth models using mushy zones (Deguen *et al.*, 2007; Loper & Roberts, 1981; Shimizu *et al.*, 2005), because it was speculated that the core could not supply enough substrates for heterogeneous nucleation to occur and produce a slurry. However, these studies are limited because the effect of core convection, compaction and the crystal structure of iron under high pressure on the mush is poorly understood. Seismic studies by Adam *et al.* (2018) and Zou *et al.* (2008) observe a strongly attenuating region at the base of the outer core, which is the opposite to what is normally expected. As a result, both studies appeal to the presence of a slurry layer containing a suspension of solid iron particles to explain the scattering of seismic waves in this F-layer region.

In this thesis, we believe the slurry hypothesis can explain the dynamics of the F-layer in a self-consistent manner that agrees with the seismic constraints. Loper & Roberts (1977) extend the original model by Braginsky (1963) to develop a general theory on the motion of an iron-alloy core containing a slurry. A core composition on the iron-rich side of the eutectic was considered. A slurry is a two-component, two-phase system and describes the dynamics of solidification and sedimentation of iron particles that was absent from the Gubbins *et al.* (2008) model. Solid iron particles freezing throughout the slurry layer that sink under gravity towards the ICB to grow the inner core, whilst the remaining light material released throughout the layer migrates to the outer core to power the dynamo without disturbing the F-layer. We believe a slurry completes the dynamics of the F-layer that was missing from previous studies, since the transport of solid phase can be described and provides a pathway for light

material to pass through a stably-stratified layer.

In this project, the theory by Loper & Roberts (1977, 1980, 1987) and Roberts & Loper (1987) will be developed into a tractable problem and geophysically relevant parameters will be updated. We will demonstrate that a slurry can aid understanding of the dynamics concerning the F-layer, and provide a way for light element released by the growing inner core to pass through a stably-stratified F-layer. Explaining this process is important because the release of these light elements is fundamental to powering the geodynamo.

1.3 Project aims

The aim of this thesis is to develop an idealised, self-consistent slurry model that explains the dynamics of how heat and light material may pass through the F-layer. The model should be compatible with the geophysical observations provided by seismology and agree with constraints on the thermal history of the core. To this end, the objectives are:

1. Derive the governing equations and boundary conditions of a slurry.
   (a) Develop a mathematical description of the slurry model based on the general theory of Loper & Roberts (1977, 1980, 1987); Roberts & Loper (1987).
   (b) Determine geophysically appropriate boundary conditions for the slurry layer.
2. Establish a geophysically plausible, one-dimensional, steady state slurry model.
   (a) Derive an idealised, steady-state numerical model that captures the fundamental processes of a slurry.
   (b) Explore the parameter space to produce geophysically consistent solutions that explain the F-layer.
3. Investigate the implications of the slurry's presence in the core over time.
   (a) Present a time-dependent model of the slurry with the relevant boundary conditions that couple the layer to the changing thermal state of the core.
   (b) Demonstrate that the F-layer can be formed by a growing slurry layer on geological time-scales

1.4 Thesis outline

In view of a systematic approach to explaining the stable F-layer, Chapter 2 outlines the general slurry theory and examines the thermodynamics of the system. We formulate a simplified theory clarifying the relevant dynamics and thermodynamics of a Boussinesq slurry that is more practical than a full non-equilibrium slurry theory as described by Loper & Roberts (1977). Specifically, the fast-melting limit and constant solid assumption are applied in order to reduce the thermodynamic complexity of a two-component, two-phase system. This constrains the slurry to follow the liquidus temperature everywhere in the layer and prohibits light element in a solid phase.

Chapter 3 develops a novel, steady-state box model that explains the present day F-layer. We solve the equations to find geophysically relevant solutions by fixing the layer thickness and explore the parameter space guided by the latest estimates of physical properties. By testing the sensitivity of the thermal conductivity in our model, we anticipate that the outcomes of this research are timely due to the recent debate of its value in the literature. A key step advanced by the model is that a dynamical explanation of how light material is transported through a stable layer is provided. This chapter is concluded by a discussion of the results.

Chapter 4 continues with the steady-state model and transforms the geometry of the system from Cartesian to spherical coordinates. Boundary conditions are improved by adopting more sophisticated assumptions that couple the slurry layer to the inner core and outer core in a geophysically realistic manner, so that the heat flow into and out of the slurry is controlled by the thermal history of the entire core. Solutions to this model provide suitable initial states for the time-dependent model.

Chapter 5 extends the work of the box and spherical models by relaxing the steady-state assumption to allow for time-dependence. This allows the layer to either grow or

shrink over time in response to the thermal evolution of the entire core. A numerical scheme is implemented to account for the slurry boundaries moving independently of each other at different speeds. Time-dependent boundary conditions are developed so that the global core thermal history dictates the heat flow through the slurry system.

Chapter 6 summarises the contents of this thesis, discusses the limitations of the model, and concludes by proposing further avenues for research in the future.

1.5 Summary

The magnetic field is a robust feature of the Earth that has existed beyond the magnetic diffusion time-scale (Glatzmaier & Coe, 2015). Geochemical arguments assert that the majority of the core is composed of iron (McDonough & Sun, 1995), which permits dynamo action. The magnetic field is sustained by a self-excited dynamo that is internal in origin, whereby convective motions in the metallic liquid outer core supports electromagnetic induction (Larmor, 1919). Temperature gradients with respect to radius in the core closely approximate the adiabat (Nimmo, 2015a), except in thin boundary layers, since convection is very efficient at advecting energy. Substantial amounts of energy are needed to power the dynamo and this is mainly provided by thermal and compositional sources (Gubbins *et al.*, 2004). Earth's interior is very hot because of the accretional heat generated when the Earth was formed. Gradual cooling of the Earth releases thermal energy to support thermal convection.

Seismic data finds that the density deficit of the outer core relative to pure iron is 5–10%, hence lighter elements also exist within the ferrous core (Birch, 1952). The observed density jump at the ICB cannot be explained by phase change alone, therefore light elements must be present in order to account for the rest of the density difference. Viable candidate elements that match the seismic and geochemical constraints include silicon, sulphur and oxygen (Badro *et al.*, 2014; Hirose *et al.*, 2013; Poirier, 1994). The composition of the iron alloy is on the iron-rich side of the eutectic since the solid inner core is denser than the liquid outer core. As the core cools over time heavy iron solidifies to grow the inner core, liberating light elements at the ICB. Partitioning studies show that oxygen readily separates into the liquid phase and is rejected by the crystalline solid iron, whereas silicon and sulphur are incorporated evenly between the solid and liquid phases of iron (Alfè *et al.*, 2002a). The substantial amount of gravita-

tional energy released upon solidification provides the driving force for compositional convection in the liquid core.

Experimentally and theoretically determined phase diagrams of iron and its alloys determines the temperature structure of the liquid core. Estimates of the melting temperature at the ICB provide an anchor point that can be extrapolated along the adiabat to give the temperature distribution across the liquid core. The melting temperature of pure iron is considerably depressed by hundreds of Kelvin when it is alloyed with light element (Davies *et al.*, 2015), which can alter the adiabatic temperature profile significantly. Iron solidifies outwards from an initially fully molten state at the centre of the Earth because the adiabat crossed the melting curve first at the centre (Jacobs, 1953). The latent heat released from phase transition provides a source of power to the geodynamo.

Heat flow out of the core is limited by the ability of mantle convection to extract heat from the core and is estimated to be between 5 and 17 terawatts (Lay *et al.*, 2008; Nimmo, 2015a). Upward revisions of the thermal conductivity of core material increase the amount of heat that is conducted along the adiabat, reducing the thermal energy available for thermal convection (Williams, 2018). This forces the inner core to be younger since heat is removed from the core more quickly and so the speed of inner growth is faster.

There is mounting evidence to suggest that a stably-stratified F-layer resides at the base of Earth's outer core. A low P wave velocity layer is consistently observed by seismology (Adam & Romanowicz, 2015; Ohtaki & Kaneshima, 2015; Souriau & Poupinet, 1991; Zou *et al.*, 2008). P waves passing through the lowermost 150–$350\ \mathrm{km}$ portion of the outer core are slower than PREM speeds, in which PREM assumes an adiabatic core. This infers a density stratification that cannot be explained by adiabatic compression alone. The layer cannot be a thermal boundary layer, since temperature

would decrease with radius and therefore produce an unstable density stratification. Gubbins *et al.* (2008) try to explain the F-layer using a thermochemical model. This approach was incomplete because a compositional gradient matching the seismic observations was imposed *a posteriori*, and the presence of any solid phase in the layer was not considered.

Light material rejected by the crystalline iron phase as the inner core solidifies must be able to pass through the stably-stratified F-layer without disturbing it. The aim of this project is to explain this process in a self-consistent manner. Based on the work by Loper & Roberts (1977, 1980, 1987); Roberts & Loper (1987) we believe the F-layer can be explained by a slurry, which is a two-component, two-phase system. Solid particles crystallise from the liquid iron alloy and snow under gravity towards the ICB to grow the inner core, and light material is released throughout the layer rather than immediately at the ICB. This allows the buoyant light material to be expelled into the liquid phase without disturbing the stable stratification.

We shall approach this problem by developing the governing equations of a slurry system based on the general theory of Loper & Roberts (1977, 1980, 1987); Roberts & Loper (1987). A careful and consistent treatment of the thermodynamic system will be required since there exists two components (iron and light element) in two phases (solid and liquid) that undergo phase transition. We will derive appropriate boundary conditions for the slurry layer so that solutions of the model are compatible with seismic, geochemical and geophysical constraints.

An idealised, steady state, one-dimensional box model will be developed so that the essential characteristics of a slurry system are elucidated. To achieve this we shall simplify the thermodynamics by applying two key assumptions: fast–melting and constant solid. The parameter space of this simplified model will be explored based on varying the layer thickness according to seismic estimates, and varying the heat flow

through the system. We shall explore the effect of changing the thermal conductivity since recently revised estimates will have a significant impact on heat transfer.

Solutions of the steady-state model provide the basis for more complex time-dependent studies. We will investigate the evolution of the slurry layer by coupling the system to the global heat balance of the entire core. This will require further development of the equations and boundary conditions. The governing slurry equations are transformed to spherical coordinates and radially dependent properties such as gravity may change significantly as the inner core grows over geological time-scales. The time-dependent study may demonstrate that the slurry can grow in thickness over time, which will shed light on the history and origin of the F-layer.

Chapter 2

Slurry theory

Contents

In this chapter, a general overview of the slurry theory developed by Loper & Roberts (1977, 1980, 1987); Roberts & Loper (1987) is presented. Basic definitions of each constituent of the slurry in each phase are outlined and the conservation laws for these quantities and the entropy equations are formulated. We reduce the thermodynamics of the general slurry theory in two key ways: firstly, by considering the fast-melting limit, and secondly, by assuming a constant solid composition, as originally suggested by Loper and Roberts (Loper & Roberts, 1977, 1980, 1987; Roberts & Loper, 1987). The fast-melting limit assumes that the time-scales of phase change are instantaneous compared to other relevant timescales of the core, thus constraining the system to a state of phase equilibrium. As a consequence, the temperature of the slurry is on the liquidus everywhere in the layer, and we derive a thermodynamically consistent expression for the liquidus using the lever rule. In applying the constant solid assumption we approximate the slurry mixture as a binary Fe-O alloy with oxygen partitioning entirely into the liquid phase, as supported by the partitioning studies of Alfè *et al.* (2002a). The solid material in the slurry is therefore assumed to be pure iron. The constitutive equations for the light element flux, $\mathbf{i}$, solid flux $\mathbf{j}$, and entropy flux, $\mathbf{k}$, are developed by considering the exact differentials of the specific volume, entropy and chemical potential derived from the Gibbs free energy. Jump conditions at the slurry boundaries are developed from first principles, which will be used to inform the boundary conditions imposed on the model in subsequent chapters. A summary of the governing equations of the reduced slurry theory and a table of symbols used is provided. Finally, the global heat balance of the core containing a slurry layer is derived, which will serve as an important geophysical constraint on the results of the model in subsequent chapters.

2.1 Basic definitions

As discussed in Chapter 1, a slurry consists of a two-phase, two component mixture, consisting of a light element alloyed with iron. The components and phases are defined by considering a small volume of material with liquid iron mass M^l_{Fe}, liquid light element mass, M^l_ξ, solid iron mass, M^s_{Fe}, and solid light element mass, M^s_ξ. Here the superscript denotes the phase of the material, with 'l' for liquid and 's' for solid, and the subscript denotes the composition of the material, with 'Fe' for iron and 'ξ' for light element. The mass concentrations of light element, ξ, light element in the liquid phase, ξ^l, light element in the solid phase, ξ^s, and the solid fraction ϕ are defined as

$$\xi = \frac{M^s_\xi + M^l_\xi}{M^l_\xi + M^l_{Fe} + M^s_\xi + M^s_{Fe}} = \frac{\text{Light element mass}}{\text{Total mass}} \tag{2.1.1a}$$

$$\xi^l = \frac{M^l_\xi}{M^l_\xi + M^l_{Fe}} = \frac{\text{Liquid light element mass}}{\text{Liquid mass}} \tag{2.1.1b}$$

$$\xi^s = \frac{M^s_\xi}{M^s_\xi + M^s_{Fe}} = \frac{\text{Solid light element mass}}{\text{Solid mass}} \tag{2.1.1c}$$

$$\phi = \frac{M^s_\xi + M^s_{Fe}}{M^l_\xi + M^l_{Fe} + M^s_\xi + M^s_{Fe}} = \frac{\text{Solid mass}}{\text{Total mass}} \tag{2.1.1d}$$

These definitions determine the relation

$$\xi = \phi\xi^s + (1-\phi)\xi^l, \tag{2.1.2}$$

and its differential form

$$d\xi = \phi \mathrm{d}\xi^s + (1-\phi)\mathrm{d}\xi^l + \left(\xi^s - \xi^l\right)\mathrm{d}\phi \tag{2.1.3}$$

will be used to develop the slurry equations later. The solid fraction ϕ is an average

of the fraction of small, numerous solid grains that occupy a volume. Its value ranges between 0 and 1, where $\phi = 0$ indicates there is no solid present and $\phi = 1$ means that the whole volume is solid. However in a slurry volume we always assume that $\phi \ll 1$ so that the mixture consists of fine grain particles, and we do not consider a solid matrix assembly and resulting effects such as compaction, which is beyond the scope of this thesis.

2.2 Conservation equations

According to seismic observations, the thickness of the F-layer is small compared to the rest of the liquid outer core. Therefore we assume that the density variations within a thin F-layer are small relative to the reference density, ρ_0, and apply the Boussinesq approximation. Density variations are neglected everywhere except in the buoyancy term where they are multiplied by the gravitational acceleration. The total mass of a fixed volume, V, is conserved, and is given by

$$\int_V \rho \, dV, \tag{2.2.1}$$

where $\rho = \rho(\mathbf{x}, t)$ is the density that may be a function of position $\mathbf{x}$ and time t. The mass of V can only change over time if there is a flow, $\mathbf{u} \equiv \mathbf{u}(\mathbf{x}, t)$, across the boundary, S, that encloses volume, V, such that

$$\frac{\mathrm{d}}{\mathrm{d}t} \int_V \rho \, dV = -\int_S \rho \mathbf{u} \cdot \mathbf{dS}, \tag{2.2.2}$$

where $\mathbf{dS}$ is the vector normal to the surface element dS. Since volume V is fixed and does not depend on space and time, then the time derivative may be brought inside the

integral so that (2.2.2) becomes

$$\int_V \left(\frac{\partial \rho}{\partial t} + \nabla \cdot \rho \mathbf{u} \right) \, dV = 0. \tag{2.2.3}$$

This holds for any arbitrary fixed volume, V, therefore

$$\frac{\partial \rho}{\partial t} + \nabla \cdot \rho \mathbf{u} = 0. \tag{2.2.4}$$

An alternative form is

$$\frac{\mathrm{D}\rho}{\mathrm{D}t} = -\rho \nabla \cdot \mathbf{u}, \tag{2.2.5}$$

where

$$\frac{\mathrm{D}}{\mathrm{D}t} \rightarrow \frac{\partial}{\partial t} + \mathbf{u} \cdot \nabla$$

is the material derivative. For a Boussinesq slurry with a constant reference density, ρ_0, then the condition for mass conservation (2.2.5) reduces to

$$\nabla \cdot \mathbf{u} = 0. \tag{2.2.6}$$

In other words the velocity is solenoidal and the slurry is incompressible, where $\mathbf{u}$ is the mean (or barycentric) velocity,

Light element is conserved in the slurry layer, therefore

$$\rho_0 \frac{\mathrm{D}\xi}{\mathrm{D}t} = -\nabla \cdot \mathbf{i}, \tag{2.2.7}$$

is the advection–diffusion equation for light element ξ, where $\mathbf{i}$ is the diffusive flux of light element (Landau & Lifshitz, 1959). Light element in the slurry system cannot be created or destroyed, therefore it is a conserved quantity and no source terms are

present.

The solid fraction, ϕ, is transported by advection and diffusion in the slurry. However, unlike light element, solid can be created and destroyed through freezing and melting thus ϕ is not a conserved quantity. The advection-diffusion equation for the solid is

$$\rho_0 \frac{\mathrm{D}\phi}{\mathrm{D}t} = -\nabla \cdot \mathbf{j} + m^s, \tag{2.2.8}$$

where $\mathbf{j}$ is the solid flux of the particles and m^s is a source term that defines the rate that solid particles are formed (Loper & Roberts, 1977).

Light element is either in a solid phase or a liquid phase, therefore the contribution of solid light element to the solid flux is given by

$$\rho_0 \frac{\mathrm{D}}{\mathrm{D}t}\left(\phi\xi^s\right) = -\nabla \cdot \left(\xi^s \mathbf{j}\right) + m^s_\xi, \tag{2.2.9}$$

where m^s_ξ is the rate at which solid particles of light element are formed. An alternative form can be acquired by using the conservation of solid mass (2.2.8), to give

$$\rho_0 \phi \frac{\mathrm{D}\xi^s}{\mathrm{D}t} = -\mathbf{j} \cdot \nabla \xi^s + m^s_\xi - \xi^s m^s. \tag{2.2.10}$$

It is useful to define

$$\mathbf{i}' = \mathbf{i} - \left(\xi^s - \xi^l\right)\mathbf{j}, \tag{2.2.11}$$

where $\mathbf{i}'$ is the flux of light element in the liquid phase. A two phase binary system is complex because it forms a system with four independent thermodynamic variables for the constituents ξ, ξ^s, ξ^l and ϕ. The diffusive fluxes are separated into three parts $\mathbf{i}, \mathbf{i}'$ and $\mathbf{j}$, compared with the conventional single flux to used describe Fickian diffusion.

The equation for light element in the liquid phase is given by

$$\rho_0 (1-\phi) \frac{\mathrm{D}\xi^l}{\mathrm{D}t} = -\nabla \cdot \mathbf{i}' + \mathbf{j} \cdot \nabla \xi^l - m^s_\xi + \xi^l m^s, \tag{2.2.12}$$

when (2.2.7), (2.2.8), (2.2.10) and (2.2.11) are combined. This justifies that $\mathbf{i}'$ is indeed the diffusive flux of the light element in the liquid phase.

To derive the conservation of momentum, we assume that the slurry layer has a hydrostatic reference state in which departures from hydrostatic equilibrium are small so that

$$\nabla p_H = -\rho_0 \mathbf{g}, \tag{2.2.13}$$

where p_H is the hydrostatic pressure and $\mathbf{g}$ is the gravitational acceleration. The momentum equation under the Boussinesq approximation, with no rotation and no magnetic field[1], is given by

$$\frac{\mathrm{D}\mathbf{u}}{\mathrm{D}t} = -\nabla \left(\frac{p'}{\rho_0} \right) + \rho' \mathbf{g} + \nu \nabla^2 \mathbf{u} + \mathbf{F}, \tag{2.2.14}$$

where p' is the non-hydrostatic pressure, ρ' is the density variation due to buoyancy, ν is the kinematic viscosity and $\mathbf{F}$ are other external body forces.

The entropy equation is given by

$$\rho_0 T \frac{\mathrm{D}s}{\mathrm{D}t} + T \nabla \cdot \mathbf{k} = \rho_0 H + Q_D + Q_M + Q_\nu, \tag{2.2.15}$$

where s is the entropy, $\mathbf{k}$ is the entropy flux vector, and H is the internal heating rate

[1] We are most interested in studying the slurry first before adding more complex effects. Adding the Lorentz and Coriolis is beyond the scope of this thesis.

produced by radiogenic sources (Loper & Roberts, 1977). On the RHS,

$$Q_D = -\mathbf{i}' \cdot \nabla \mu^l - \mathbf{j} \cdot \left(\nabla \mu_\phi - \mu^s \nabla \xi^s + \mu^l \nabla \xi^l \right) - \mathbf{k} \cdot \nabla T, \tag{2.2.16}$$

is the dissipation due to diffusive fluxes. The dissipation due to phase relaxation is given by

$$Q_M = -m^s \left[\mu_\phi - \left(\xi^s - \xi^l \right) \mu^l \right] - \left(m_O^s - \xi^s m^s \right) \left(\mu^s - \mu^l \right), \tag{2.2.17}$$

where m_O^s is the creation rate of oxygen in the solid phase. We define $\mu^s = \mu_{Fe}^s - \mu_\xi^s$ as the chemical potential of iron relative to light element in the solid phase, which is the free energy released when an atom of solid light element replaces an atom of solid iron at constant pressure and temperature. The chemical potential of iron relative to light element in the liquid phase is given by $\mu^l = \mu_{Fe}^l - \mu_\xi^l$, which is the free energy released when an atom of liquid light element replaces an atom of liquid iron at constant pressure and temperature. We also define μ_ϕ as the chemical potential of solid relative to the liquid phase, which is unique to the slurry system and its meaning in terms of the Gibbs free energy shall become clearer in Sections 2.3 and 2.5.

Viscous dissipation is given by

$$Q_\nu = p \nabla \cdot \mathbf{u} + \underline{\underline{\tau}} : \nabla \mathbf{u}, \tag{2.2.18}$$

where symbol ‘: ’ denotes the double inner product and $\underline{\underline{\tau}} = -p\delta_{ij} + \sigma_{ij}$ is the total stress tensor, with p the total isotropic pressure, δ_{ij} the Kronecker delta and σ_{ij} is the deviatoric stress tensor using the Einstein summation convention. Viscous dissipation is an irreversible process that converts kinetic energy into internal energy, through the action of shear forces that heat up the medium.

This completes the set of conservative equations for a general slurry, originally outlined by Loper & Roberts (1977).

2.3 Fast-melting and constant solid composition

The conservation laws formulated in the previous section are valid for a two-component, two-phase slurry system that is thermodynamically complex, making it difficult to solve in practice. We first reduce the general theory by assuming that the fast-melting limit applies. We introduce the Gibbs free energy, which is a fundamental thermodynamic potential that is minimised when a system reaches equilibrium at constant pressure and temperature (Landau *et al.*, 1980). The exact differential of the Gibbs free energy is given by (Loper & Roberts, 1977)

$$\mathrm{d}\Phi = V\ \mathrm{d}p - s\ \mathrm{d}T + \mu^l\ \mathrm{d}\xi + \phi\left(\mu^s - \mu^l\right)\ \mathrm{d}\xi^s + \left[\mu_\phi - \left(\xi^s - \xi^l\right)\mu^l\right]\ \mathrm{d}\phi, \quad (2.3.1)$$

where

$$\left(\frac{\partial\Phi}{\partial p}\right)_{T,\xi,\xi^s,\phi} \equiv V, \qquad \left(\frac{\partial\Phi}{\partial T}\right)_{p,\xi,\xi^s,\phi} \equiv -s,$$
$$\left(\frac{\partial\Phi}{\partial \xi}\right)_{p,T,\xi^s,\phi} \equiv \mu^l, \qquad \left(\frac{\partial\Phi}{\partial \xi^s}\right)_{p,T,\xi,\phi} \equiv \phi\left(\mu^s - \mu^l\right),$$
$$\left(\frac{\partial\Phi}{\partial \phi}\right)_{p,T,\xi,\xi^s} \equiv \mu_\phi - \left(\xi^s - \xi^l\right)\mu^l.$$

At equilibrium the Gibbs free energy is minimised so that $\mathrm{d}\Phi = 0$. In the fast-melting limit, we assume that the freezing time-scale is fast compared to the evolution of the stably-stratified F-layer. In an infinitesimal slurry volume at a constant p, T, ξ and ξ^s, the solid fraction varies as material solidifies so that $\mathrm{d}\phi \neq 0$. We assume that the

approach to equilibrium through freezing is instantaneous so that

$$\mu_\phi - \left(\xi^s - \xi^l\right)\mu^l = 0 \tag{2.3.2}$$

must hold to minimise the Gibbs free energy. Similarly, if solid light element is frozen at constant p, T, ξ and ϕ so that $\mathrm{d}\xi^s \neq 0$, then

$$\mu^s - \mu^l = 0 \tag{2.3.3}$$

must hold. Physically, the fast-melting limit means that in an infinitesimal volume the slurry contains either liquid or solid phase only, and there are no intermediate metastable states in which both phases are present. This implies that the solid iron crystals are in phase equilibrium with the liquid. The chemical potential μ^s no longer enters the theory as a consequence of the fast-melting limit, as phase equilibrium implies $\mu^l = \mu^s$ everywhere and μ^l is rewritten as μ with no danger of ambiguity henceforth. As a result of (2.3.2) and (2.3.3), the dissipation due to phase change (2.2.17) becomes

$$Q_M = 0. \tag{2.3.4}$$

Adopting the fast-melting approximation alone does not avoid the challenging issue of particle history dependence on composition, ξ^s. An iron crystal created at a certain pressure and temperature may move to a location with different pressure and temperature conditions where the particle may accrete material of a different ξ^s that changes the compositional history of that particle. Accounting for this effect would dramatically increase the complexity of this already complicated model. We argue that the sensitivity to the compositional history of a particle can be safely ignored by assuming a constant solid composition as follows.

Constant solid composition assumes that the slurry mixture is a binary alloy composed of iron and oxygen. As discussed in Chapter 1, *ab initio* calculations show that oxygen partitions almost entirely into the liquid phase during solidification. Consequently, the solid phase is exclusively composed of iron, therefore

$$\xi^s = 0 \tag{2.3.5}$$

and (2.1.2), (2.1.3) reduce to

$$\xi = (1-\phi)\,\xi^l, \tag{2.3.6}$$

$$\mathrm{d}\xi = (1-\phi)\ \mathrm{d}\xi^l - \xi^l\,\mathrm{d}\phi. \tag{2.3.7}$$

Particle history dependence on composition is eliminated since solid particles can no longer accrete variable concentrations of ξ^s that depend on differing pressure and temperature conditions. The rate ξ^s is created is equal to zero by equation (2.2.10) so that

$$m_O^s = 0, \tag{2.3.8}$$

where subscript O denotes the oxygen composing the light element ξ.

2.4 Partial volumes

In this section, we define the partial volumes of the slurry components using ideal solution theory. Ideal solution theory assumes that there is no change in volume when components of the slurry are mixed. According to Gubbins *et al.* (2004), this assumption is accurate for the small concentrations of the light elements found in the core. Defining their partial densities will be useful in the next section where we develop the

thermodynamics of the system.

Consider an infinitesimal volume of slurry material, denoted by δV. Applying the constant solid approximation, the total mass inside this volume is defined as

$$M^{sl} = M_O^l + M_{Fe}^l + M_{Fe}^s, \tag{2.4.1}$$

where M^{sl} is the total mass of δV, M_O^l is the mass of oxygen in the liquid phase, M_{Fe}^l is the mass of iron in the solid phase and M_{Fe}^s is the mass of iron in the solid phase. By (2.1.1a) and (2.1.1d), in which $M_O^s = 0$ due to the constant solid assumption, the mass of iron in the liquid phase is given by

$$M_{Fe}^l = M^{sl} - M_O^l - M_{Fe}^s = M^{sl}\left(1 - \xi - \phi\right), \tag{2.4.2}$$

which will be useful later in deriving the partial volume of the whole slurry (2.4.5).

Using ideal solution theory, the volumes of each component can be added together to form the total volume, δV, therefore

$$\delta V_O^l = \frac{M_O^l}{\rho_O^l}, \qquad \delta V_{Fe}^l = \frac{M_{Fe}^l}{\rho_{Fe}^l}, \qquad \delta V_{Fe}^s = \frac{M_{Fe}^s}{\rho_{Fe}^s}, \tag{2.4.3}$$

$$\delta V = \delta V_O^l + \delta V_{Fe}^l + \delta V_{Fe}^s = \frac{M_O^l + M_{Fe}^l + M_{Fe}^s}{\rho} = \frac{M^{sl}}{\rho}, \tag{2.4.4}$$

where ρ is the density of the whole volume, δV. Combining (2.4.4) together with (2.1.1a), (2.1.1d), and (2.4.2) gives the partial volume of the slurry

$$\frac{1}{\rho} = \frac{\xi}{\rho_O^l} + \frac{(1 - \xi - \phi)}{\rho_{Fe}^l} + \frac{\phi}{\rho_{Fe}^s} \tag{2.4.5}$$

$$= \frac{\phi}{\rho_{Fe}^s} + (1 - \phi)\left(\frac{\left(1 - \xi^l\right)}{\rho_{Fe}^l} + \frac{\xi^l}{\rho_O^l}\right), \tag{2.4.6}$$

which is re-written in terms of ξ^l using (2.3.6). Using (2.1.1b) and (2.4.3) , the partial volume of the liquid phase is given by

$$\frac{1}{\rho^l_{Fe,O}} = \frac{\delta V^l_O + \delta V^l_{Fe}}{M^l_O + M^l_{Fe}} = \frac{\left(1-\xi^l\right)}{\rho^l_{Fe}} + \frac{\xi^l}{\rho^l_O}. \tag{2.4.7}$$

Following this, it is clear that (2.4.6) can be expressed as

$$\frac{1}{\rho} = \frac{\phi}{\rho^s_{Fe}} + (1-\phi)\,\frac{1}{\rho^l_{Fe,O}}. \tag{2.4.8}$$

2.5 The liquidus

In this section, we apply the fast melting limit and constant solid assumptions to derive the liquidus equation from the Gibbs free energy. The liquidus is the melting curve on a phase diagram that first divides solid from liquid. Exact differentials of thermodynamic quantities are defined that will elucidate aspects of the slurry equations later. The expression for the liquidus is derived by combining the condition for phase equilibrium together with the lever rule and the exact differential for the chemical potential.

2.5.1 Exact differentials

Under the fast-melting limit and constant solid composition, the exact differential of the Gibbs free energy (2.3.1) becomes

$$\mathrm{d}\Phi = V\ \mathrm{d}p - s\ \mathrm{d}T + \mu\ \mathrm{d}\xi + \left(\mu_\phi + \xi^l\mu\right)\ \mathrm{d}\phi, \tag{2.5.1}$$

where

$$\left(\frac{\partial\Phi}{\partial p}\right)_{T,\xi,\phi} \equiv V, \qquad \left(\frac{\partial\Phi}{\partial T}\right)_{p,\xi,\phi} \equiv -s,$$
$$\left(\frac{\partial\Phi}{\partial \xi}\right)_{p,T,\phi} \equiv \mu, \qquad \left(\frac{\partial\Phi}{\partial \phi}\right)_{p,T,\xi} \equiv \mu_\phi + \xi^l\mu.$$

Equivalently we can combine (2.3.7) and (2.5.1) to express the Gibbs free energy differential in terms of the independent variables $p,\ T,\ \xi^l$ and ϕ to give

$$\mathrm{d}\Phi = V\ \mathrm{d}p - s\ \mathrm{d}T + (1-\phi)\,\mu\ \mathrm{d}\xi^l + \mu_\phi\ \mathrm{d}\phi, \tag{2.5.2}$$

where

$$\left(\frac{\partial\Phi}{\partial p}\right)_{T,\xi^l,\phi} \equiv V, \qquad \left(\frac{\partial\Phi}{\partial T}\right)_{p,\xi^l,\phi} \equiv -s,$$
$$\left(\frac{\partial\Phi}{\partial \xi^l}\right)_{p,T,\phi} \equiv (1-\phi)\,\mu, \qquad \left(\frac{\partial\Phi}{\partial \phi}\right)_{p,T,\xi^l} \equiv \mu_\phi.$$

The Gibbs free energy is a fundamental thermodynamic potential that can be manipulated to give the exact differentials of the specific volume, $\mathrm{d}V$, entropy, $\mathrm{d}s$, and chemical potential, $\mathrm{d}\mu$, that are useful for developing the slurry theory further.

The differential of the specific volume is used to determine the density variation, ρ' in (2.2.14). This is given by

$$\mathrm{d}V = \left(\frac{\partial V}{\partial p}\right)_{T,\xi,\phi}\mathrm{d}p + \left(\frac{\partial V}{\partial T}\right)_{p,\xi,\phi}\mathrm{d}T + \left(\frac{\partial V}{\partial \xi}\right)_{p,T,\phi}\mathrm{d}\xi + \left(\frac{\partial V}{\partial \phi}\right)_{p,T,\xi}\mathrm{d}\phi \tag{2.5.3}$$

$$= -\frac{\beta}{\rho}\,\mathrm{d}p + \frac{\alpha}{\rho}\,\mathrm{d}T + \frac{\alpha_\xi}{\rho}\,\mathrm{d}\xi - \frac{\alpha_\phi}{\rho}\,\mathrm{d}\phi, \tag{2.5.4}$$

where

$$\left(\frac{\partial V}{\partial p}\right)_{T,\xi,\phi} \equiv -\frac{\beta}{\rho}, \qquad \left(\frac{\partial V}{\partial T}\right)_{p,\xi,\phi} \equiv \frac{\alpha}{\rho},$$
$$\left(\frac{\partial V}{\partial \xi}\right)_{p,T,\phi} \equiv \frac{\alpha_\xi}{\rho}, \qquad \left(\frac{\partial V}{\partial \phi}\right)_{p,T,\xi} \equiv -\frac{\alpha_\phi}{\rho},$$

are the thermodynamic definitions of the isothermal compressibility, β (or the inverse of the bulk modulus, $K = 1/\beta$), thermal expansion coefficient, α, compositional expansion coefficient, α_ξ, and phasal expansion coefficient, α_ϕ. The density variation, $\mathrm{d}\rho$, is related to the differential of the specific volume, $\mathrm{d}V$, by

$$\mathrm{d}V = \mathrm{d}\left(\frac{1}{\rho}\right) = -\frac{1}{\rho^2}\mathrm{d}\rho, \tag{2.5.5}$$

therefore

$$\mathrm{d}\rho = \rho\left[\beta\ \mathrm{d}p - \alpha\ \mathrm{d}T - \alpha_\xi\ \mathrm{d}\xi + \alpha_\phi\ \mathrm{d}\phi\right]. \tag{2.5.6}$$

Most of the terms in (2.5.6) are familiar from other well known physical processes: the first term is recognisable from the equation of state for compressible systems (Moran *et al.*, 2010), the second term is well known from thermal convection (Chandrasekhar, 1961) and the third term is familiar from double diffusive systems (Turner, 1973). Only the last term is unique to the slurry system, where the phasal expansion and changes in solid phase contribute to the density variation, $\mathrm{d}\rho$. Unlike water, iron contracts upon freezing and we define $\alpha_\phi > 0$. Since we are applying the Boussinesq approximation, the first term vanishes and the equation of state becomes

$$\rho' = \rho_0\left[-\alpha\ \mathrm{d}T - \alpha_\xi\ \mathrm{d}\xi + \alpha_\phi\ \mathrm{d}\phi\right], \tag{2.5.7}$$

where ρ_0 is the reference density.

The Gibbs free energy is manipulated in a similar manner to the specific volume to give the specific entropy

$$\begin{aligned} \mathrm{d}s &= \left(\frac{\partial s}{\partial p}\right)_{T,\xi^l,\phi} \mathrm{d}p + \left(\frac{\partial s}{\partial T}\right)_{p,\xi^l,\phi} \mathrm{d}T + \left(\frac{\partial s}{\partial \xi^l}\right)_{p,T,\phi} \mathrm{d}\xi^l + \left(\frac{\partial s}{\partial \phi}\right)_{p,T,\xi^l} \mathrm{d}\phi \\ &= -\frac{\alpha}{\rho}\,\mathrm{d}p + \frac{c_p}{T}\,\mathrm{d}T - (1-\phi)\left(\frac{\partial \mu}{\partial T}\right)_{p,\xi^l,\phi} \mathrm{d}\xi^l - \left(\frac{\partial \mu_\phi}{\partial T}\right)_{p,\xi^l,\phi} \mathrm{d}\phi, \end{aligned} \tag{2.5.8}$$

where we make use of the thermodynamic definition of the heat capacity, c_p, and Maxwell's relations

$$\begin{aligned} &\left(\frac{\partial s}{\partial p}\right)_{T,\xi^l,\phi} = -\frac{\partial}{\partial p}\left(\frac{\partial \Phi}{\partial T}\right)_{p,\xi^l,\phi} = -\frac{\partial}{\partial T}\left(\frac{\partial \Phi}{\partial p}\right)_{T,\xi^l,\phi} = -\left(\frac{\partial V}{\partial T}\right) = -\frac{\alpha}{\rho}, \\ &\left(\frac{\partial s}{\partial T}\right)_{p,\xi^l,\phi} \equiv \frac{c_p}{T}, \\ &\left(\frac{\partial s}{\partial \xi^l}\right)_{p,T,\phi} = -\frac{\partial}{\partial \xi^l}\left(\frac{\partial \Phi}{\partial T}\right)_{p,\xi^l,\phi} = -\frac{\partial}{\partial T}\left(\frac{\partial \Phi}{\partial \xi^l}\right)_{p,T,\phi} = -(1-\phi)\left(\frac{\partial \mu}{\partial T}\right)_{p,\xi^l,\phi}, \\ &\left(\frac{\partial s}{\partial \phi}\right)_{p,T,\xi^l} = -\frac{\partial}{\partial \phi}\left(\frac{\partial \Phi}{\partial T}\right)_{p,\xi^l,\phi} = -\frac{\partial}{\partial T}\left(\frac{\partial \Phi}{\partial \phi}\right)_{p,T,\xi^l} = -\left(\frac{\partial \mu_\phi}{\partial T}\right)_{p,\xi^l,\phi}. \end{aligned}$$

The entropy differential is used to derive the temperature equation (2.6.22) later.

The chemical potential differential is used to develop the liquidus relation, and flux vectors $\mathbf{i}$, $\mathbf{j}$, $\mathbf{k}$ later in equations (2.5.27), (2.6.8), (2.6.10) and (2.6.16) respectively. The chemical potential differential is is given by

$$\mathrm{d}\mu = \Delta V^l_{Fe,O}\,\mathrm{d}p + \left(\frac{\partial \mu}{\partial T}\right)_{p,\xi^l,\phi} \mathrm{d}T + \left(\frac{\partial \mu}{\partial \xi^l}\right)_{p,T,\phi} \mathrm{d}\xi^l, \tag{2.5.9}$$

where we make use of the Maxwell relation

$$\left(\frac{\partial \mu}{\partial p}\right)_{T,\xi^l,\phi} = \frac{\partial}{\partial p}\left(\frac{\partial \Phi}{\partial \xi^l}\right)_{p,T} = \frac{\partial}{\partial \xi^l}\left(\frac{\partial \Phi}{\partial p}\right)_{T,\xi^l} = \left(\frac{\partial V}{\partial \xi^l}\right)_{T,\xi^l}.$$

The partial volume (2.4.7) together with $V \equiv V^l_{Fe,O}$, gives

$$\begin{aligned}\left(\frac{\partial V^l_{Fe,O}}{\partial \xi^l}\right)_{T,\xi^l} &= \left(\frac{\partial}{\partial \xi^l}\left(\frac{1}{\rho^l_{Fe,O}}\right)\right)_{T,\xi^l} \\ &= \left(\frac{\partial}{\partial \xi^l}\left(\frac{1-\xi^l}{\rho^l_{Fe}} + \frac{\xi^l}{\rho^l_O}\right)\right)_{T,\xi^l} \\ &= \frac{1}{\rho^l_O} - \frac{1}{\rho^l_{Fe}} \\ &= V^l_O - V^l_{Fe} \equiv \Delta V^l_{Fe,O}.\end{aligned}$$

Therefore

$$\left(\frac{\partial \mu}{\partial p}\right)_{T,\xi^l,\phi} \equiv \Delta V^l_{Fe,O}, \tag{2.5.10}$$

is the change in specific volume between liquid iron and oxygen.

2.5.2 The lever rule

Assuming that the liquid and solid phases do not interact chemically, which is commonly supposed in phase equilibrium (Loper & Roberts, 1977), then the lever rule can apply where the Gibbs free energy is assumed linear in ϕ such that

$$\Phi = \phi\Phi^s(p,T) + (1-\phi)\,\Phi^l(p,T,\xi^l), \tag{2.5.11}$$

where Φ^s is the Gibbs free energy of the solid and Φ^l is the Gibbs free energy of the liquid. Its exact differential is

$$d\Phi = \phi d\Phi^s + (1-\phi)d\Phi^l + \left(\Phi^s - \Phi^l\right) d\phi, \tag{2.5.12}$$

where

$$\mathrm{d}\Phi^s = \left(\frac{\partial \Phi^s}{\partial p}\right)_T \mathrm{d}p + \left(\frac{\partial \Phi^s}{\partial T}\right)_p \mathrm{d}T, \tag{2.5.13}$$

$$\mathrm{d}\Phi^l = \left(\frac{\partial \Phi^l}{\partial p}\right)_{T,\xi^l} \mathrm{d}p + \left(\frac{\partial \Phi^l}{\partial T}\right)_{p,\xi^l} \mathrm{d}T + \left(\frac{\partial \Phi^l}{\partial \xi^l}\right)_{p,T} \mathrm{d}\xi^l, \tag{2.5.14}$$

are the solid and liquid parts of the Gibbs free energy differential respectively. The full expression of the Gibbs free energy differential in terms of the chosen independent thermodynamic variables p, T, ξ^l, ϕ, is given by substituting (2.5.13) and (2.5.14) into (2.5.12) to get

$$\mathrm{d}\Phi = \left(\phi\frac{\partial \Phi^s}{\partial p} + (1-\phi)\frac{\partial \Phi^l}{\partial p}\right) \mathrm{d}p + \left(\phi\frac{\partial \Phi^s}{\partial T} + (1-\phi)\frac{\partial \Phi^l}{\partial T}\right) \mathrm{d}T + (1-\phi)\frac{\partial \Phi^l}{\partial \xi^l}\,\mathrm{d}\xi^l + \left(\Phi^s - \Phi^l\right)\,\mathrm{d}\phi. \tag{2.5.15}$$

By comparing (2.5.15) with (2.5.2), it can be seen that the specific volume, V, and entropy, s, follow a similar lever rule with

$$V = \phi V^s_{Fe} + (1-\phi)\, V^l_{Fe,O}, \tag{2.5.16}$$

$$s = \phi s^s + (1-\phi)\, s^l, \tag{2.5.17}$$

where

$$\begin{aligned} V^s_{Fe} &= \left(\frac{\partial \Phi^s}{\partial p}\right)_T, & V^l_{Fe,O} &= \left(\frac{\partial \Phi^l}{\partial p}\right)_{T,\xi^l}, \\ -s^s &= \left(\frac{\partial \Phi^s}{\partial T}\right)_p, & -s^l &= \left(\frac{\partial \Phi^l}{\partial T}\right)_{p,\xi^l}, \\ \mu &= \left(\frac{\partial \Phi^l}{\partial \xi^l}\right)_{p,T}, & \mu_\phi &= \Phi^s - \Phi^l. \end{aligned} \tag{2.5.18}$$

Using (2.5.18), differentials (2.5.13) and (2.5.14) can be re-written as

$$\mathrm{d}\Phi^s = V^s_{Fe}\,\mathrm{d}p - s^s\,\mathrm{d}T, \tag{2.5.19}$$

$$\mathrm{d}\Phi^l = V^l_{Fe,O}\mathrm{d}p - s^l\,\mathrm{d}T + \mu\,\mathrm{d}\xi^l. \tag{2.5.20}$$

Assuming constant solid composition, (2.3.5), the phase equilibrium condition, (2.3.2), becomes

$$\mu_\phi + \xi^l\mu = 0. \tag{2.5.21}$$

Substituting μ_ϕ (2.5.18) into (2.5.21), the phase equilibrium condition can be expressed as

$$\Phi^s - \Phi^l + \xi^l\mu = 0, \tag{2.5.22}$$

via the lever rule. The differential of (2.5.22) is also equal to zero at phase equilibrium, so

$$\mathrm{d}\Phi^s - \mathrm{d}\Phi^l + \xi^l\mathrm{d}\mu + \mu\mathrm{d}\xi^l = 0. \tag{2.5.23}$$

Substituting (2.5.19) and (2.5.20) into (2.5.23) gives

$$\left(V^s_{Fe} - V^l_{Fe,O}\right)\,\mathrm{d}p + \left(-s^s + s^l\right)\,\mathrm{d}T + \xi^l\,\mathrm{d}\mu = 0, \tag{2.5.24}$$

and we define

$$V^l_{Fe,O} - V^s_{Fe} \equiv \Delta V^{s,l}_{Fe,O} \tag{2.5.25}$$

as the change in specific volume between liquid and solid, otherwise known as the change in specific volume upon melting. By using the chemical potential differential

(2.5.9), then (2.5.24) can be written

$$-\Delta V^{s,l}_{Fe,O}\,\mathrm{d}p + \left(-s^s + s^l\right)\,\mathrm{d}T + \xi^l\left[\Delta V^l_{Fe,O}\,\mathrm{d}p + \left(\frac{\partial \mu}{\partial T}\right)_{p,\xi^l,\phi}\mathrm{d}T + \left(\frac{\partial \mu}{\partial \xi^l}\right)_{p,T,\phi}\mathrm{d}\xi^l\right] = 0. \quad (2.5.26)$$

Re-arranging (2.5.26) yields the liquidus relation

$$\Delta V^{s,l}_{Fe}\,\mathrm{d}p - \frac{L}{T}\,\mathrm{d}T = \xi^l\frac{\partial \mu}{\partial \xi^l}\,\mathrm{d}\xi^l, \quad (2.5.27)$$

where

$$\begin{aligned}\Delta V^{s,l}_{Fe,O} - \xi^l \Delta V^l_{Fe,O} &= V^l_{Fe,O} - V^s_{Fe} - \xi^l\left(V^l_O - V^l_{Fe}\right)\\ &= \frac{1}{\rho^l_{Fe,O}} - \frac{1}{\rho^s_{Fe}} - \xi^l\left(\frac{1}{\rho^l_O} - \frac{1}{\rho^l_{Fe}}\right)\\ &= \frac{\left(1-\xi^l\right)}{\rho^l_{Fe}} + \frac{\xi^l}{\rho^l_O} - \frac{1}{\rho^s_{Fe}} - \xi^l\left(\frac{1}{\rho^l_O} - \frac{1}{\rho^l_{Fe}}\right)\\ &= \frac{1}{\rho^l_{Fe}} - \frac{1}{\rho^s_{Fe}}\\ &= V^l_{Fe} - V^s_{Fe} \equiv \Delta V^{s,l}_{Fe} \end{aligned} \quad (2.5.28)$$

is the change in specific volume between solid iron and liquid iron, derived by using (2.4.7), and

$$-s^s + s^l + \xi^l\frac{\partial \mu}{\partial T} \equiv \frac{L}{T} \quad (2.5.29)$$

is the latent heat of fusion per unit mass. The expression for the latent heat is similar to the standard definition of latent heat, $L = T\Delta s$, that appears in the usual Clausius-

Clapeyron relation (Moran *et al.*, 2010)

$$\frac{\mathrm{d}p}{\mathrm{d}T} = \frac{L}{T\Delta v},$$

where Δv is the change in specific volume of the phase transition. Definition (2.5.29) contains an extra contribution proportional to $\partial\mu/\partial T$ that is unique to the slurry system. The liquidus relation 2.5.27 is an important consequence of the fast-melting limit because it links the thermodynamic variables p, T and ξ^l everywhere in the slurry, therefore reducing the degree of thermodynamic freedom in the system. Increasing pressure will increase the liquidus temperature, while increasing the presence of light elements will depress the liquidus temperature.

The lever rule, μ_ϕ (2.5.18), together with the definition of the latent heat, (2.5.29) can be used to re-write the last term in the entropy differential (2.5.8) as

$$\left(\frac{\partial\mu_\phi}{\partial T}\right)_{p,\xi^l,\phi} = \frac{\partial}{\partial T}\left(\Phi^s - \Phi^l\right) = -s^s + s^l = \frac{L}{T} - \xi^l\frac{\partial\mu}{\partial T}, \tag{2.5.30}$$

hence (2.5.8) becomes

$$\mathrm{d}s = -\frac{\alpha}{\rho}\,\mathrm{d}p + \frac{c_p}{T}\,\mathrm{d}T - (1-\phi)\left(\frac{\partial\mu}{\partial T}\right)_{p,\xi^l,\phi}\mathrm{d}\xi^l - \left(\frac{L}{T} - \xi^l\frac{\partial\mu}{\partial T}\right)\mathrm{d}\phi. \tag{2.5.31}$$

In a similar manner, the phasal expansion coefficient can be re-written as

$$\alpha_\phi \equiv -\rho\left(\frac{\partial V}{\partial\phi}\right)_{p,T,\xi} = -\rho\frac{\partial}{\partial\phi}\left(\frac{\partial\Phi}{\partial p}\right)_{p,T,\xi} = -\rho\left(\frac{\partial\mu_\phi}{\partial p}\right)_{T,\xi,\phi}, \tag{2.5.32}$$

where we can apply the lever rule (2.5.19,2.5.20) and the definition of $\Delta V^{s,l}_{Fe,O}$ (2.5.25)

to (2.5.32), to get

$$\alpha_\phi = -\rho \frac{\partial}{\partial p}\left(\Phi^s - \Phi^l\right) = -\rho\left(V^s_{Fe} - V^l_{Fe,O}\right) = \rho \Delta V^{s,l}_{Fe,O}. \tag{2.5.33}$$

Hence the phasal expansion coefficient is the change in volume per unit mass upon melting.

2.6 Constitutive relations

To complete the conservation equations (2.2.7, 2.2.8, 2.2.15), the constitutive form of the light material flux $\mathbf{i}$, solid flux $\mathbf{j}$ and entropy flux $\mathbf{k}$ must be sought. In general, the fluxes can be written as any linear combination of the gradients of p, T and μ. Onsager noted that there are symmetry conditions that restrict the fluxes (Landau *et al.*, 1980), and the general form is given by

$$\mathbf{i} = -\left(a - h\xi^l\right)\nabla\mu - g\nabla T - \xi^l \mathbf{j}, \tag{2.6.1}$$

$$\mathbf{j} = \left(b\xi^l - h\right)\nabla\mu - f\nabla T, \tag{2.6.2}$$

$$\mathbf{k} = -(g - f\xi^l)\nabla\mu - c\nabla T, \tag{2.6.3}$$

where coefficients a to g are arbitrary. In writing these constitutive relations, we have applied the fast-melting limit and the constant solid assumption to reduce the constitutive relations given by equations 3.21-3.23 of Loper & Roberts (1977), and we have used the flux relation

$$\mathbf{i}' = \mathbf{i} + \xi^l \mathbf{j} \tag{2.6.4}$$

to write $\mathbf{i}'$ in terms of $\mathbf{i}$ and $\mathbf{j}$, and we set $h = 0$ without loss of generality since h only appears in combination with coefficients a and b (Loper & Roberts, 1980). Small-

scale responses of the light element mass flux to temperature gradients, also known as the Soret effect, are usually ignored as the relevant Soret coefficient is difficult to determine from first principles (Gubbins *et al.*, 2004) or experimentally (Rahman & Saghir, 2014). The solid flux is assumed to be independent of temperature and compositional gradients (Loper & Roberts, 1977). Substituting the chemical potential differential (2.5.9) into (2.6.1) and (2.6.2) gives

$$\mathbf{i} = -a\Delta V^{l}_{Fe,O}\nabla p - \left[a\left(\frac{\partial \mu}{\partial T}\right)_{p,\xi^l,\phi} + g\right]\nabla T - a\frac{\partial \mu}{\partial \xi^l}\nabla \xi^l - \xi^l \mathbf{j}, \tag{2.6.5}$$

$$\mathbf{j} = b\left(\xi^l \Delta V^{s,l}_{Fe,O} + \Delta V^{s,l}_{Fe}\right)\nabla p - \left[b\frac{L}{T} - b\xi^l\frac{\partial \mu}{\partial T} + f\right]\nabla T, \tag{2.6.6}$$

where ignoring Soret effects implies that

$$\begin{aligned} f &= -b\left(\frac{L}{T} - \xi^l \frac{\partial \mu}{\partial T}\right), \\ g &= -a\frac{\partial \mu}{\partial T}, \end{aligned} \tag{2.6.7}$$

which is also given in Loper & Roberts (1980).

Upon substitution of $\Delta V^{s,l}_{Fe}$ (2.5.28) and the liquidus (2.5.27) into (2.6.5), the light element flux becomes

$$\mathbf{i} = -\frac{\rho^l_{Fe} D' \Delta V^{s,l}_{Fe,O}}{\xi^l \left(\partial \mu / \partial \xi^l\right)}\nabla p + \frac{\rho^l_{Fe} D' L}{T\xi^l \left(\partial \mu / \partial \xi^l\right)}\nabla T - \xi^l \mathbf{j}, \tag{2.6.8}$$

where

$$a \equiv \rho^l_{Fe} D' / \left(\partial \mu / \partial \xi^l\right), \tag{2.6.9}$$

and D' is the self-diffusion coefficient of the light material (Landau & Lifshitz, 1959), which measures the diffusion coefficient of a species in the absence of a chemical potential gradient. The first term in (2.6.8) corresponds to the barodiffusion of light

material in the slurry and occurs whether solid material is present or not. Barodiffusion occurs when material diffuses from a higher pressure to a lower pressure. The "Soret"-like behaviour in the second term of (2.6.8) is caused by variations in $\nabla\xi^l$ that depend on ∇p and ∇T through the liquidus. The last term accounts for the light element that is displaced by the flux of solid particles snowing under gravity.

Substituting (2.5.28) into (2.6.6) and using (2.6.7) yields the solid flux

$$\mathbf{j} = b(\phi)\Delta V^{s,l}_{Fe,O}\nabla p, \tag{2.6.10}$$

where $b(\phi)$ is the sedimentation coefficient with dimension $\mathrm{kg\ s\ m^{-3}}$. The mass flux, $\mathbf{j}$, describes how the solid particles fall through the liquid in response to gravity, which is proportional to the pressure gradient, and has dimension $\mathrm{kg\ m^{-2}\ s^{-1}}$. The sole purpose of the sedimentation coefficient is to relate the solid fraction, ϕ, with the solid flux, $\mathbf{j}$, and its form will be developed later in Section 2.7.

Turning attention to the entropy flux in order to complete the entropy equation (2.2.15), then (2.6.3) can be re-written

$$\mathbf{k} = -\left[a\frac{\partial\mu}{\partial T} + b\xi^l\left(\frac{L}{T} - \xi^l\frac{\partial\mu}{\partial T}\right)\right]\nabla\mu - \left[\frac{k}{T} + b\left(\frac{L}{T} - \xi^l\frac{\partial\mu}{\partial T}\right)^2 + a\left(\frac{\partial\mu}{\partial T}\right)^2\right]\nabla T, \tag{2.6.11}$$

where coefficients f and g (2.6.7) are replaced, and

$$c \equiv \frac{k}{T} + \frac{f^2}{b} + \frac{g^2}{a}. \tag{2.6.12}$$

Substituting the chemical potential differential (2.5.9) into (2.6.11) gives

$$\begin{aligned}\mathbf{k} = &-\left[-a\frac{\partial\mu}{\partial T}+b\xi^l\left(\frac{L}{T}-\xi^l\frac{\partial\mu}{\partial T}\right)\right]\left[\Delta V_{Fe}^{s,l}\nabla p+\frac{\partial\mu}{\partial T}\nabla T+\frac{\partial\mu}{\partial\xi^l}\nabla\xi^l\right]\\ &-\left[\frac{k}{T}+b\left(\frac{L^2}{T^2}-2\frac{L\xi^l}{T}\frac{\partial\mu}{\partial T}+\left(\xi^l\frac{\partial\mu}{\partial T}\right)^2\right)+a\left(\frac{\partial\mu}{\partial T}\right)^2\right]\nabla T.\end{aligned} \tag{2.6.13}$$

We eliminate $\nabla\xi^l$ using the liquidus (2.5.27) to get

$$\begin{aligned}\mathbf{k} = &-\left[-a\frac{\partial\mu}{\partial T}+b\xi^l\left(\frac{L}{T}-\xi^l\frac{\partial\mu}{\partial T}\right)\right]\left[\frac{\Delta V_{Fe,O}^{s,l}}{\xi^l}\nabla p+\left(\frac{\partial\mu}{\partial T}-\frac{L}{T\xi^l}\right)\nabla T\right]\\ &-\left[\frac{k}{T}+b\left(\frac{L^2}{T^2}-2\frac{L\xi^l}{T}\frac{\partial\mu}{\partial T}+\left(\xi^l\frac{\partial\mu}{\partial T}\right)^2\right)+a\left(\frac{\partial\mu}{\partial T}\right)^2\right]\nabla T,\end{aligned} \tag{2.6.14}$$

where the relation between the changes in specific volumes (2.5.28) is used to obtain $\Delta V_{Fe,O}^{s,l}$. The terms in (2.6.14) cancel to give

$$\begin{aligned}\mathbf{k} &= a\frac{\partial\mu}{\partial T}\frac{\Delta V_{Fe,O}^{s,l}}{\xi^l}\nabla p-a\frac{\partial\mu}{\partial T}\frac{L}{T\xi^l}\nabla T+b\xi^l\frac{\partial\mu}{\partial T}\Delta V_{Fe,O}^{s,l}\nabla p-b\frac{L}{T}\Delta V_{Fe,O}^{s,l}\nabla p-\frac{k}{T}\nabla T\\ &= -\frac{\partial\mu}{\partial T}\left[-a\frac{\Delta V_{Fe,O}^{s,l}}{\xi^l}\nabla p+a\frac{L}{T\xi^l}\nabla T-\xi^l\mathbf{j}\right]-\frac{L}{T}\mathbf{j}-\frac{k}{T}\nabla T,\end{aligned} \tag{2.6.15}$$

where the definition of the solid flux, (2.6.10) has been applied. Equation (2.6.15) finally reduces to

$$\mathbf{k} = -\frac{\partial\mu}{\partial T}\mathbf{i}-\frac{L}{T}\mathbf{j}-\frac{k}{T}\nabla T, \tag{2.6.16}$$

where the definition of the light element flux, (2.6.8), has been applied.

Under the fast-melting limit (2.5.21), the energy flux can be defined as (Loper & Roberts, 1977)

$$\mathbf{q} = \mu\mathbf{i}+T\mathbf{k} = \left(\mu-T\frac{\partial\mu}{\partial T}\right)\mathbf{i}-L\mathbf{j}-k\nabla T, \tag{2.6.17}$$

where $\mu - T\frac{\partial\mu}{\partial T}$ is the heat of reaction (Gubbins *et al.*, 2004).

Dissipation due to fluxes (2.2.16), together with the phase equilibrium condition (2.5.21), constant solid assumption (2.3.5) and the flux relation (2.6.4), reduces to

$$\begin{aligned} Q_D &= -\mathbf{i}' \cdot \nabla\mu - \mathbf{j} \cdot \left(\nabla\mu_\phi + \mu\nabla\xi^l\right) - \mathbf{k} \cdot \nabla T \\ &= -\mathbf{i}' \cdot \nabla\mu - \mathbf{j} \cdot \nabla\xi^l\mu - \mathbf{j} \cdot \mu\nabla\xi^l - \mathbf{k} \cdot \nabla T \\ &= -\mathbf{i}' \cdot \nabla\mu + \xi^l\mathbf{j} \cdot \nabla\mu - \mathbf{k} \cdot \nabla T \\ &= -\mathbf{i} \cdot \nabla\mu - \mathbf{k} \cdot \nabla T. \end{aligned} \tag{2.6.18}$$

To derive a temperature equation for the slurry, the exact differential of the entropy (2.5.8) and (2.6.18) is substituted into entropy equation (2.2.15) to give

$$-\alpha T\frac{\mathrm{D}p}{\mathrm{D}t}+\rho_0 c_p\frac{\mathrm{D}T}{\mathrm{D}t}-\rho_0 T\frac{\partial\mu}{\partial T}\frac{\mathrm{D}\xi^l}{\mathrm{D}t}-\rho_0 L\frac{\mathrm{D}\phi}{\mathrm{D}t}+\rho_0 T\frac{\partial\mu}{\partial T}\xi^l\frac{\mathrm{D}\phi}{\mathrm{D}t}+T\nabla\cdot\mathbf{k}=\rho_0 H-\mathbf{i}\cdot\nabla\mu-\mathbf{k}\cdot\nabla T. \tag{2.6.19}$$

where the viscous dissipation, Q_ν, is neglected under the Boussinesq approximation, and the fast-melting limit means dissipation due to melting and freezing, Q_M, is equal to zero (see equation 2.3.4). Using (2.3.7) and $\nabla \cdot T\mathbf{k} = T\nabla \cdot \mathbf{k} + \mathbf{k} \cdot \nabla T$, we can re-write (2.6.19) as

$$-\alpha T\frac{\mathrm{D}p}{\mathrm{D}t}+\rho_0 c_p\frac{\mathrm{D}T}{\mathrm{D}t}-\rho_0 T\frac{\partial\mu}{\partial T}\frac{\mathrm{D}\xi}{\mathrm{D}t}-\rho_0 L\frac{\mathrm{D}\phi}{\mathrm{D}t}=\rho_0 H-\mathbf{i}\cdot\nabla\mu-\nabla\cdot T\mathbf{k}. \tag{2.6.20}$$

Substituting the entropy flux vector (2.6.16) into (2.6.20) gives

$$\begin{aligned} \rho_0 c_p\frac{\mathrm{D}T}{\mathrm{D}t}-\alpha T\frac{\mathrm{D}p}{\mathrm{D}t} &= \rho_0 T\frac{\partial\mu}{\partial T}\frac{\mathrm{D}\xi}{\mathrm{D}t}+\rho_0 L\frac{\mathrm{D}\phi}{\mathrm{D}t}-\mathbf{i}\cdot\nabla\mu-\nabla\cdot\left(-\frac{\partial\mu}{\partial T}\mathbf{i}-\frac{L}{T}\mathbf{j}-\frac{k}{T}\nabla T\right) \\ &\quad +\rho_0 H \\ &= \nabla\cdot k\nabla T+\rho_0 L\frac{\mathrm{D}\phi}{\mathrm{D}T}+L\nabla\cdot\mathbf{j}-\mathbf{i}\cdot\nabla\left(\mu-T\frac{\partial\mu}{\partial T}\right)+\rho_0 H, \end{aligned} \tag{2.6.21}$$

where the conservation of light element (2.2.7) has been used. For the sake of simplicity radiogenic heating, $\rho_0 H$, is ignored in (2.6.21). Pressure heating, $-\alpha T \frac{\mathrm{D}p}{\mathrm{D}t}$, is the heat released by an isothermal increase in pressure (Gubbins *et al.*, 2003). The heat of reaction is $\mu - T\frac{\partial \mu}{\partial T}$, which is released when the Fe-O alloy dissociates, and is absorbed as the oxygen recombines in the outer core (Gubbins *et al.*, 2004). Heat of reaction and pressure heating are often ignored in the literature, as their estimated values are small compared to the other terms (Davies, 2015; Gubbins *et al.*, 2003, 2004; Nimmo, 2015a) and we have already assumed that the solid and liquid phases do not interact chemically when applying the lever rule. Therefore (2.6.21) becomes the temperature equation

$$\rho_0 c_p \frac{\mathrm{D}T}{\mathrm{D}t} = \nabla \cdot (k \nabla T + L\mathbf{j}) + \rho_0 L \frac{\mathrm{D}\phi}{\mathrm{D}T}, \tag{2.6.22}$$

which is similar to the conventional temperature equation for Rayleigh-Bénard convection (Chandrasekhar, 1961), except that there is an extra term to account for the latent heat release due to phase change, which is proportional to the rate of freezing, $m^s = \rho_0 \frac{\mathrm{D}\phi}{\mathrm{D}t} + \nabla \cdot \mathbf{j}$ (2.2.8).

2.7 Sedimentation

For the sake of simplicity, in our model of sedimentation, we assume that the solid iron crystals are uniformly spherical particles falling with gravity against viscous drag. According to Stokes' law (Kundu *et al.*, 2015), the drag force acting on a single solid particle with radius R is defined as

$$\mathbf{F_d} = (\rho^s_{Fe} - \rho_0) \frac{4\pi R^3}{3} \mathbf{g} = \rho^s_{Fe} \Delta V^{s,l}_{Fe,O} \frac{4\pi R^3}{3} \nabla p, \tag{2.7.1}$$

where (2.5.25) is used to re-write the specific densities in terms of the change in specific volume, $\Delta V^{s,l}_{Fe,O}$, and hydrostatic equilibrium (2.2.13) is assumed. The flux of solid caused by a pressure gradient is

$$\mathbf{j} = \rho_0 \phi M \mathbf{F_d}, \tag{2.7.2}$$

where

$$M = \frac{1}{6\pi\rho_0 \nu R}, \tag{2.7.3}$$

is the average mobility of the solid particle (Landau & Lifshitz, 1959), and recall that ν is the kinematic viscosity. Equating (2.7.2) with (2.6.10) gives

$$b\left(\phi\right) = \rho^s_{Fe}\rho_0\phi M v = \left(\frac{v^2}{6\pi^2}\right)^{\frac{1}{3}} \frac{\rho^s_{Fe}\phi}{3\nu} = \left(\frac{\rho^s_{Fe}\rho_0^2}{162\pi^2\nu^3 N^2}\right)^{1/3} \phi^{5/3}, \tag{2.7.4}$$

where

$$v = \frac{4\pi R^3}{3} = \frac{\rho_0\phi}{\rho^s_{Fe}N} \tag{2.7.5}$$

is the volume of an individual solid particle in terms of ϕ, and N is the number of particles per unit volume (Loper & Roberts, 1980). Note that the dimension of the sedimentation coefficient, $b(\phi)$, is $\mathrm{kg\ m^{-3}\ s}$. If there are a small number of very large particles or a large number of very small particles, then both scenarios can produce the same solid flux. There is no likely indication of what the particle size should be from observations to constrain N, hence by considering solutions of $\mathbf{j}$ there is no need to evaluate ϕ. Our model of the slurry is based on the premise that $\phi \ll 1$, so that solid iron is a small component of a mostly liquid slurry. In this model of mobility there is currently no capacity for the kinematic viscosity, ν, to change depending on ϕ in this model. If ϕ exceeds a critical value then a larger presence of solid particles in the suspension would start to inhibit shear, therefore increasing the effective viscosity. It

is possible that once the solid fraction exceeds a critical value, bridging of iron crystals may occur and the slurry could transition to a mush (Loper & Roberts, 1987). Other more sophisticated models of sedimentation and mobility (for example, crystallisation of magma oceans (Solomatov, 2007)) could be incorporated into $b(\phi)$ to account for factors such as particle shapes and hindered particle transport, which is beyond the scope of this thesis.

2.8 Jump conditions

In this section jump conditions at the lower ICB and upper core-slurry boundary (CSB) for the slurry system are derived from first principles. In general, Leibniz's rule for integrating a scalar quantity f over a volume that changes over time, $V(t)$, is

$$\frac{\mathrm{d}}{\mathrm{d}t}\iiint_{V(t)} f\,\mathrm{d}V = \iiint_{V(t)} \frac{\partial f}{\partial t}\mathrm{d}V + \oint_{A_t} f\mathbf{U}_t\cdot\mathbf{n}\,\mathrm{d}S - \iint_{S_b} f\mathbf{U}_b\cdot\mathbf{n}\,\mathrm{d}S, \quad (2.8.1)$$

where $\mathbf{U}$ is the velocity of the end face in which the subscripts t and b refer to the top and bottom surfaces A_t and A_b respectively (see Figure 2.1).

We denote that $\langle a\rangle = a^{sl} - a^{l/s}$ is the jump in quantity a, with superscripts sl and l/s denoting the value in the slurry and in the liquid/solid. We assume the continuity of temperature

$$\langle T\rangle = 0, \quad (2.8.2)$$

at both layer boundaries, and the continuity of light element in the liquid phase

$$\langle \xi^l\rangle = 0, \quad (2.8.3)$$

at both boundaries, since both of these variables are governed by diffusive equations.

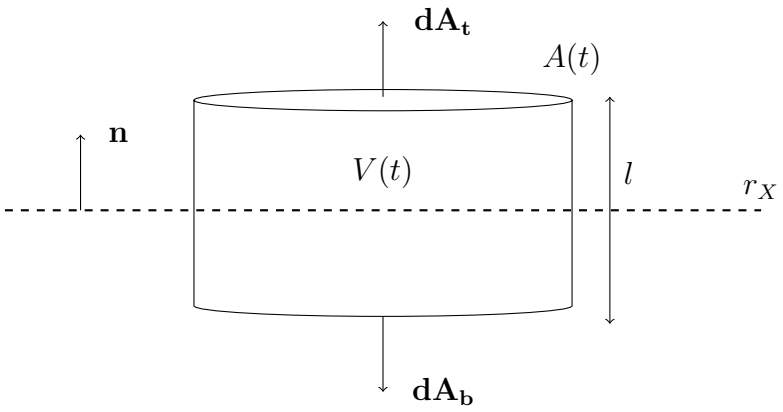

Figure 2.1: A Gaussian pillbox with volume $V(t)$ enclosed by area $A(t)$ spanning a slurry interface, r_X. Areas of the end faces are denoted by $\mathbf{dA_t}$ and $\mathbf{dA_b}$, separated by a distance l, and $\mathbf{n}$ is the normal vector.

2.8.1 Conservation of mass

Consider the continuity equation in the rest frame,

$$\frac{\partial \rho}{\partial t} + \nabla \cdot (\rho \mathbf{u}) = 0. \tag{2.8.4}$$

Integrating over a pill-box, $V(t)$, that straddles the interface r_X, gives

$$\int_{V(t)} \frac{\partial \rho}{\partial t}\, dV = - \oint_{A(t)} \rho \mathbf{u} \cdot \mathbf{n}\, dA, \tag{2.8.5}$$

where the divergence theorem has been applied. Applying Leibniz's rule gives

$$\frac{\mathrm{d}}{\mathrm{d}t} \int_{V(t)} \rho\, dV - \oint_{A_t} \rho \mathbf{U_t} \cdot \mathbf{n}\, dA + \oint_{A_b} \rho \mathbf{U_b} \cdot \mathbf{n}\, dA = - \oint_{A(t)} \rho \mathbf{u} \cdot \mathbf{n}\, dA. \tag{2.8.6}$$

We take $\mathbf{U_b} = 0$ and re-write $\mathbf{U_t} = \mathbf{U}$ without loss of generality, since only the relative velocity $\mathbf{u} - \mathbf{U}$ between the fluid and the moving volume is important. As $V(t) \to 0$, then

$$\oint_{A(t)} \rho\, (\mathbf{u} - \mathbf{U}) \cdot \mathbf{n}\, \mathrm{d}A = 0,$$

therefore we obtain the pillbox condition

$$\langle \rho \left(\mathbf{u} - \mathbf{U} \right) \rangle \cdot \mathbf{n} = 0, \tag{2.8.7}$$

that conserves mass at the boundaries.

2.8.2 Conservation of solid

The conservative form of the solid equation is

$$\frac{\partial}{\partial t} \left(\rho \phi \right) = -\nabla \left(\rho \phi \mathbf{u} + \mathbf{j} \right) + m^s.$$

Integrating over the pillbox volume gives

$$\int_{V(t)} \frac{\partial}{\partial t} \left(\rho \phi \right) \, \mathrm{d}V = - \oint_{A(t)} \left(\rho \phi \mathbf{u} + \mathbf{j} \right) \cdot \mathbf{n} \, \mathrm{d}A + \int_{V(t)} m^s \, \mathbf{d}V.$$

Applying Leibniz's rule, taking $\mathbf{U_b} = 0$ and re-writing $\mathbf{U_t} = \mathbf{U}$ gives

$$\frac{\mathrm{d}}{\mathrm{d}t} \int_{V(t)} \rho \phi \, \mathrm{d}V - \oint_{A_t} \rho \phi \mathbf{U} \cdot \mathbf{n} \, \mathrm{d}A_t = - \oint_{A(t)} \left(\rho \phi \mathbf{u} + \mathbf{j} \right) \cdot \mathbf{n} \, \mathrm{d}A + \int_{V(t)} m^s \, \mathbf{d}V.$$

As the pillbox volume vanishes, we are left with

$$\oint_{A(t)} \left(\rho \phi \left(\mathbf{u} - \mathbf{U} \right) + \mathbf{j} \right) \cdot \mathbf{n} \, \mathrm{d}A = 0,$$

which yields the pillbox condition

$$\langle \rho \phi \left(\mathbf{u} - \mathbf{U} \right) \rangle \cdot \mathbf{n} + \langle \mathbf{j} \rangle \cdot \mathbf{n} = 0. \tag{2.8.8}$$

No new particles nucleate at the boundaries as solid is conserved there, so the inner core is assumed to grow entirely by the accumulation of iron particles settling onto the ICB under the influence of gravity.

2.8.3 Conservation of total energy

In general, the conservative form of the internal energy equation is

$$\frac{\partial}{\partial t}\left(\rho E\right) = -\nabla \cdot \left(\mathbf{q} + \rho E \mathbf{u}\right), \tag{2.8.9}$$

where the energy flux vector, $\mathbf{q}$ is given by (2.6.17)

$$\mathbf{q} = -L\mathbf{j} - k\nabla T. \tag{2.8.10}$$

after neglecting the heat of reaction. We dot the more general form of the momentum equation (2.2.14) with $\mathbf{u}$ to obtain the kinetic energy equation

$$\frac{\partial}{\partial t}\left(\frac{\rho u^2}{2}\right) = -\mathbf{u} \cdot \nabla\left(\frac{\rho u^2}{2}\right) - \mathbf{u} \cdot \nabla p + \underline{\underline{\sigma}}' \cdot \mathbf{u} + \rho \mathbf{u} \cdot \mathbf{F}, \tag{2.8.11}$$

where $\underline{\underline{\sigma}}'$ is the deviatoric stress tensor and $\mathbf{F}$ are external body forces, and includes the buoyancy force, $\mathbf{f_b} = -\nabla\psi$, in which ψ is the gravitational potential. The equation for total energy is therefore

$$\frac{\partial}{\partial t}\left(\rho\left(E + \frac{u^2}{2}\right)\right) = \rho \mathbf{u} \cdot \mathbf{F} - \nabla \cdot \left[\rho\left(E + \frac{u^2}{2}\right)\mathbf{u} + p\mathbf{u} - \underline{\underline{\sigma}}' \cdot \mathbf{u} + \mathbf{q}\right]. \tag{2.8.12}$$

Applying the pillbox argument to this equation yields the condition (Loper & Roberts, 1987)

$$\mathbf{n}\cdot\rho\left(\mathbf{u}-\mathbf{U}\right)\langle E+\frac{u^2}{2}+\frac{p}{\rho}\rangle+\mathbf{n}\cdot\langle-\underline{\underline{\sigma}}'\cdot\left(\mathbf{u}-\mathbf{U}\right)+\mathbf{q}\rangle=0, \tag{2.8.13}$$

where (2.8.7) is used to remove the jump in mass. The Gibbs free energy is related to the total internal energy by (Landau *et al.*, 1980)

$$\Phi=E-Ts+\frac{p}{\rho}.$$

Evaluating the jump in Gibbs free energy at the boundaries and re-arranging gives

$$\langle E+\frac{p}{\rho}\rangle=\langle\Phi\rangle+T\langle s\rangle, \tag{2.8.14}$$

where we have assumed the continuity of temperature (2.8.2). To evaluate the Gibbs free energy term, we combine the lever rule (2.5.11) and the condition for phase equilibrium (2.5.22) to get

$$\Phi=\Phi^l(p,T,\xi^l)-\phi\xi^l\mu(p,T,\xi^l),$$

where μ is dependent on the thermodynamic variables p, T and ξ^l. We assume that $\langle p\rangle=0$ since viscosity and velocity jumps are assumed to have a small effect on the normal component of the stress at the interface (Loper & Roberts, 1987). If pressure, temperature and ξ^l are continuous across the interface, then so are Φ^l and μ. Therefore the jump in Gibbs free energy is given by

$$\langle\Phi\rangle=-\xi^l\mu\langle\phi\rangle. \tag{2.8.15}$$

Similarly for the entropy term, we use the lever rule (2.5.17) and the definition of the latent heat (2.5.29) to obtain

$$s = s^l + \phi\left(\xi^l \frac{\partial \mu}{\partial T} - \frac{L}{T}\right). \tag{2.8.16}$$

Therefore

$$T\langle s\rangle = -\langle\phi\rangle\left(L - T\xi^l \frac{\partial \mu}{\partial T}\right), \tag{2.8.17}$$

where s^l, L and $\frac{\partial \mu}{\partial T}$ are assumed to be continuous. Substituting (2.8.15) and (2.8.16) into (2.8.14) gives

$$\langle E + \frac{p}{\rho}\rangle = -\langle\phi\rangle\left(L + \xi^l\left(\mu - T\frac{\partial \mu}{\partial T}\right)\right). \tag{2.8.18}$$

After ignoring viscous stresses, $\underline{\underline{\sigma}}'$, (since we are working in the Boussinesq framework), the heat of reaction, and assuming that jumps in kinetic energy are small ($\langle\frac{u^2}{2}\rangle = 0$), we can use (2.8.18) and the energy flux vector, (2.8.10), to express (2.8.13) as

$$\mathbf{n}\cdot\rho L\langle\phi\rangle\left(\mathbf{u} - \mathbf{U}\right) + \mathbf{n}\cdot\langle L\mathbf{j} + k\nabla T\rangle = 0. \tag{2.8.19}$$

By using the jump condition on the solid mass (2.8.8), then (2.8.19) can be re-written as

$$\mathbf{n}\cdot\langle k\nabla T\rangle = 0. \tag{2.8.20}$$

In other words, condition (2.8.20) says that the heat flux across the slurry interface is continuous.

More specific boundary conditions for the steady state models (Chapter 3 and 4) and time-dependent model (Chapter 5) are developed in the proceeding chapters, since they differ depending on the assumptions made.

2.9 Governing equations

In summary the reduced equations of a Boussinesq slurry are

$$\xi = (1-\phi)\xi^l, \tag{2.9.1a}$$

$$\rho_0 \frac{\mathrm{D}\xi}{\mathrm{D}t} = -\nabla \cdot \mathbf{i}, \tag{2.9.1b}$$

$$\rho_0 \frac{\mathrm{D}\phi}{\mathrm{D}t} = -\nabla \cdot \mathbf{j} + m^s, \tag{2.9.1c}$$

$$\rho_0 c_p \frac{\mathrm{D}T}{\mathrm{D}t} = \nabla \cdot (k\nabla T + L\mathbf{j}) + \rho_0 L \frac{\mathrm{D}\phi}{\mathrm{D}t}, \tag{2.9.1d}$$

$$\nabla T = \frac{T\Delta V_{Fe}^{s,l}}{L}\nabla p - \frac{T\xi^l\left(\partial\mu/\partial\xi^l\right)}{L}\nabla\xi^l, \tag{2.9.1e}$$

$$\mathbf{i} = -\frac{\rho_0 D' \Delta V_{Fe,O}^{s,l}}{\xi^l\left(\partial\mu/\partial\xi^l\right)}\nabla p + \frac{\rho_0 D' L}{T\xi^l\left(\partial\mu/\partial\xi^l\right)}\nabla T - \xi^l\mathbf{j}, \tag{2.9.1f}$$

$$\mathbf{j} = b(\phi)\Delta V_{Fe,O}^{s,l}\nabla p, \tag{2.9.1g}$$

$$\nabla \cdot \mathbf{u} = 0, \tag{2.9.1h}$$

$$\frac{\mathrm{D}\mathbf{u}}{\mathrm{D}t} = -\nabla\left(\frac{p'}{\rho_0}\right) + \frac{\rho'}{\rho_0}\mathbf{g} + \nu\nabla^2\mathbf{u} + \mathbf{F}, \tag{2.9.1i}$$

$$\rho' = \rho_0\left[-\alpha T' - \alpha^\xi \xi' + \alpha_\phi \phi'\right]. \tag{2.9.1j}$$

The governing equations are subject to the jump conditions

$$\langle \rho\left(\mathbf{u}-\mathbf{U}\right)\rangle \cdot \mathbf{n} = 0 \tag{2.9.2a}$$

$$\langle \rho\phi\left(\mathbf{u}-\mathbf{U}\right)\rangle \cdot \mathbf{n} + \langle \mathbf{j}\rangle \cdot \mathbf{n} = 0 \tag{2.9.2b}$$

$$\langle k\nabla T\rangle \cdot \mathbf{n} = 0 \tag{2.9.2c}$$

at the ICB and CSB.

A list of symbols used in this chapter is presented in Table 2.1.

Symbol	Definition	Units
ξ	Light element concentration	
ξ^l	Light element concentration in the liquid phase	
ϕ	Solid fraction	
T	Temperature	K
p	Pressure	Pa
p'	Reduced pressure	Pa
ρ_0	Reference density	kgm^{-3}
ρ'	Density variation	kgm^{-3}
$\mathbf{u}$	Flow velocity	$\mathrm{m\ s}^{-1}$
$\mathbf{i}$	Light element flux vector	$\mathrm{kg\ m}^{-2}\ \mathrm{s}^{-1}$
$\mathbf{j}$	Solid mass flux vector	$\mathrm{kg\ m}^{-2}\ \mathrm{s}^{-1}$
$\mathbf{k}$	Entropy flux vector	J
$b(\phi)$	Sedimentation coefficient	$\mathrm{kg\ m}^{-3}\ \mathrm{s}$
m^s	Creation rate of solid particles	$\mathrm{kg\ m}^{-3}\ \mathrm{s}^{-1}$
M_O^l	Mass of liquid oxygen	kg
M_{Fe}^l	Mass of liquid iron	kg
M_{Fe}^s	Mass of solid iron	kg
ρ_O	Specific density of light element	$\mathrm{kg\ m}^{-3}$
ρ_{Fe}^l	Specific density of liquid iron, reference density	$\mathrm{kg\ m}^{-3}$
$\rho_{Fe}^s\ (\rho^s)$	Specific density of solid	$\mathrm{kg\ m}^{-3}$
$\Delta V_{Fe,O}^l\ (\bar{\delta})$	Change in specific volume between light element and liquid iron	$\mathrm{kg}^{-1}\ \mathrm{m}^3$
$\Delta V_{Fe,O}^{s,l}\ (\Delta V)$	Change in specific volume between liquid and solid phase	$\mathrm{kg}^{-1}\ \mathrm{m}^3$

$\Delta V_{Fe}^{s,l}$ (δ)	Change in specific volume between liquid iron and solid iron	$\mathrm{kg}^{-1}\ \mathrm{m}^3$
Φ	Gibbs free energy	J
V	Specific volume	$\mathrm{m}^3\mathrm{kg}^{-1}$
s	Specific entropy	JK^{-1}
μ (μ^l)	Chemical potential of light element relative to iron	$\mathrm{J\ kg}^{-1}$
μ_ϕ (ψ)	Chemical potential of solid relative to the liquid	$\mathrm{J\ kg}^{-1}$
β	Isothermal compressibility	Pa^{-1}
α	Thermal expansion coefficient	K^{-1}
α_ξ $(\bar{\alpha})$	Compositional expansion coefficient	
α_ϕ	Phasal expansion coefficient	
c_p (C_p)	Specific heat capacity	$\mathrm{J\ kg}^{-1}\ \mathrm{K}^{-1}$
$\partial\mu/\partial T$ $(-\bar{s})$	Thermodynamic derivative of chemical potential w.r.t. T	$\mathrm{J\ kg}^{-1}\mathrm{K}^{-1}$
$\partial\mu/\partial\xi^l$ $(\bar{\mu})$	Thermodynamic derivative of chemical potential w.r.t. ξ^l	$\mathrm{J\ kg}^{-1}$
k	Thermal conductivity	$\mathrm{W\ m}^{-1}\ \mathrm{K}^{-1}$
L	Latent heat of fusion	$\mathrm{J\ kg}^{-1}$
D'	ξ^l self–diffusion coefficient	$\mathrm{m}^2\mathrm{s}^{-1}$

Table 2.1: Symbols commonly used in the reduced slurry theory. For ease of reference, the corresponding notation used in Loper & Roberts (1977, 1980, 1987); Roberts & Loper (1987) is provided in brackets.

2.10 Global energy balance

We consider the conservation of energy in the whole core and derive the global energy balance that includes a slurry layer at the base of the outer core. The heat flux across the CMB, Q^c, is extracted by the mantle out of the core. A high CMB heat flow indicates that the core is rapidly cooling. We show that energy is derived from three key sources: secular cooling, Q_s, latent heat, Q_L, gravitational power, Q_g[1].

The global energy balance will be used to constrain solutions to the slurry model in future chapters. As discussed in Chapter 1, the CMB heat flow cannot exceed 17 TW. Geophysically relevant solutions of the slurry model should therefore be consistent with the core thermal history and power requirements for operating the geodynamo.

Consider a core volume $V(t)$ bounded by a surface $A(t)$, where there is no mass exchange at the CMB. We assume there is a no normal flow at the CMB, therefore $\mathbf{u} \cdot \hat{\mathbf{n}} = 0$ there. The time-scale of interest is long compared to the scale of convective motions but short compared to geological time-scales.

Recall the general continuity and momentum equations with no rotation and no magnetic field

$$\frac{\mathrm{D}\rho}{\mathrm{D}t} = -\rho \frac{\partial u_i}{\partial x_i}, \tag{2.10.1}$$

$$\rho \frac{\mathrm{D}u_i}{\mathrm{D}t} = \rho \frac{\partial \psi}{\partial x_i} + \frac{\partial \tau_{ij}}{\partial x_j}, \tag{2.10.2}$$

which are written in tensor notation using the Einstein summation convention, where ψ is the gravitational potential in which $g_i = \frac{\partial \psi}{\partial x_i}$. Note that we assume that the Boussinesq approximation applies to the slurry volume only and not the rest of the liquid outer core when deriving the global energy balance. The Boussinesq approximation is

[1] We neglect the heat of reaction, pressure freezing and internal heating - see discussion following (2.6.21)

used when considering the equation of state (2.9.1j) to eliminate compressible effects in the slurry.

To find the rate of change of kinetic energy, we dot (2.10.2) with $\mathbf{u}$ to get

$$\rho \frac{\mathrm{D}}{\mathrm{D}t}\left(\frac{u_i^2}{2}\right) = \rho u_i \frac{\partial \psi}{\partial x_i} + u_i \frac{\partial \tau_{ij}}{\partial x_j}, \tag{2.10.3}$$

where $u_i^2 = u_i u_i = u_1^2 + u_2^2 + u_3^2$. Consider the total work done on the fluid element by surface forces, $\frac{\partial}{\partial x_j}(u_i \tau_{ij})$, and the identity

$$\frac{\partial}{\partial x_j}(u_i \tau_{ij}) \equiv \tau_{ij} \frac{\partial u_i}{\partial x_j} + u_i \frac{\partial \tau_{ij}}{\partial x_j}. \tag{2.10.4}$$

The first term on the RHS is the work done by viscous deformation which increases the internal energy, and the second term on the RHS is the increase in kinetic energy as local fluid is advected due to differences in stress on a fluid element. The total stress tensor for a Newtonian fluid is

$$\tau_{ij} \equiv -p\delta_{ij} + \sigma_{ij} = -p\delta_{ij} + 2\eta e_{ij} - \frac{2}{3}\eta\left(\nabla \cdot \mathbf{u}\right)\delta_{ij}, \tag{2.10.5}$$

where η is the dynamic viscosity. The product $\tau_{ij}\frac{\partial u_i}{\partial x_j}$ is equal to τ_{ij} times the symmetric part of $\frac{\partial u_i}{\partial x_j}$ denoted by e_{ij} (Kundu *et al.*, 2015), therefore the rate of work done by deformation is

$$\begin{aligned} \tau_{ij}\frac{\partial u_i}{\partial x_j} = \tau_{ij} e_{ij} &= -p\delta_{ij}e_{ij} + 2\eta e_{ij}e_{ij} - \frac{2}{3}\eta\left(\nabla \cdot \mathbf{u}\right)\delta_{ij}e_{ij} \\ &= -p\left(\nabla \cdot \mathbf{u}\right) + 2\eta e_{ij}e_{ij} - \frac{2}{3}\eta\left(\nabla \cdot \mathbf{u}\right)^2, \end{aligned} \tag{2.10.6}$$

where

$$e_{ij} = \frac{1}{2}\left(\frac{\partial u_i}{\partial x_j} + \frac{\partial u_j}{\partial x_i}\right), \tag{2.10.7}$$

and $e_{ij}\delta_{ij} = e_{ii} = \nabla \cdot \mathbf{u}$. Substituting (2.10.4) and (2.10.6) back into the kinetic energy equation (2.10.3) gives

$$\rho \frac{\mathrm{D}}{\mathrm{D}t}\left(\frac{u_i^2}{2}\right) = \rho u_i \frac{\partial \psi}{\partial x_i} + \frac{\partial}{\partial x_j}\left(u_i \tau_{ij}\right) + p\nabla \cdot \mathbf{u} - \phi_\nu, \tag{2.10.8}$$

where $\phi_\nu = 2\eta e_{ij}e_{ij} - \frac{2}{3}\eta\left(\nabla \cdot \mathbf{u}\right)^2$ is the rate of viscous dissipation. The term $p\nabla \cdot \mathbf{u}$ represents the rate of work done by volume expansion. Integrating (2.10.8) gives the integral equation for the kinetic energy

$$\frac{\mathrm{d}}{\mathrm{d}t}\int_V \frac{\rho u^2}{2}\,\mathrm{d}V = \int_V \rho u_i \frac{\partial \psi}{\partial x_i}\,\mathrm{d}V + \oint_A u_i \tau_{ij}\,\mathrm{d}A_j + \int_V p\nabla \cdot \mathbf{u}\,\mathrm{d}V - \int_V \phi_\nu\,\mathrm{d}V. \tag{2.10.9}$$

To find the rate of change of the total energy, we need to also consider the internal energy of the system in addition to the kinetic energy. The equation of internal energy is given by (Loper & Roberts, 1977)

$$\rho \frac{\mathrm{D}E}{\mathrm{D}t} = -\frac{\partial q_i}{\partial x_i} - p\nabla \cdot \mathbf{u} + \phi_\nu, \tag{2.10.10}$$

where

$$\rho \frac{\mathrm{D}E}{\mathrm{D}t} = \frac{p}{\rho}\frac{\mathrm{D}\rho}{\mathrm{D}t} + \rho T \frac{\mathrm{D}s}{\mathrm{D}t} \tag{2.10.11}$$

after assuming fast-melting and constant solid composition, as well as neglecting the heat of reaction. The sum $E + \frac{u_i^2}{2}$ is the total energy per unit mass. Integrating (2.10.10) over the core volume V and combining with (2.10.9) gives

$$\frac{\mathrm{d}}{\mathrm{d}t}\int_V \rho\left(E + \frac{u^2}{2}\right) = \int_V \rho \mathbf{u} \cdot \nabla\psi\,\mathrm{d}V + \oint_A \mathbf{u} \cdot \underline{\underline{\tau}} \cdot \mathbf{dA} - \oint_A \mathbf{q} \cdot \mathbf{dA}. \tag{2.10.12}$$

On the time-scales of interest, it is assumed that the rate of change in kinetic energy

is negligible in comparison with the leading order changes in gravitational and internal energies (Buffett *et al.*, 1996; Gubbins, 1977). Therefore (2.10.12) becomes

$$\frac{\mathrm{d}}{\mathrm{d}t}\int_V \rho E = \int_V \rho \mathbf{u}\cdot\nabla\psi \,\mathrm{d}V - \oint_A \mathbf{q}\cdot\mathbf{dA} - \int_V p\nabla\cdot\mathbf{u}\,\mathrm{d}V. \tag{2.10.13}$$

where the work done by deviatoric stress forces at the boundary vanish by assuming a stress-free boundary at the CMB.

By substituting the entropy differential (2.5.31) into (2.10.11), integral (2.10.13) becomes

$$-\int_V \alpha T\frac{\mathrm{D}p}{\mathrm{D}t}\,\mathrm{d}V + \int_V \rho c_p\frac{\mathrm{D}T}{\mathrm{D}t}\,\mathrm{d}V - \int_V \rho L\frac{\mathrm{D}\phi}{\mathrm{D}t}\,\mathrm{d}V = \int_V \rho\mathbf{u}\cdot\nabla\psi\,\mathrm{d}V - \oint_A \mathbf{q}\cdot\mathbf{dA}, \tag{2.10.14}$$

where the continuity equation (2.10.1) is used to replace $\frac{\mathrm{D}\rho}{\mathrm{D}t}$.

Recall that the entropy flux (2.8.10) is given by

$$\mathbf{q} = -L\mathbf{j} - k\nabla T \tag{2.10.15}$$

after neglecting the heat of reaction. Then the CMB heat flux is defined from (2.10.14) by

$$\begin{aligned} Q^c &\equiv \oint_A -k\nabla T\cdot\mathbf{dA} \\ &= \underbrace{\int_V \alpha T\frac{\mathrm{D}p}{\mathrm{D}t}\,\mathrm{d}V}_{Q_p,\text{ pressure freezing}} - \underbrace{\int_V \rho c_p\frac{\mathrm{D}T}{\mathrm{D}t}\,\mathrm{d}V}_{Q_s,\text{ secular cooling}} + \underbrace{\int_V L\left(\rho\frac{\mathrm{D}\phi}{\mathrm{D}t} + \nabla\cdot\mathbf{j}\right)\,\mathrm{d}V}_{Q_L,\text{ latent heat}} + \underbrace{\int_V \rho\mathbf{u}\cdot\nabla\psi\,\mathrm{d}V}_{Q_g,\text{ gravitational power}}. \end{aligned} \tag{2.10.16}$$

Assuming that pressure freezing and internal heating terms are negligible (see discus-

sion following equation (2.6.21)), the CMB heat flux reduces to

$$Q^c = -\int_V \rho c_p \frac{\mathrm{D}T}{\mathrm{D}t}\,\mathrm{d}V + \int_V Lm^s\,\mathrm{d}V + \int_V \rho\mathbf{u}\cdot\nabla\psi\,\mathrm{d}V, \tag{2.10.17}$$

where the solid mass equation (2.2.8) is used to relate the latent heat flux to the rate at which solid is created, m^s. Heat from secular cooling, Q_s, is generated as specific heat is lost over time as the core cools. Gravitational power, Q_g, is associated with the release of compositional energy as light elements separate from the solid phase when core material freezes. Latent heat, Q_L, is also released as result of phase change as solid phase is produced.

2.11 Summary

In this chapter, we presented the equations governing a two-phase, two component slurry system. Conservation laws for the total mass, light element, solid fraction, momentum and energy were expressed. We simplified the thermodynamics of these equations to produce a reduced slurry theory by applying two main approximations suggested by Loper & Roberts (1977, 1980, 1987); Roberts & Loper (1987), namely the fast-melting limit and constant solid composition. The fast-melting limit assumes that an infinitesimal volume of slurry exclusively contains either a solid or liquid phase, which implies that solid iron crystals are in phase equilibrium with the ambient liquid. We consider this assumption to be valid on relevant time-scales such as the speed of IC growth. By assuming a constant solid composition the solid created by freezing the alloy is composed only of pure iron while light element partitions entirely into the liquid phase during solidification. This assumption is supported by the *ab initio* partitioning studies of Alfè *et al.* (2002a), and allows us to disregard potential complications such

as particle history dependence.

The Gibbs free energy of the slurry system is considered in detail. Exact differentials of the specific density, entropy and chemical potential are derived from the Gibbs free energy, which is useful for developing the governing slurry equations. By assuming that the liquid and solid phases do not interact chemically the lever rule can be applied to derive the liquidus relation, which is essentially another form of the phase equilibrium condition. The liquidus describes the relationship between temperature, pressure and light element in the liquid phase everywhere in the slurry. This is very useful for reducing the thermodynamic complexity of the non-equilibrium theory.

Constitutive equations for the light element, solid and entropy fluxes are developed. In doing so, many of the thermodynamic quantities derived from the Gibbs free energy are used. The light element flux is composed of three parts: barodiffusion, a "Soret"-like effect, and the displacement of light element due to solid flux. These processes can explain the dynamics of how light element can pass through a stable F-layer. Solid flux is assumed to depend only on gradients of pressure, and we assume that solid particles fall under gravity against viscous drag according to Stokes' law. A model of mobility is proposed to help define the sedimentation coefficient, $b(\phi)$, however there is some uncertainty over estimating the number of particles per unit volume. In view of this, it is more insightful to consider solutions of the solid flux, $\mathbf{j}$, rather than solutions of ϕ of the slurry system. The entropy flux is derived and used to develop the temperature equation. By ignoring radiogenic heating, and neglecting the heat of reaction and pressure heating, we derive a temperature equation that is similar to the standard form used in thermal convection. The only difference is that the slurry releases latent heat as iron undergoes solidification, therefore an extra term proportional to the freezing rate, m^s, is needed to account for this.

Jump conditions on the mass, energy and solid mass at the slurry boundaries are

derived from first principles using the pillbox argument. We assume that the thermodynamic variables pressure, temperature and light element are continuous at the boundaries, whereas the solid fraction is not. We find that the heat flux across the slurry boundaries is continuous, after neglecting jumps in kinetic energy, viscous stress and the heat of reaction.

The slurry system is fundamentally distinct from the dynamics and thermodynamics of thermal or thermochemical convection. This is clear from the contribution of the changes in solid phase, $\mathrm{d}\phi$, to the Gibbs free energy. A significant difference of the slurry compared to standard convection models is the intrinsic relationship between the temperature, pressure and light element through the liquidus relation. For example in a system at constant pressure, warm fluid may not necessarily rise as it does in regular thermal convection since an increase in temperature reduces the concentration of light material in the liquid phase to maintain the liquidus. The increase in density from the reduction of light material can outweigh the decrease in density from warm temperatures. This mechanism could possibly help produce a stabilising, bottom-heavy slurry layer may explain the F-layer.

By examining the conservation of energy in the entire core, we derive a global energy balance for a core containing a slurry that is consistent with the assumptions made so far. This includes neglecting pressure freezing and the heat of reaction, as well as ignoring any internal heat generated from radiogenic sources. Heat is extracted from the core by the overlying mantle, and the simplified CMB heat flux is composed of three main parts: secular cooling, Q_s, latent heat, Q_L and the gravitational power, Q_g. We constrain results from the slurry system in subsequent chapters so that they are consistent with the CMB heat flows determined by thermal history models given in the literature.

Chapter 3

A steady-state box model

Contents

In this chapter we explore the properties of a basic slurry system by solving the governing equations (see Section 2.9) in a non-convective and steady reference state. We shall develop and examine a simple model of a slurry in a Cartesian box, with no x, y dependence, and z denoting the vertical distance in the layer. We ignore the effects of a magnetic field and rotation so that the dynamics of the slurry alone can be demonstrated clearly. The Boussinesq approximation is applied, where changes in density are assumed to be small except in the buoyancy force, since variations in density across an F-layer between 150 and 300 km thick are likely to be on the order of 0.1% according to PREM (Dziewonski & Anderson, 1981).

For conditions in the Earth's core a bottom-heavy F-layer with an unstable temperature gradient and a stable composition is inferred, as heat is transported radially outward from the inner core and a stable composition matches the seismology (see Section 1.1.2) . The position of the ICB changes over time due to inner core growth as iron particles accumulate at the base of the layer, so we seek a coordinate transform to a frame moving at the speed of ICB advance. This introduces an inherent time-dependence to the steady system, and so the model is technically in a quasi-steady state. The appropriate boundary conditions are determined, which constrains the steady state slurry equations. This includes fixing the light element concentration, temperature and solid flux at the top of the layer, and fixing the solid flux and the heat flow at the bottom of the layer. A schematic of the box model and the imposed boundary conditions is given in Figure 3.1.

A range of reference states are explored by changing three parameters. Due to the uncertainty in seismological estimates of the layer depth (see Section 1.2.1), we explore a range of layer thicknesses between 150 and 300 km. The heat flux out of the inner core is a geophysically uncertain constraint, with estimates varying between 0.3 TW and 1.6 TW depending on whether the inner core is assumed to be isothermally

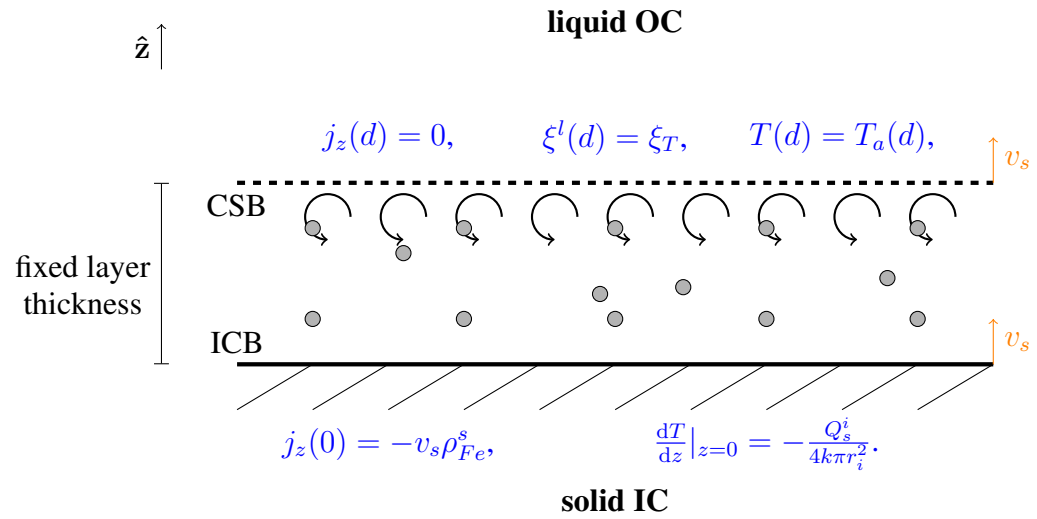

Figure 3.1: A schematic of the steady state box model. The steady state problem is solved subject to five boundary conditions.

or adiabatically stratified (Pozzo *et al.*, 2014). We explore its effect on the slurry layer by varying the heat flow through the system. Recent upward revisions to the thermal conductivity (see Section 1.1.3) significantly affects the amount of heat that is conducted along the adiabat, therefore we investigate its effect on the slurry layer.

3.1 Box model

The slurry layer is considered to be relatively thin compared to the rest of the core, so we seek a reference state in a Cartesian geometry. Seismic evidence indicates that F-layer stratification is dependent on depth, therefore we aim to formulate a one–dimensional model by assuming no x, y dependence $(\frac{\partial}{\partial x}, \frac{\partial}{\partial y} \to 0)$ and denote $\hat{\mathbf{z}}$ as the unit vector pointing away from the ICB. In a steady state we assume that the layer thickness, d, is fixed and cannot grow or shrink over time.

The position of the ICB advances upwards at the rate of inner core growth as solid particles accumulate at the base of the layer, assuming that there is no direct freezing at the interface itself and no compaction[1] of the solid occurs. In a steady state, the slurry is time-independent $(\frac{\partial}{\partial t} \to 0)$ and static $(\mathbf{u} = 0)$. The time dependence of the advancing ICB is removed by transforming to a frame of reference that moves with the ICB, in a similar manner to Gubbins *et al.* (2008). This transformation is given by

$$z = z' - v_s t \qquad t = t' \tag{3.1.1}$$

where z' and t' are the vertical and time coordinates in the rest frame, with z and t the corresponding coordinates in the moving frame in which the ICB is assumed to advance at speed $v_s > 0$. Buffett *et al.* (1996) estimate that the inner core growth rate, v_s, scales with $\sqrt{t}$, however for the purposes of developing a simple steady state model we shall assume that v_s is constant. As a consequence of transforming to a moving frame (3.1.1), the material derivative is given by

$$\frac{\mathrm{D}f}{\mathrm{D}t} \equiv -v_s \frac{\partial f}{\partial z}, \tag{3.1.2}$$

[1] Compaction is a common process in Earth sciences that occurs in lake sediments, hardening of snow, cumulate formation of magma chambers, etc. (Sumita *et al.*, 1996)

for an arbitrary scalar function, f.

There are a couple of simplifications that can be applied to the model equations at this point. Loper & Roberts (1980) assume that ξ^l cannot diffuse through solid material, which suggests that the diffusion coefficient D' can be linearly approximated as

$$D' = (1 - \phi)\bar{D} \simeq \bar{D} \tag{3.1.3}$$

where $\bar{D}$ is a modified diffusion coefficient independent of ϕ, and $\phi \ll 1$ is always assumed. The depression of the liquidus (2.9.1e) due to composition and the light element flux (2.9.1f), depends on the derivative of the chemical potential with respect to ξ^l. We use ideal solution theory (Gubbins *et al.*, 2004) to approximate the chemical potential. An ideal solution experiences no change in volume upon mixing, though the validity of an ideal solution under core pressure and temperature conditions remains to be checked experimentally by high pressure experiments. Gubbins *et al.* (2004) argue that the ideal solution approximation should be accurate for small concentrations of impurity, and the chemical potential is given by

$$\mu = \mu_0 + RT\frac{1000}{a_O}\log \xi^l, \tag{3.1.4}$$

where μ_0 is a constant reference potential, and $R \times 1000/a_O$ converts from molar to mass concentration, with R the gas constant and a_O the atomic weight of oxygen. The derivative of the chemical potential with respect to ξ^l is therefore

$$\xi^l \frac{\partial \mu}{\partial \xi^l} = RT\frac{1000}{a_O}. \tag{3.1.5}$$

The general equations for the light element (2.9.1b) and temperature (2.9.1d) are

$$\rho_0 \frac{\mathrm{D}\xi}{\mathrm{D}t} = -\nabla \cdot \left(-\frac{\rho_0 D' \Delta V^{s,l}_{Fe,O}}{\xi^l \left(\partial\mu/\partial\xi^l\right)} \nabla p + \frac{\rho_0 D' L}{T\xi^l \left(\partial\mu/\partial\xi^l\right)} \nabla T - \xi^l \mathbf{j} \right)$$
$$\rho_0 c_p \frac{\mathrm{D}T}{\mathrm{D}t} = \nabla \cdot (k\nabla T + L\mathbf{j}) + \rho_0 L \frac{\mathrm{D}\phi}{\mathrm{D}t}$$

where (2.9.1g) defines the solid flux

$$\mathbf{j} = b\left(\phi\right) \Delta V^{s,l}_{Fe,O} \nabla p$$

and the liquidus (2.9.1e)

$$\nabla T = \frac{T\Delta V^{s,l}_{Fe}}{L} \nabla p - \frac{T\xi^l \left(\partial\mu/\partial\xi^l\right)}{L} \nabla \xi^l$$

closes the equations. For a steady slurry system with an advancing ICB, the light element and temperature equations become

$$\xi^l \frac{\mathrm{d}j_z}{\mathrm{d}z} = g\rho^l_{Fe} \frac{\mathrm{d}}{\mathrm{d}z} \left(\frac{\rho^l_{Fe} \bar{D} \Delta V^{s,l}_{Fe,O}}{RT\frac{1000}{a_O}} \right) - \left(v_s \rho^l_{Fe} + j_z\right) \frac{\mathrm{d}\xi^l}{\mathrm{d}z}, \tag{3.1.6}$$
$$-k\frac{\mathrm{d}^2 T}{\mathrm{d}z^2} = v_s \rho^l_{Fe} c_p \frac{\mathrm{d}T}{\mathrm{d}z} + L\frac{\mathrm{d}j_z}{\mathrm{d}z}, \tag{3.1.7}$$

using (3.1.2) and (3.1.5), where the reference density, ρ_0, is assumed to be equal to the density of liquid iron, ρ^l_{Fe}. Terms involving $d\phi/dz$ are ignored since results suggest the solid fraction must be on the order of $|\phi| \sim 10^{-3}$ to be comparable with the other terms in (3.1.7). The "Soret"-like term in the light element flux is also neglected, so that the effect of barodiffusion alone can be elucidated for the sake of simplicity.

3.1.1 Boundary conditions

The steady state equations (3.1.6), (3.1.7) and liquidus (2.9.1e) form a fourth order system. This is solved subject to five boundary conditions, in which the extra boundary condition determines a free parameter introduced later in Section 3.1.2. In Section 2.8 we derived the jump conditions at the slurry boundaries. We assumed the continuity of light element in the liquid phase (2.8.3)

$$\langle \xi^l \rangle = 0,$$

at the ICB and CSB. Continuity of ξ^l at the CSB at the top of the layer yields the boundary condition

$$\xi^l(d) = \xi_T, \tag{3.1.8}$$

where ξ_T is the concentration of light element in the bulk of the liquid core, and is presumed to be 8 mol.% oxygen (Alfè *et al.*, 2002b). The temperature is assumed to be continuous across the boundaries (2.8.2), so that

$$\langle T \rangle = 0,$$

therefore the slurry temperature at the CSB should coincide with the adiabatic temperature of the liquid outer core

$$T(d) = T_a(d), \tag{3.1.9}$$

where T_a is the adiabatic temperature. The adiabat is calculated by (Gubbins *et al.*, 2003)

$$T_a(z) = T_i \exp\left(- \int_0^{r_i+z} \frac{g\gamma}{\varphi} \, \mathrm{d}z \right), \tag{3.1.10}$$

where T_i is the ICB temperature, r_i is the ICB radius and

$$\varphi \equiv \frac{K_s}{\rho} = v_p^2 - \frac{4}{3}v_s^2 \tag{3.1.11}$$

is the seismic parameter, with $K_s \equiv -V\left(\frac{\partial p}{\partial V}\right)_s$ the adiabatic bulk modulus, v_p the P wave speed and v_s the S wave speed. Shear waves cannot propagate through liquid so the seismic parameter reduces to $\varphi = v_p^2$ in the liquid outer core, and the P wave velocity is taken from PREM (Dziewonski & Anderson, 1981).

Continuity of the heat flux at the boundaries (2.8.20) is given by

$$\mathbf{n} \cdot \langle k \nabla T \rangle = 0.$$

At the ICB this heat flux condition becomes

$$\frac{\mathrm{d}T^{sl}}{\mathrm{d}z} = -\frac{Q_s^i}{4k\pi r_i^2}, \tag{3.1.12}$$

where thermal conductivity, k, is assumed to be continuous and Q_s^i is the heat flux from the secular cooling of the IC. Note that the latent heat released in the slurry is separated from the heat flux out of the inner core, since we assume that the latent heat released by inner core growth is due to the accumulation of solid particles from the slurry settling onto the ICB.

The jump condition on the solid mass at the slurry boundaries (2.8.8) is

$$\langle \rho\phi \left(\mathbf{u} - \mathbf{U}\right) \rangle \cdot \mathbf{n} + \langle \mathbf{j} \rangle \cdot \mathbf{n} = 0.$$

At the ICB this condition becomes

$$\rho^{sl}\phi^{sl}(u^{sl} - U^{sl}) + j_z^{sl} - \rho^s\phi^s(u^s - U^s) - j_z^s = 0. \tag{3.1.13}$$

We have assumed a fixed layer thickness so that the boundary velocities are the same, so $U^{sl} = U^s = v_s$, the speed of the moving frame. In the limit $\phi^{sl} \ll 1$, the first term of (3.1.13) becomes negligible. Assuming that the solid inner core is static and not convecting, then $u^s = 0$ and $j_z^s = 0$. The density of the solid, ρ^s, is assumed to be equal to the density of solid iron, ρ^s_{Fe}, and we suppose $\phi^s = 1$ in the solid inner core. Therefore the boundary condition on the solid flux at the ICB is

$$j_z^{sl} = -\rho^s_{Fe} v_s. \tag{3.1.14}$$

The sign of the solid flux is negative down towards the ICB since iron particles sediment under gravity. Assuming linear growth of the inner core, then the growth speed, $v_s > 0$, is estimated by

$$v_s = \frac{r_i}{\tau_i} \tag{3.1.15}$$

where r_i is the present-day inner core radius and τ_i is the age of the inner core. Speeds of 1.2 and $2.4\,\mathrm{mmyr}^{-1}$ correspond with inner core ages of 0.5 and $1\,\mathrm{Ga}$ respectively, and relate to the high and low values of thermal conductivity through the core energy budget (see Figure 1.4).

At the CSB, condition (2.8.8) gives

$$\begin{aligned} &\rho^{sl}\phi^{sl}(u^{sl} - U^{sl}) + j_z^{sl} - \rho^l\phi^l(u^l - U^l) - j_z^l = 0 \\ &\Rightarrow j_z^{sl} = 0, \end{aligned} \tag{3.1.16}$$

where $j_z^l = \phi^l = 0$ in the liquid since no solid exists on the liquid side of the CSB, and $\phi^{sl} \ll 1$. Applying two boundary conditions on j_z over–constrains the steady state problem, therefore a free parameter is introduced in Section 3.1.2 to ensure (3.1.16) is satisfied at the CSB.

3.1.2 Turbulent mixing layer

If there is no diffusion in the light element flux so that $\bar{D} = 0$, then the first term on the RHS of (3.1.6) vanishes. This gives

$$\frac{\mathrm{d}}{\mathrm{d}z}\left(v_s \rho_{Fe}^l \xi^l + \xi^l j_z\right) = 0,$$

which can be simply integrated to give

$$v_s \rho_{Fe}^l \xi^l + \xi^l j_z = C, \tag{3.1.17}$$

where C is a constant of integration. At the CSB, we apply the boundary conditions (3.1.8) and (3.1.16), therefore constant C is given by

$$C = v_s \rho_{Fe}^l \xi_T$$

and (3.1.17) becomes

$$v_s \rho_{Fe}^l (\xi_T - \xi^l) = \xi^l j_z. \tag{3.1.18}$$

For a stable layer, we require $\xi^l < \xi_T$ and the solid flux is always in the negative direction for solid particles to snow towards the ICB. These two requirements are not consistent with condition (3.1.18) and contradicts the assumption that $\bar{D} = 0$, hence we require $\bar{D} \neq 0$ to attain a stable layer.

We envisage a thin turbulent mixing sub-layer at the top of the slurry generated by the difference in the slurry and the liquid outer core velocities. We suppose that in the mixing sub-layer, diffusion is enhanced by eddies that promote the transport of light element out of the slurry layer into the rest of the outer core. This mechanism is incorporated into the pre-existing light element barodiffusion term in (3.1.6), as this process also transports light element out of the layer, albeit along a pressure gradient. Enhancement is controlled by modifying the self-diffusion coefficient, $\bar{D}$. A functional form of $\bar{D}$ is assumed by the exponential function

$$\bar{D} = D_O \exp\left(\frac{Fz}{d}\right), \tag{3.1.19}$$

where D_O is the self-diffusion coefficient of oxygen and F is a dimensionless free parameter to be determined by forcing the solid flux to vanish at the CSB as required by (3.1.16). Note that by adopting (3.1.19) the product rule applies to the z-derivative of the barodiffusion term in (3.1.6) so that the light element flux becomes

$$\begin{aligned} i_z &= -g\rho^l_{Fe}\frac{\mathrm{d}}{\mathrm{d}z}\left(\frac{\rho^l_{Fe}\bar{D}\Delta V^{s,l}_{Fe,O}a_O}{1000RT}\right) \\ &= -\left(\frac{g{\rho^l_{Fe}}^2\Delta V^{s,l}_{Fe,O}a_O}{1000R}\right)\frac{\mathrm{d}}{\mathrm{d}z}\left(\frac{\bar{D}}{T}\right) - \xi^l j_z \\ &= -\frac{g{\rho^l_{Fe}}^2\Delta V^{s,l}_{Fe,O}a_O}{1000R}\left(\frac{F\bar{D}}{Td} - \frac{\bar{D}}{T^2}\frac{\partial T}{\partial z}\right) - \xi^l j_z. \end{aligned} \tag{3.1.20}$$

3.2 Parameter estimates

To explore the slurry system we shall vary the most uncertain parameters, such as the layer thickness, ICB heat flux and thermal conductivity, while assuming that other parameters remain fixed. For reference, a list of all parameter estimates is given in

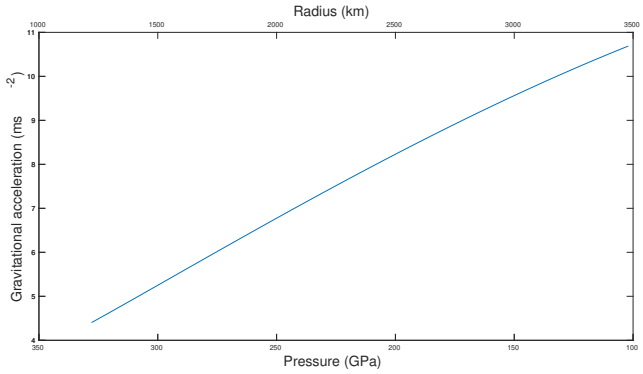

Figure 3.2: Gravitational acceleration in the core according to PREM (Dziewonski & Anderson, 1981).

Table (3.1). Given that the F-layer is thin compared to the rest of the outer core, some parameter values are assumed to be constant since they are not expected to vary much across such a thin layer. This includes physical and material properties such as the gravitational acceleration, g, specific heat capacity, c_p, thermal and compositional expansion coefficients, α and α_ξ respectively, latent heat, L, self-diffusion coefficient of oxygen, D_O, specific densities ρ_O^l and ρ_{Fe}^l, and thermal conductivity, k.

From Figure 3.2 it can be seen that the gravitational acceleration, g, varies significantly with depth inside the core. Its value is $4.40\ \mathrm{ms}^{-2}$ at the ICB and $5.32\ \mathrm{ms}^{-2}$ at the top of an F-layer $300\ \mathrm{km}$ thick. This difference is roughly 20%, which is not insignificant, however as a sensible first step we take g as constant in the slurry for now. The thermal expansion coefficient, α, and the specific heat capacity, c_p, are closely linked through the Grüneisen parameter, γ, by

$$\gamma = \frac{\alpha K_s}{\rho c_p}, \tag{3.2.1}$$

where $K_s \equiv -V\left(\frac{\partial p}{\partial V}\right)_s$ is the adiabatic bulk modulus (Stacey & Davis, 2008). Calculations from first principles show that the Grüneisen parameter near the ICB varies a small amount from 1.51 to 1.52 as pressure increases from 280 to 340 GPa (Ichikawa

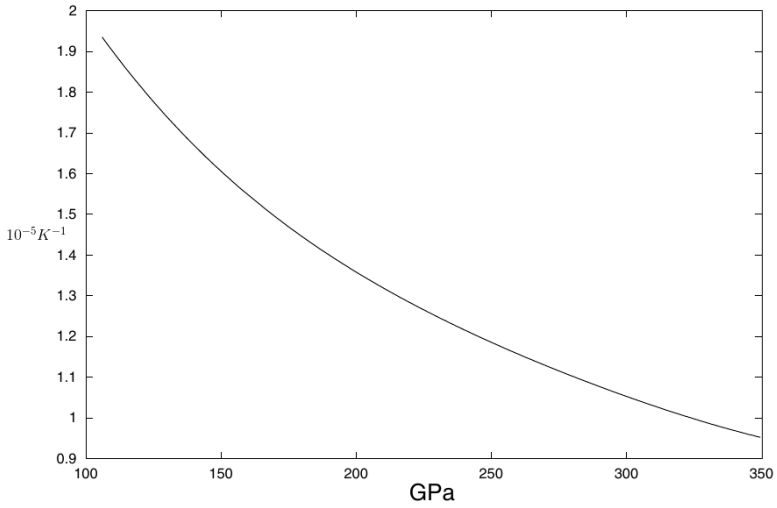

Figure 3.3: Thermal expansion coefficient, α, with units of $10^{-5}\mathrm{K}^{-1}$ in the core. Figure modified from Gubbins *et al.* (2003).

et al., 2014). The relevant core pressures for an F-layer up to 300 km thick is between 310 and 330 GPa, therefore we take γ as constant. Both the density, ρ, and the adiabatic bulk modulus, K_s, are known from PREM (Dziewonski & Romanowicz, 2015), whereas thermal expansion, α, and the specific heat capacity, c_p, are determined from experiments and *ab initio* calculations. Figure 3.3 shows the variation of the thermal expansion coefficient in the core determined from first principles (Gubbins *et al.*, 2003). At core pressures relevant to the F-layer, we take α as constant with the value 1.0×10^{-5} K^{-1} and the corresponding specific heat capacity is given by

$$c_p = \frac{\alpha K_s}{\gamma \rho} \simeq \frac{(1.0 \times 10^{-5})(1.3 \times 10^{12})}{(1.5)(1.2 \times 10^{4})} \simeq 715 \text{ Jkg}^{-1}. \tag{3.2.2}$$

The compositional expansion coefficient, α_ξ, is calculated from the partial volume data provided by *ab initio* calculations. From first principles, Gubbins *et al.* (2004) find that compositional expansion coefficient is equal to 1.1 for oxygen.

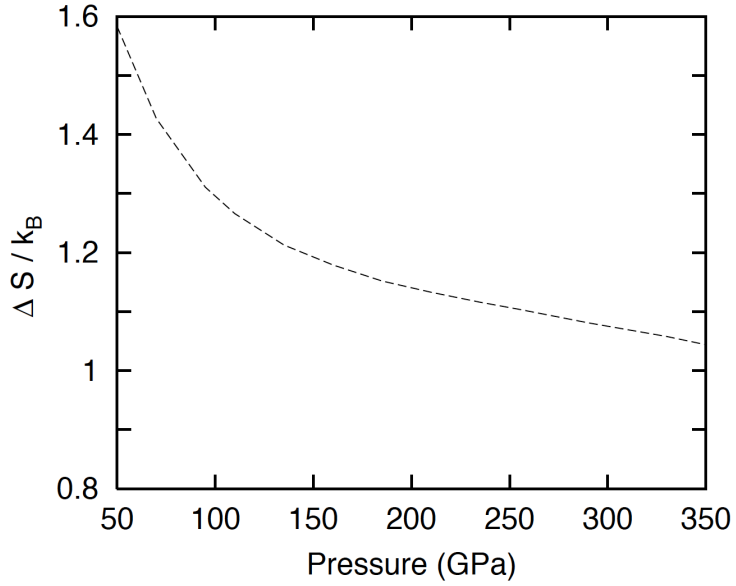

Figure 3.4: Entropy of melting per atom from *ab initio* calculations. Figure modified from Alfè *et al.* (2002c).

Recall the definition of the latent heat in the slurry (2.5.29)

$$L = T\Delta s + T\xi^l \frac{\partial \mu}{\partial T}, \tag{3.2.3}$$

where $\Delta s = s^l - s^s$ is the entropy difference between solid and liquid. Figure 3.4 presents data from *ab initio* calculations (Alfè *et al.*, 2002c) that shows the entropy of melting varies little at pressures between 310 and 330 GPa which correspond with the F-layer. From ideal solution theory (3.1.4), the second term of (3.2.3) becomes

$$T\xi^l \frac{\partial \mu}{\partial T} = T\xi^l \frac{1000R}{a_O} \log \xi^l. \tag{3.2.4}$$

We assume that ξ^l and T do not vary greatly in the layer, which is likely to be smaller than the change in gravity across the layer. Given that model uncertainties in the parameter estimates cannot be avoided, we take $L = 0.75 \times 10^6$ Jkg^{-1} (Gubbins *et al.*, 2003) as constant in the slurry layer for the sake of simplicity.

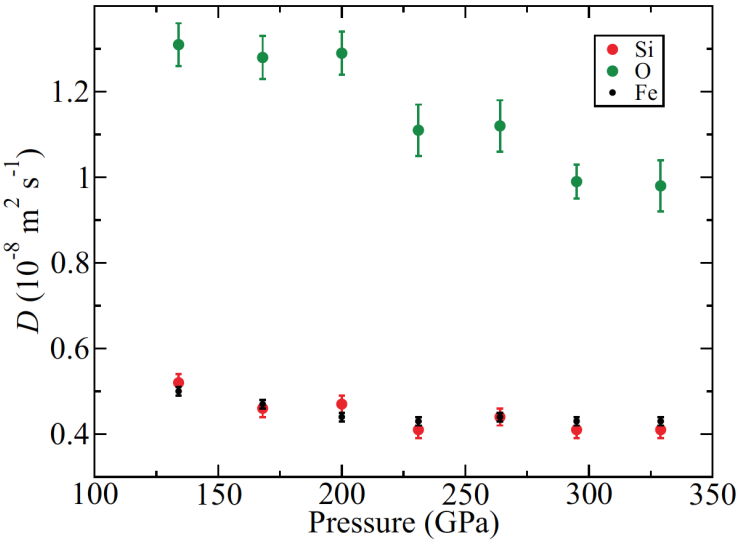

Figure 3.5: Self-diffusion coefficients of iron, silicon and oxygen atoms as a function of pressure for an $Fe_{0.82}Si_{0.10}O_{0.08}$ mixture. Figure from Pozzo *et al.* (2013).

The self-diffusion coefficient of oxygen, D_O, is calculated from first principles (Pozzo *et al.*, 2013). Figure 3.5 shows that its value does not vary greatly with pressure close to the ICB. Therefore we take D_O constant at $1 \times 10^{-8}\ \mathrm{m^2 s^{-1}}$.

From seismology, the specific density on the solid side of the ICB is estimated as $\rho^s_{Fe} = 12.76 \times 10^3\ \mathrm{kg\,m^{-3}}$ (Dziewonski & Anderson, 1981). Ideal solution theory is used to estimate the specific densities of the other slurry components. Specific densities are taken from Gubbins *et al.* (2004) and are given by $\rho_O = 5.56 \times 10^2\ \mathrm{kg\,m^{-3}}$, and $\rho^l_{Fe} \equiv \rho^s_{Fe} - \Delta\rho_{\mathrm{melting}} = 12.52 \times 10^3\ \mathrm{kg\,m^{-3}}$ where the density drop upon melting is $\Delta\rho_{\mathrm{melting}} = 0.24 \times 10^3\ \mathrm{kg\,m^{-3}}$, calculated from first principles (Alfè *et al.*, 2002a). This assumes that the core material is composed of an Fe-(Si,S)-O alloy, with 84% iron, 8% silicon/sulphur and 8% oxygen, where oxygen partitions entirely into the liquid when the alloy solidifies (Alfè *et al.*, 2002b).

As discussed in Section 1.1.2 thermal conductivity at core conditions is difficult to study in high pressure experiments, and its value significantly impacts thermal history models and estimates of the inner core age. Lower thermal conductivities produce a

nominal inner core age of a billion years (Davies *et al.*, 2015), since heat is removed more slowly from the core as less heat is conducted along the adiabat. However recent higher conductivity estimates mean that heat is evacuated more quickly from the core, therefore the inner core is a much younger feature of the Earth, with a predicted inner core age of 500 million years (Gomi *et al.*, 2013; Konôpková *et al.*, 2016; Ohta *et al.*, 2016).

Table 3.1 summarises the parameter estimates used in the steady state box model.

Symbol	Definition	Value	Units	Source
r_i	ICB radius	1.22×10^6	m	PREM (Dziewonski & Anderson, 1981)
r_o	CMB radius	3.48×10^6	m	PREM
g	Gravitational acceleration at $r = r_i$	4.40×10^4	ms^{-1}	PREM
$g\rho^l_{Fe}$	Hydrostatic pressure gradient at $r = r_i$	5.51×10^4	$\mathrm{Pa\,m}^{-1}$	PREM
ρ^s_{Fe}	Specific density of solid	12.76×10^3	$\mathrm{kg\,m}^{-3}$	PREM
$\rho^l_{Fe,O}$	Specific density of liquid iron and oxygen at $r = r_i$	12.17×10^3	$\mathrm{kg\ m}^{-3}$	PREM
ξ_T	Oxygen concentration in the bulk of the liquid core	0.0252 (8)	Mass fraction (mol.%)	Alfè *et al.* (2002b)
T_i	ICB temperature	5,500	K	Alfè *et al.* (2007)
T_c	CMB temperature	4,290	K	Davies *et al.* (2015)
c_p	Specific heat capacity	715	$\mathrm{J\,kg}^{-1}\,\mathrm{K}^{-1}$	Gubbins *et al.* (2003)
α	Thermal expansion coefficient	1×10^{-5}	K^{-1}	Gubbins *et al.* (2003)
α_ξ	Compositional expansion coefficient of oxygen	1.1		Gubbins *et al.* (2004)

L	Latent heat of fusion	0.75×10^6	$\mathrm{J\,kg^{-1}}$	Gubbins *et al.* (2003)
D_O	Self–diffusion coefficient of oxygen	1×10^{-8}	$\mathrm{m^2 s^{-1}}$	Pozzo *et al.* (2013)
$\Delta\rho_{\mathrm{melting}}$	Density drop upon melting	0.24×10^3	$\mathrm{kg\,m^{-3}}$	Alfè *et al.* (2002a)
ρ_O	Specific density of light element	5.56×10^3	$\mathrm{kg\,m^{-3}}$	Gubbins *et al.* (2004)
ρ^l_{Fe}	Specific density of liquid iron, reference density	12.52×10^3	$\mathrm{kg\,m^{-3}}$	Gubbins *et al.* (2004)
d	Layer thickness	$150 - 300$	km	Section 1.2.1
Q^i_s	Secular cooling of the inner core	$0.8 - 1.6$	TW	Pozzo *et al.* (2014)
τ_i	Inner core age	$0.5 - 1$	Ga	Gomi *et al.* (2013)
k	Thermal conductivity	$50 - 107$	$\mathrm{Wm^{-1}K^{-1}}$	Davies *et al.* (2015)
Q^c	CMB heat flow	$5 - 17$	TW	Lay *et al.* (2008), Nimmo (2015a)
$\frac{\mathrm{d}T_c}{\mathrm{d}t}$	Core cooling rate	-100	$\mathrm{KGa^{-1}}$	Nimmo (2015a)

Table 3.1: Parameter estimates used in the steady state box model. The first group are well-known and derived from seismology; the second group relies on *ab initio* calculations; the third group depend on ideal solution theory; the fourth group are parameters to be investigated in the slurry model.

3.3 Geophysical constraints

The steady state model should satisfy several geophysical constraints. The density jump across the slurry layer should be consistent with seismic observations (see Section 1.1.3). The discrepancy between the normal and body wave estimates, $\Delta\rho_{\text{mod}} - \Delta\rho_{\text{bod}}$, constrains the anomalous stabilising density contrast across the F-layer caused by stable stratification. Hence solutions obtained from the slurry model should satisfy a maximum density jump of $\max(\Delta\rho_{\text{mod}} - \Delta\rho_{\text{bod}}) = 1,100 - 280 = 720\,\text{kg}\,\text{m}^{-3}$, and a minimum density jump is unspecified since $\min(\Delta\rho_{\text{mod}} - \Delta\rho_{\text{bod}}) < 0$ because the observations are not in agreement with each other. The variance in the range of permissible density jumps is attributed to the limitations of different sampling techniques employed in each seismic study (Deuss, 2014).

Total density, ρ, is given by the addition of the hydrostatic part, ρ_H, together with density fluctuations, ρ', within the slurry given by (2.9.1j). The hydrostatic contribution is derived from the equation of hydrostatic equilibrium (2.2.13)

$$\frac{\mathrm{d}p_H}{\mathrm{d}z} = -g\rho_H. \tag{3.3.1}$$

The thermodynamic definition of the isothermal bulk modulus is

$$K_T \equiv \rho\frac{\mathrm{d}p}{\mathrm{d}\rho}, \tag{3.3.2}$$

therefore the variation of the hydrostatic density with respect to z is

$$\frac{\partial\rho_H}{\partial z} = \frac{\partial\rho}{\partial p_H}\frac{\partial p_H}{\partial z} = -\frac{g\rho_H^2}{K_T}. \tag{3.3.3}$$

Integrating (3.3.3) gives

$$\int \frac{1}{\rho_H^2}\,\mathrm{d}\rho_H = \int -\frac{g}{K_T}\,\mathrm{d}z \Rightarrow -\frac{1}{\rho_H} = -\frac{gz}{K_T} + C, \tag{3.3.4}$$

where C is a constant of integration. We impose $\rho(d) = \rho_{\mathrm{PREM}}$, in which ρ_{PREM} is the PREM value of the density taken from Dziewonski & Anderson (1981) at the top of the slurry layer. Hence (3.3.4) becomes

$$\rho_H = \left(\frac{g}{K_T}(z-d) + \frac{1}{\rho_{\mathrm{PREM}}}\right)^{-1}. \tag{3.3.5}$$

Note that for a bottom-heavy layer the calculated density jump, $\Delta\rho$, is negative, so its magnitude is presented in the results.

Present day estimates of the maximum CMB heat flow are believed to be $12\pm5\,\mathrm{TW}$ (see Table 3.1), therefore acceptable steady state solutions should satisfy

$$5\,\mathrm{TW} \leq Q^c = Q_s + Q_l + Q_g \leq 17\,\mathrm{TW}. \tag{3.3.6}$$

The global energy balance of the core is derived in Chapter 2 and is given by (2.10.17)

$$Q^c = -\int_V \rho c_p \frac{\mathrm{D}T}{\mathrm{D}t}\,\mathrm{d}V + \int_V Lm^s\,\mathrm{d}V + \int_V \rho\mathbf{u}\cdot\nabla\psi\,\mathrm{d}V \tag{3.3.7}$$

The total core volume, V, can be split into three parts: $V = V^l + V^{sl} + V^s$, where V^l is the liquid outer core volume, V^{sl} is the slurry volume and V^s is the solid inner core volume. The secular cooling can be split into $Q_s = Q_s^l + Q_s^{sl} + Q_s^i$, where

$$Q_s^l = -\int_V \rho c_p \frac{\mathrm{D}T_a}{\mathrm{D}t}\,\mathrm{d}V^l. \tag{3.3.8}$$

is the secular cooling in the liquid outer core. We have assumed that the temperature in

the liquid outer core is adiabatic, T_a, calculated using (3.1.10). Gubbins *et al.* (2003) show that the change in adiabatic temperature is related to the core cooling rate, $\frac{\mathrm{d}T_c}{\mathrm{d}t}$ by

$$\frac{1}{T_a}\frac{\mathrm{D}T_a}{\mathrm{D}t} = \frac{1}{T_c}\frac{\mathrm{d}T_c}{\mathrm{d}t}, \tag{3.3.9}$$

where T_c is the CMB temperature. We use the estimate of $T_c = 4,290$ K as reported by Davies *et al.* (2015), which is derived from *ab initio* calculations and high pressure experiments, and a cooling rate of $\frac{\mathrm{d}T_c}{\mathrm{d}t} = -100\ \mathrm{KGa}^{-1}$, which is a rough value taken from Nimmo (2015a) derived from thermal history models in the literature. Hence (3.3.8) becomes

$$Q_s^l = -\frac{4\pi c_p}{T_c}\frac{\mathrm{d}T_c}{\mathrm{d}t}\int_{r_{sl}}^{r_o} \rho T_a r^2\,\mathrm{d}z, \tag{3.3.10}$$

where $r = r_i + z$ and $r_{sl} = r_i + d$ denotes the CSB radius. Note that the global energy balance is formulated in the rest frame, so technically the coordinates need to be denoted by primes (see equation (3.1.1)), but we drop them here for the sake of convenience. In the slurry volume we have assumed that the flow is static, therefore

$$\begin{aligned} Q_s^{sl} &= -\int_{V^{sl}} \rho c_p \frac{\partial T}{\partial t}\,\mathrm{d}V^{sl} \\ &= -\int_{V^{sl}} \rho c_p \frac{\partial T}{\partial z}\frac{\partial z}{\partial t}\,\mathrm{d}V^{sl} \\ &= -4\pi\int_0^d \rho c_p v_s \frac{\partial T}{\partial z}\,(r_i + z)^2\,\mathrm{d}z, \end{aligned}$$

where $v_s \equiv \frac{\partial z}{\partial t}$ is the speed of IC growth.

On time-scales longer than core convection but shorter than core evolution, we assume that all of the solid formed in the slurry volume has fallen towards the ICB and

accumulated to grow the IC. Therefore

$$\int_{V^{sl}} m^s \, \mathrm{d}V^{sl} = \frac{\mathrm{d}}{\mathrm{d}t} \int_{V^s} \rho^s_{Fe} \phi^s \, \mathrm{d}V^s = \oint_{A^s} \rho^s_{Fe} \mathbf{U^s} \cdot \mathbf{dA^s}, \tag{3.3.11}$$

where the RHS describes the rate of change of the total mass of the IC volume. Latent heat is released when solid particles freeze from the alloy, therefore the latent heat flux is

$$Q_L = \int_{V^{sl}} L m^s \mathrm{d}V^{sl} = \oint_{A^s} \rho^s_{Fe} L \mathbf{U^s} \cdot \mathbf{dA^s} = - \oint_{A^s} L j_z \, \mathrm{d}A^s, \tag{3.3.12}$$

where boundary condition (3.1.14) is used to relate the ICB speed to the solid flux by $\rho^s_{Fe}\mathbf{U^s} \cdot \hat{\mathbf{n}} = \rho^s_{Fe} v_s = -j_z$. The latent heat flux, Q_L, is known *a priori* since this is controlled by the input parameter, v_s, the ICB speed. We assume that iron particles fall under gravity and accumulate at the ICB to grow the inner core, therefore latent heat is not released directly at the ICB, though its calculation using time-scale arguments is evaluated at the IC surface using (3.3.12). Boundary condition (3.1.12) contains the specific heat extracted from the inner core and does not include the latent heat release in the slurry.

The total gravitational power in the core can be manipulated to give

$$\begin{aligned} Q_g &= \int_V \rho \mathbf{u} \cdot \nabla \psi \, \mathrm{d}V \\ &= \int_V \nabla \cdot (\rho \psi \mathbf{u}) \, \mathrm{d}V - \int_V \psi \nabla \cdot (\rho \mathbf{u}) \, \mathrm{d}V. \end{aligned} \tag{3.3.13}$$

Assuming that there is no normal flow at the CMB boundary, then $\mathbf{u} \cdot \hat{\mathbf{n}} = 0$ and (3.3.13) together with the continuity equation (2.10.1) becomes

$$Q_g = \int_V \psi \frac{\partial \rho}{\partial t} \, \mathrm{d}V. \tag{3.3.14}$$

Gravitational energy is released when light element from the slurry moves into the convecting liquid outer core. The available energy (negative) helps to power the dynamo, and is converted into heat (positive) that enters into the global heat balance, Q^c. Gubbins *et al.* (2004) notes that the density change caused by the separation of light material is given by

$$\left(\frac{\partial \rho}{\partial t}\right)_{p,T,\phi} = \left(\frac{\partial \rho}{\partial \xi}\right)_{p,T,\phi} \frac{\partial \xi}{\partial t} = -\rho \alpha_\xi \frac{\partial \xi}{\partial t}, \tag{3.3.15}$$

where the thermodynamic definition of the compositional expansion coefficient, $\alpha_\xi \equiv -\frac{1}{\rho}\left(\frac{\partial \rho}{\partial \xi}\right)_{p,T,\phi}$ is used. Substituting (3.3.15) into (3.3.14) gives

$$\begin{aligned} Q_g &= -\int_V \rho \psi \alpha_\xi \frac{\partial \xi}{\partial t}\, \mathrm{d}V \\ &= -\int_V \rho \psi \alpha_\xi \frac{\partial \xi}{\partial z}\frac{\partial z}{\partial t}\, \mathrm{d}V \\ &= -\int_V \rho \psi \alpha_\xi v_s \frac{\partial \xi}{\partial z}\, \mathrm{d}V. \end{aligned} \tag{3.3.16}$$

We assume that vigorous convection in the liquid outer core quickly homogenises the distribution of light elements, and no light elements exist in the solid inner core, therefore $\frac{\partial \xi}{\partial z}$ is zero in V^l and V^s. Hence (3.3.16) becomes

$$\begin{aligned} Q_g &= -\int_{V^{sl}} \rho \psi \alpha_\xi v_s \frac{\partial \xi}{\partial z}\, \mathrm{d}V^{sl} \\ &= 4\pi \int_0^d \rho g \alpha_\xi v_s \frac{\partial \xi}{\partial z} (r_i + z)^3 \, \mathrm{d}z, \end{aligned} \tag{3.3.17}$$

where we have assumed gravity is constant in the layer so that $\psi = \int g \, \mathrm{d}r = gr = g(r_i + z)$.

In conventional thermal history models the CMB heat flux is directly proportional to the core cooling rate $\frac{\mathrm{d}T_c}{\mathrm{d}t}$ (Gubbins *et al.*, 2003). When a slurry is present this is not

the case, because the specific heat in the slurry layer is conducted along the liquidus temperature gradient rather than the adiabat, for example.

3.4 Boundary value problem

In this section we formulate a boundary value problem to solve the steady state system (see equations 2.9.1e, 2.9.1g, 3.1.6, 3.1.7, and 3.1.20)

$$\frac{\mathrm{d}T}{\mathrm{d}z} = -\frac{T\Delta V_{Fe}^{s,l}}{L} g\rho_{Fe}^{l} - \frac{RT^2 1000}{a_O L}\frac{\mathrm{d}\xi^l}{\mathrm{d}z}, \tag{3.4.1a}$$

$$\xi^l \frac{\mathrm{d}j_z}{\mathrm{d}z} = g\rho_{Fe}^{l}\frac{\rho_{Fe}^{l}\Delta V_{Fe,O}^{s,l} a_O}{1000R}\left(\frac{F\bar{D}}{Td} - \frac{\bar{D}}{T^2}\frac{\partial T}{\partial z}\right) - \left(v_s\rho_{Fe}^{l} + j_z\right)\frac{\mathrm{d}\xi^l}{\mathrm{d}z}, \tag{3.4.1b}$$

$$-k\frac{\mathrm{d}^2T}{\mathrm{d}z^2} = v_s\rho_{Fe}^{l}c_p\frac{\mathrm{d}T}{\mathrm{d}z} + L\frac{\mathrm{d}j_z}{\mathrm{d}z}, \tag{3.4.1c}$$

$$j_z = -b(\phi)\Delta V_{Fe,O}^{s,l} g\rho_{Fe}^{l}, \tag{3.4.1d}$$

subject to the boundary conditions (see equations 3.1.8, 3.1.9, 3.1.12, 3.1.14 and 3.1.16)

$$\xi^l(d) = \xi_T, \tag{3.4.2a}$$

$$T(d) = T_a(d) \tag{3.4.2b}$$

$$\left.\frac{\mathrm{d}T}{\mathrm{d}z}\right|_{z=0} = -\frac{Q_s^i}{4k\pi r_i^2}, \tag{3.4.2c}$$

$$j_z(0) = -\rho_{Fe}^{s} v_s, \tag{3.4.2d}$$

$$j_z(d) = 0. \tag{3.4.2e}$$

Equations (3.4.1a)–(3.4.1d) form a fourth order system, but there are five boundary conditions (3.4.2a)–(3.4.2e) which over-constrains the problem. A free parameter, F, is introduced through a turbulent mixing layer at the top of the slurry (see Section

3.1.2), which is controlled by the self-diffusion coefficient (3.1.19)

$$\bar{D} = D_O \exp\left(\frac{Fz}{d}\right).$$

The unknown parameter F is an eigenvalue to be determined that satisfies (3.4.2e).

The boundary value problem is solved using MATLAB function `bvp4c`, which implements a three-stage Lobatto IIIa formula using finite differences (Shampine *et al.*, 2000). Equations (3.4.1a)–(3.4.1d) are converted to an equivalent system of first order ordinary differential equations for the solver. We substitute the liquidus (3.4.1a) into the temperature equation (3.4.1c) to give

$$\frac{\mathrm{d}^2\xi^l}{\mathrm{d}z^2} = \left[\frac{v_s\rho^l_{Fe}c_p a_O}{1000kRT^2} - \frac{\Delta V^{s,l}_{Fe} g \rho^l_{Fe} a_O}{1000RT^2} - \frac{2}{T}\frac{\mathrm{d}\xi^l}{\mathrm{d}z}\right]\frac{\mathrm{d}T}{\mathrm{d}z} + \frac{a_O L}{1000kRT^2}\frac{\mathrm{d}j_z}{\mathrm{d}z}. \tag{3.4.3}$$

We label the variables

$$y_1 = \xi^l, \tag{3.4.4a}$$

$$y_2 = T, \tag{3.4.4b}$$

$$y_3 = j_z, \tag{3.4.4c}$$

so that (3.4.1a), (3.4.1b) and (3.4.3) become

$$\frac{\mathrm{d}y_1}{\mathrm{d}z} = y_4, \tag{3.4.5a}$$

$$\frac{\mathrm{d}y_2}{\mathrm{d}z} = -K_1 y_2 - K_2 y_2^2 y_4, \tag{3.4.5b}$$

$$\frac{\mathrm{d}y_3}{\mathrm{d}z} = \left[-(y_3 + K_3)y_4 + K_4\left(\frac{F\bar{D}}{dy_2} - \frac{\bar{D}}{y_2^2}\frac{\mathrm{d}y_2}{\mathrm{d}z}\right)\right] y_1^{-1}, \tag{3.4.5c}$$

$$\frac{\mathrm{d}y_4}{\mathrm{d}z} = \left[\frac{K_3K_5}{K_2y_2^2} - \frac{K_1}{K_2y_2^2} - \frac{2y_4}{y_2}\right]\frac{\mathrm{d}y_2}{\mathrm{d}z} + \frac{K_6}{K_2y_2^2}\frac{\mathrm{d}y_3}{\mathrm{d}z}, \tag{3.4.5d}$$

where

$$K_1 = \frac{g\rho^l_{Fe}\Delta V^{s,l}_{Fe,O}}{L}, \tag{3.4.6a}$$

$$K_2 = \frac{1000R}{a_O L}, \tag{3.4.6b}$$

$$K_3 = v_s\rho^l_{Fe}, \tag{3.4.6c}$$

$$K_4 = \frac{g{\rho^l_{Fe}}^2\Delta V^{s,l}_{Fe,O}a_O}{1000R}, \tag{3.4.6d}$$

$$K_5 = \frac{c_p}{k}, \tag{3.4.6e}$$

$$K_6 = \frac{L}{k}, \tag{3.4.6f}$$

are constants. The slurry equations are solved subject to boundary conditions

$$y_1(d) = \xi_T, \tag{3.4.7a}$$

$$y_2(d) = T_a(d), \tag{3.4.7b}$$

$$y_3(0) = -v_s\rho^s_{Fe}, \tag{3.4.7c}$$

$$y_3(d) = 0, \tag{3.4.7d}$$

$$y_4(0) = \frac{Q^i_s}{kK_2T^2} - \frac{K_1}{K_2T}, \tag{3.4.7e}$$

and the eigenvalue F is determined subject to $y_3(d) = 0$.

3.5 Results and discussion

We investigate the effect of layer thickness, variations of the ICB heat flux and the impact of high versus low thermal conductivity on a non-convecting, steady state slurry layer. We solve the boundary value problem outlined in Section 3.4 to determine the temperature, light element in the liquid phase and solid flux across the layer. Plots of

the solid fraction are obtained from the solid flux via the mobility model (2.7.4), and are not computed from the BVP itself. All of the solutions should be consistent with geophysical constraints such as the seismic density jump across the layer, and give plausible CMB heat fluxes as described in Section 3.3. All parameters are kept fixed as listed in Table 3.1.

Given the range of layer depths inferred from seismology in Table 3.1 and the uncertainty in estimates of the ICB heat flux, layer thicknesses between $150\,\mathrm{km}$ and $300\,\mathrm{km}$ at different rates of secular cooling, Q_s^i, are investigated. Initially a fixed thermal conductivity with a high value of $107\,\mathrm{W\,m^{-1}\,K^{-1}}$ (Davies *et al.*, 2015) and a young inner core age of $0.5\,\mathrm{Ga}$ is investigated.

Figure 3.6 shows profiles of ξ^l, T, $|j_z|$ and ϕ/ϕ_B for a range of depths with $Q_s^i = 1.6\,\mathrm{TW}$. The solid flux is always negative since iron particles fall towards the ICB under gravity in the negative $\hat{\mathbf{z}}$-direction and its absolute value is plotted. The solid fraction is normalised by its value at the base of the layer, ϕ_B. An increase in light element concentration to the outer core value of 8 mol.% is clearly observed, and its depressing effect on the liquidus towards the top of the layer is evidenced by the steepening temperature gradient. Throughout the layer the solid flux remains close to its value predetermined by the inner core growth rate, v_s, at the ICB and then quickly decreases to zero at the top where the effect of barodiffusion is enhanced by the turbulent mixing layer. The solid fraction profile follows the behaviour of the solid flux, since they are related by using Stokes flow as a model of mobility (2.7.4). The temperature at the CSB is continuous, hence at the top of the layer the liquidus temperature is equal to the adiabatic temperature. A departure in temperature from the anchor point for the adiabat is evident at the base of the layer, since the actual temperature at the ICB increases due to the latent heat transported there by falling solid particles that have crystallised in the slurry. The slurry has developed an equilibrium by balancing

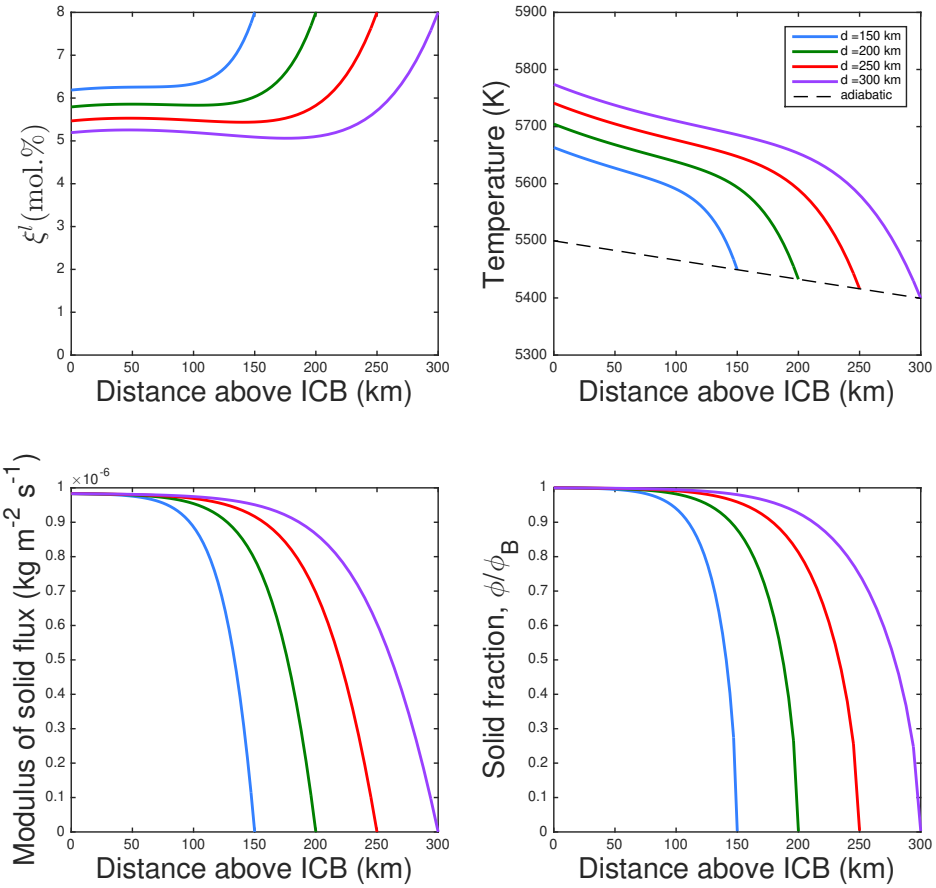

Figure 3.6: (Clockwise from top left) Profiles of ξ^l, temperature, solid fraction normalised by its value at the base of the layer, ϕ_B, and the absolute value of the solid flux. Layer thickness is indicated by the legend. Secular cooling of the inner core is fixed at $Q_s^i = 1.6\,\mathrm{TW}$ and the thermal conductivity is equal to $107\,\mathrm{W\,m^{-1}\,K^{-1}}$, with an inner core age of $\tau_i = 0.5\,\mathrm{Ga}$.

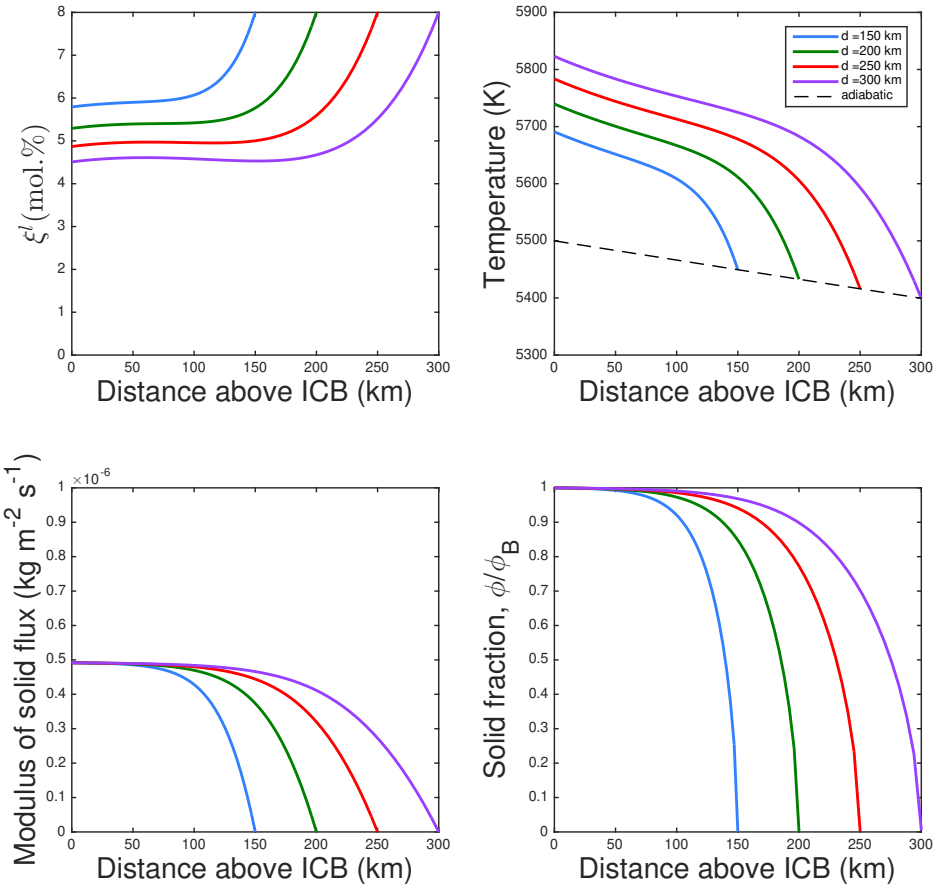

Figure 3.7: (Clockwise from top left) Profiles of ξ^l, temperature, solid fraction normalised by its value at the base of the layer, ϕ_B, and the absolute value of the solid flux. Layer thickness is indicated by the legend. Secular cooling of the inner core is fixed at $Q_s^i = 0.8\,\mathrm{TW}$ and the thermal conductivity is equal to $50\,\mathrm{W\,m^{-1}\,K^{-1}}$, with an inner core age of $\tau_i = 1\,\mathrm{Ga}$.

the latent heat released by the freezing iron snow with the heat lost by cooling so that the temperature is on the liquidus everywhere in the layer.

We compare lower estimates of the thermal conductivity to the solutions obtained with a higher thermal conductivity. A lower value of $k = 50\,\mathrm{Wm^{-1}\,K^{-1}}$ (Konôpková *et al.*, 2016), and an older inner core age of $1\,\mathrm{Ga}$ is selected. The steady state is sensitive to the inner core age through the speed of ICB advance, v_s, defined at the base of the slurry, and this enters the boundary condition (3.4.2d) for the solid flux.

Profiles for a range of depths with a fixed secular cooling of $Q_s^i = 0.8\,\mathrm{TW}$ are given in Figure 3.7. The speed of ICB advance has halved, resulting in the same factor of reduction in the solid flux imposed at the base of the layer. In comparison to the higher thermal conductivity solutions the reduction in solid flux yields a reduction in the light element concentration at the ICB, as less freezing occurs to partition light element into the liquid. Less light element in the liquid overall reduces the depression in the liquidus temperature. A lower thermal conductivity restricts the amount of heat that can be conducted through the layer along the adiabat, so more heat must be transported by the slurry and increases the temperature compared to the higher thermal conductivity case.

Figure 3.8 shows the density and P wave speed profiles compared with PREM as a function of radius, where a high and low thermal conductivity case is tested. Layer thickness is varied between $150 - 300\,\mathrm{km}$. The total density is calculated by adding the fluctuations (2.9.1j) to the hydrostatic part (3.3.5). P wave speed (1.2.1) is determined by (1.2.1)

$$v_p = \sqrt{\frac{K_s}{\rho}},$$

where the bulk modulus, K_s, is taken from PREM. Plots of the density all show a stably stratified layer, with less dense material overlaying more dense material. The corresponding plots of P wave speed demonstrate the decrease in speed because of

the density stratification compared with PREM. Seismic evidence suggests that the slowdown in speed is about 0.7 – 0.8% (see Chapter 1). For the high conductivity case the slowdown is around 0.2% whereas for the low conductivity case, the slowdown is around 0.3%.

Figure 3.9 shows a phase diagram of solutions to the steady state model comparing high and low thermal conductivity solutions. It shows that a wide range of solutions satisfy the geophysical constraints on the density jump and the CMB heat flux. Increasing the layer thickness increases the density jump across the layer at a fixed Q_s^i, and similar increases in density jump are observed when increasing Q_s^i for a fixed layer depth. There is a proportional increase in the CMB heat flux with layer thickness since a larger slurry volume releases more latent heat, and more secular cooling arises because the liquidus gradient is steeper than the adiabat. Very high estimates of the CMB heat flux are attained with $Q_s^i = 2\,\mathrm{TW}$ for thicker layers with a high thermal conductivity.

Lower thermal conductivity models with smaller layer thicknesses can comfortably provide acceptable solutions with lower rates of inner core secular cooling. Less heat is conducted down the adiabat, and therefore more heat must be transported by the slurry compared to high thermal conductivity models. The temperature drop and hence the density jump increases across the layer in turn. Conversely, a higher thermal conductivity decreases the density jump across the layer significantly, since more heat is conducted along the adiabat and reduces the temperature drop across the slurry. A larger density jump requires a greater layer thickness and/or stronger heating from inner core secular cooling to compensate.

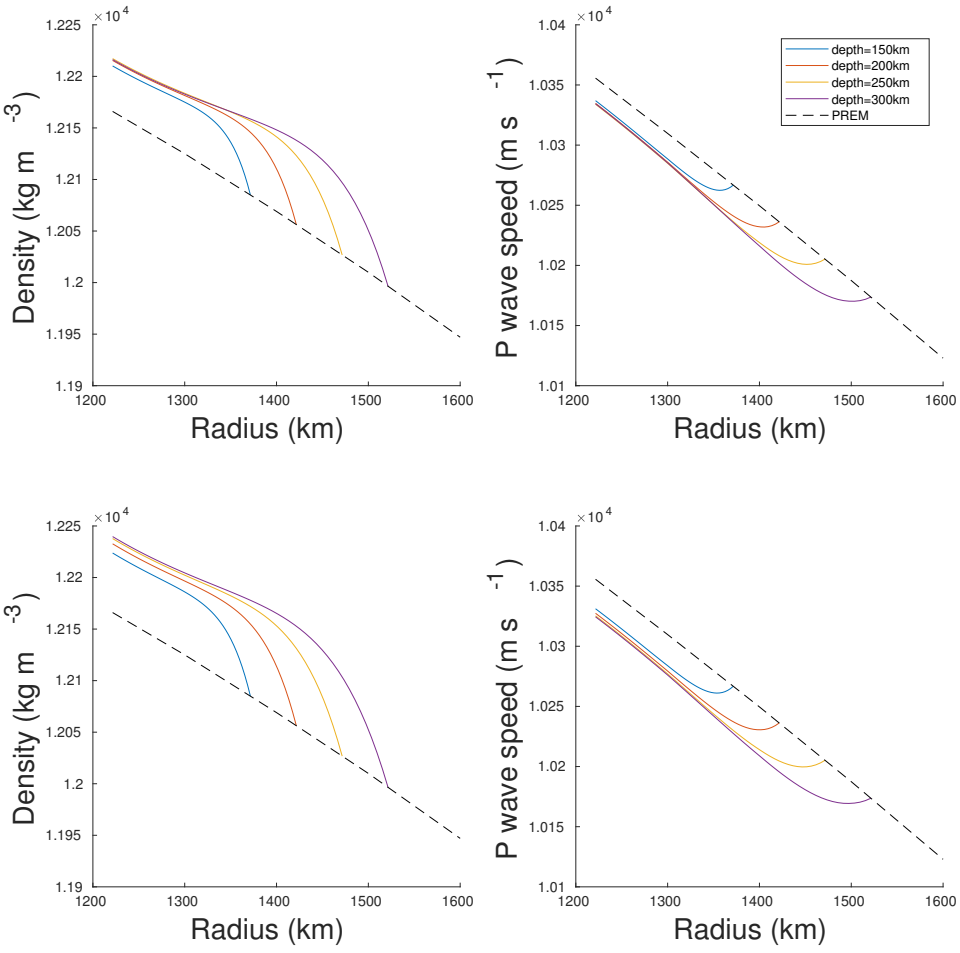

Figure 3.8: Density and P wave speed over distance above the ICB compared with PREM for a range of fixed layer thicknesses between 150 and 300 km. (Top row) $Q_s^i = 1.6$ TW, $k = 107$ $\mathrm{Wm^{-1}K^{-1}}$, $\tau_i = 0.5$ Ga. (Bottom row) $Q_s^i = 0.8$ TW, $k = 50$ $\mathrm{Wm^{-1}K^{-1}}$, $\tau_i = 1.0$ Ga.

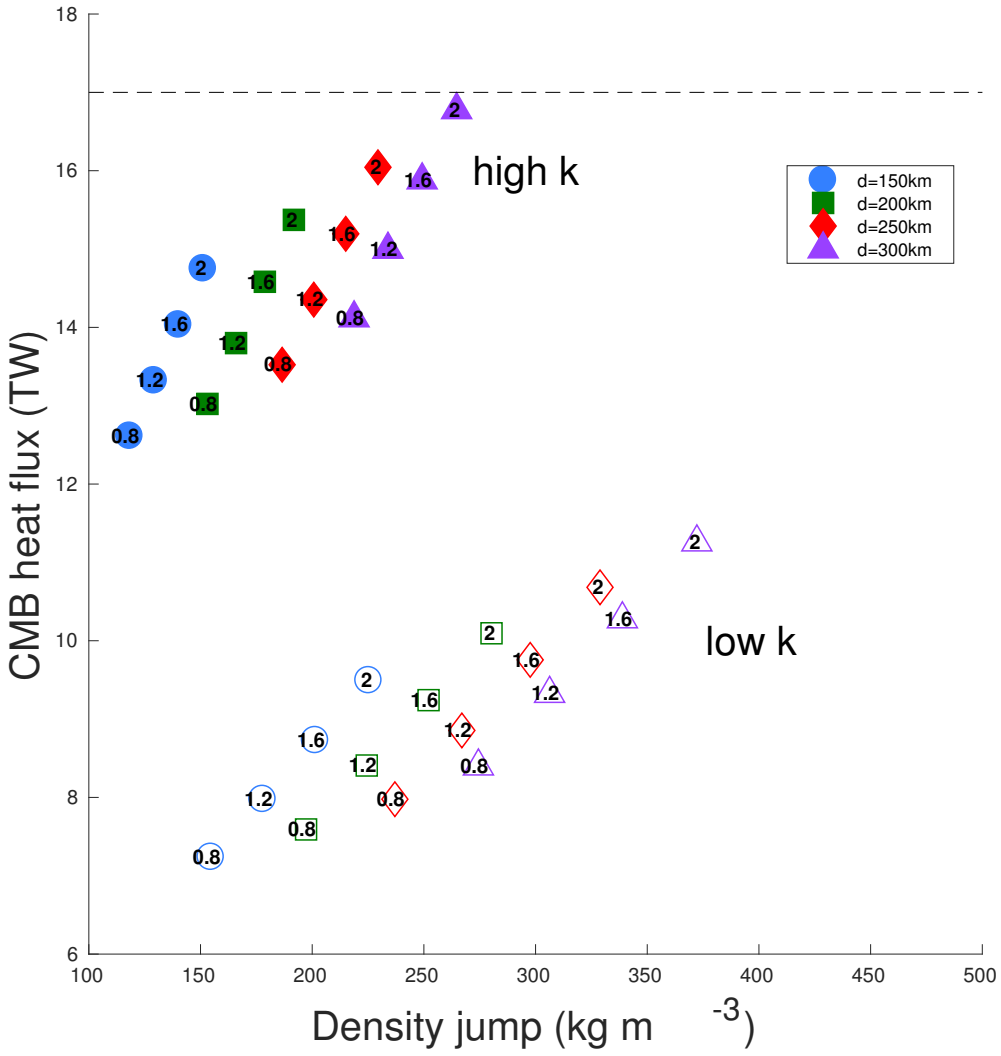

Figure 3.9: A phase diagram of steady state solutions of the slurry. Layer thicknesses are indicated by the symbols in the legend. The imposed inner core secular cooling (in TW) is given by the numbers enclosed. High conductivity solutions are grouped by filled in symbols, whereas low conductivity solutions are grouped by unfilled symbols. Along the x-axis is the calculated density jump and the y-axis is the CMB heat flux. The maximum density jump inferred from seismology is $720\,\mathrm{kg\,m^{-3}}$ and the maximum CMB heat flux is marked by the dashed line at $17\,\mathrm{TW}$

3.6 Summary

We have developed a simplified model of a slurry system to explain the dynamics of a seismically distinct layer at the base of the Earth's outer core. We propose that the F-layer can be explained by a slurry layer where stable stratification arises from particles of iron freezing out of the liquid alloy. As the iron particles fall under the influence of gravity, residual light element migrates towards the CSB into the rest of the outer core to help power the geodynamo. A steady state slurry zone that is chemically stable and on the liquidus temperature everywhere is consistent with the seismically inferred density jumps for a range of layer thicknesses and inner core secular cooling. Sensible values of the total CMB heat flux are achieved, using both high and low thermal conductivity. Greater layer thickness, secular cooling at the ICB and lower thermal conductivity tend to favour a larger density jump.

The steady state slurry model presented in the chapter provides a good dynamical description of the present day F-layer that agrees with current geophysical constraints. In the proceeding chapters we test our assumptions on how an evolving slurry layer coupled to the thermal history of the core could answer questions surrounding the origins of a slurry F-layer. While this box model generally satisfies the geophysical constraints, relatively high values of the heat flux through the CMB and hence a high rate of inner core cooling is required. This is needed to keep the slurry on the liquidus near the ICB. In Chapter 4 the boundary conditions of the slurry system is further developed so that the global heat balance of the core remains consistent. A transformation from a Cartesian box model to a spherical geometry is performed and a possible physical scenario leading to a higher heat flux at the ICB is investigated.

Chapter 4

A steady-state spherical model

Contents

In this chapter we extend the box model of Chapter 3 and develop a steady state slurry in spherical coordinates to match the geometry of the core. Appropriate boundary conditions are developed so that the slurry volume is coupled to the liquid outer core and solid inner core in a consistent manner. We formulate a boundary value problem and the steady state solutions obtained will be used to initialise the time-dependent model in Chapter 5. For this reason, it is important that the boundary conditions imposed are consistent. The objective of this chapter is to seek stably-stratified solutions that match the seismic observations of the present day F-layer. Results will be used to explain the evolution of the F-layer in the next chapter using a time-dependent model.

A schematic of the spherical steady state model is given in Figure 4.1.

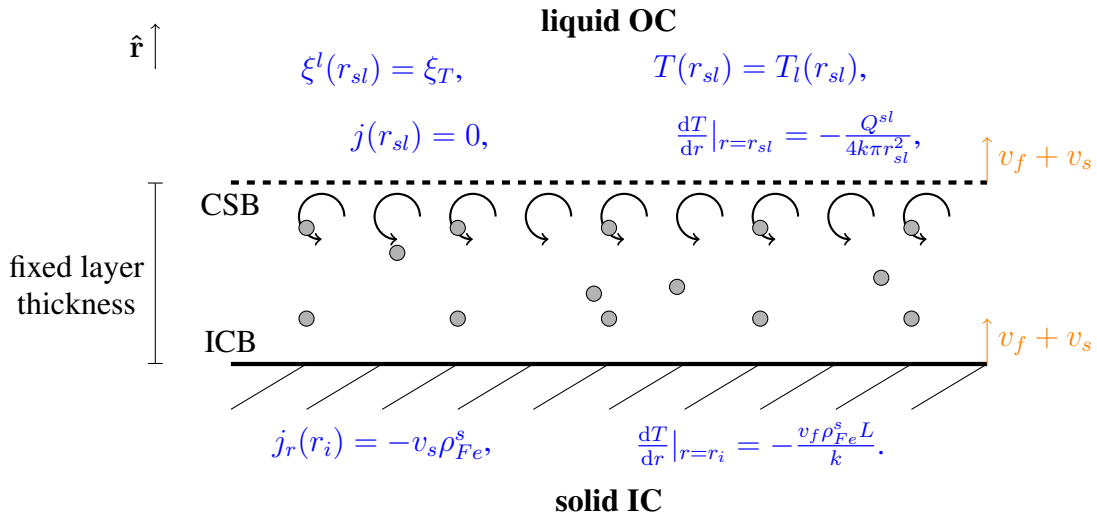

Figure 4.1: A schematic of the boundary conditions imposed on the spherical steady state slurry problem. The system is solved subject to six boundary conditions.

4.1 Spherical geometry

We solve the steady slurry equations in spherical coordinates to account for geometric effects. Recall the temperature equation (2.9.1d)

$$\rho^l_{Fe} c_p \frac{\mathrm{D}T}{\mathrm{D}t} = \nabla \cdot (k\nabla T + L\mathbf{j}) + \rho^l_{Fe} L \frac{\mathrm{D}\phi}{\mathrm{D}t}. \tag{4.1.1}$$

In the $\phi \ll 1$ limit the last term on the RHS is assumed to be negligible, i.e. $\frac{\mathrm{D}\phi}{\mathrm{D}t} \to 0$. In spherical coordinates, the divergence for a radially dependent slurry is

$$\nabla \cdot \mathbf{A} = \frac{1}{r^2} \frac{\partial \left(r^2 A_r\right)}{\partial r}.$$

Therefore (4.1.1) in spherical coordinates is

$$\frac{\mathrm{D}T}{\mathrm{D}t} = \kappa \frac{\partial^2 T}{\partial r^2} + \frac{2\kappa}{r}\frac{\partial T}{\partial r} + \frac{L}{\rho^l_{Fe} c_p}\frac{\partial j_r}{\partial r} + \frac{2L}{r\rho^l_{Fe} c_p} j_r, \tag{4.1.2}$$

where $\kappa = k/\rho^l_{Fe} c_p$ is the thermal diffusivity, and we have assumed the slurry remains static ($\mathbf{u} = 0$).

Recall the light element equation (2.9.1b)

$$\rho^l_{Fe} \frac{\mathrm{D}\xi}{\mathrm{D}t} = -\nabla \cdot \mathbf{i} \tag{4.1.3}$$

and the light element flux from (3.1.20)

$$i_r = \frac{g {\rho^l_{Fe}}^2 \bar{D} \Delta V^{s,l}_{Fe,O} a_O}{1000RT} - \xi^l j_r. \tag{4.1.4}$$

In spherical coordinates, (4.1.3) together with (4.1.4) becomes

$$\rho_{Fe}^{l}\frac{\mathrm{D}\xi}{\mathrm{D}t} = K_4\left[\frac{\bar{D}}{T^2}\frac{\partial T}{\partial r} - \frac{1}{T}\frac{\partial \bar{D}}{\partial r} - \frac{2}{r}\frac{\bar{D}}{T}\right] + \left(\xi^l\frac{\partial j_r}{\partial r} + j_r\frac{\partial \xi^l}{\partial r} + \frac{2}{r}\xi^l j_r\right) \tag{4.1.5}$$

where $K_4 = g{\rho_{Fe}^{l}}^2\Delta V_{Fe,O}^{s,l}a_O/1000R$ (3.4.6d), and we use $r = r_i + z$ to write the functional form of the diffusion coefficient, $\bar{D}$ (3.1.19) as

$$\bar{D} = D_O \exp\left(\frac{F(r-r_i)}{d}\right). \tag{4.1.6}$$

In spherical coordinates, the liquidus equation is given by

$$\frac{\partial T}{\partial r} = -g(r)K_1 T - K_2 T^2\frac{\partial \xi^l}{\partial r}, \tag{4.1.7}$$

where $K_1 = \rho_{Fe}^{l}\Delta V_{Fe,O}^{s,l}/L$ and $K_2 = 1000R/a_O L$. The constants K_1, K_2 and K_4 (3.4.6) are the same values used in the box model with the same physical properties given in Table 3.1, since quantities such as the latent heat do not vary greatly in a steady state slurry layer.

4.2 Boundary conditions

The slurry ODEs form a fourth order system, however in this section we develop six boundary conditions compared with the five boundary conditions used in the box model. There are two boundary conditions on the heat flux at the ICB and CSB, two boundary conditions on the solid flux at the ICB and CSB, one boundary condition on the light element concentration at the CSB and one boundary condition on the temperature at the CSB. Compared with the box model, the extra condition comes from the heat flux imposed at the CSB. This is used to determine the snow speed, v_s, at which

the ICB moves due the accumulation of iron particles snowing from the slurry.

We improve the ICB heat flux condition from the previous box model so that it is closer to geophysical reality. We assume that the inner core is isothermal. In reality the inner core is likely to be somewhere between isothermal and adiabatic since the thermal diffusion timescale is $t_\kappa = r_i^2/\kappa \simeq 1.9$ Ga (Pozzo *et al.*, 2014), which is longer than the oldest estimates of the inner core age of around 1 Ga. If the inner core is convecting then the superadiabatic temperature is effectively 'frozen in' at the melting point in the limit of zero thermal conductivity. If the inner core is isothermal then the inner core cannot convect and the heat flux across the ICB is zero, because a high thermal conductivity rapidly exchanges heat away so that no temperature gradients can exist. Pozzo *et al.* (2014) use a core cooling rate of $\frac{\mathrm{d}T_c}{\mathrm{d}t} = -100\ \mathrm{KGa}^{-1}$ to show that the secular cooling of the inner core is $Q_s^i = 0.3$ TW, whereas the adiabatic heat flux is $Q_a^i = 1.6$ TW. Assuming that there is no radiogenic heating in the inner core, this indicates that the inner core is very subcritical because $Q_s^i < Q_a^i$. If the inner core was assumed to be neutrally stable so that $Q_s^i = Q_a^i$, then this would require a much higher cooling rate of $\frac{\mathrm{d}T_c}{\mathrm{d}t} = -540\ \mathrm{KGa}^{-1}$, which corresponds to an extremely high CMB heat flux of 66 TW. This value is implausible, since the surface heat flux of the Earth is estimated to be 47 ± 2 TW (Davies & Davies, 2010).

If we assume that the inner core is subadiabatic, then the temperature gradient at the ICB is too shallow to get onto the liquidus. If we assume that the inner core is adiabatic then we would require an inner core that can release heat for a long time, which has already been shown to be geophysically implausible. However we overcome this by supposing that there exists an infinitely thin shell at the inner core surface where direct freezing occurs, which introduces a freezing speed denoted by v_f separate from the ICB snow speed, v_s, originally introduced in the coordinate transform in the steady model (3.1.1). The freezing speed is a kinematic velocity rather than a fluid velocity,

and is fixed at a constant value. This releases the latent heat necessary to elevate the temperature gradient onto the liquidus in the slurry and maintain an isothermal inner core. This model improves on the traditional model of iron freezing directly onto the ICB, which does not explain the stable F-layer, and the box model in Chapter 3, which did not consider an isothermal inner core. We adjust the previous coordinate transform (3.1.1) to a spherical geometry by

$$r = r' - vt, \qquad t = t', \tag{4.2.1}$$

The ICB advances through the combination of iron particles settling and accumulating at the base of the F-layer, given by the snow speed v_s, as well as through direct freezing, v_f. Therefore the total speed of ICB advance is the sum of these two components

$$v \equiv \dot{r}_i = v_s + v_f, \tag{4.2.2}$$

and the material derivative becomes

$$\frac{\mathrm{D}f}{\mathrm{D}t} \equiv -v\frac{\partial f}{\partial r}$$

for an arbitrary scalar function f. The latent heat flux at the ICB released from direct freezing is therefore given by

$$Q_l^i = 4\pi r_i^2 v_f \rho_{Fe}^s L \qquad \text{at } r = r_i \tag{4.2.3}$$

and replaces the ICB heat flux, Q_s^i, (3.4.2c) that is no longer specified since the core is

isothermal. The condition on the temperature gradient at the ICB becomes

$$\left.\frac{\partial T}{\partial r}\right|_{r=r_i} = -\frac{v_f \rho_{Fe}^s L}{k}. \tag{4.2.4}$$

Compared to the previous box model, an extra condition is provided on the heat flux at the CSB that will eventually couple the slurry with the thermal evolution of the liquid outer core in the time-dependent model of Chapter 5. At the CSB we impose

$$\left.\frac{\partial T}{\partial r}\right|_{r=r_{sl}} = -\frac{Q^{sl}}{4k\pi r_{sl}^2}, \tag{4.2.5}$$

where the CSB heat flux, Q^{sl}, is prescribed and time-independent for now. A high thermal conductivity estimate of $k = 107\ \mathrm{Wm^{-1}K^{-1}}$ is used throughout to be consistent with the value used in Chapter 3 (see Table 3.1).

Light element concentration remains continuous at the CSB and is fixed at a value of $\xi_T = 8\ \mathrm{mol.\%}$. Temperature is also continuous at the CSB and is equal to the liquidus temperature, T_l, given by the melting data obtained from *ab initio* calculations. The liquidus data for a core composition of $Fe_{0.82}Si_{0.10}O_{0.08}$ (Pozzo *et al.*, 2013) is available as a polynomial fit given by Davies *et al.* (2015) as a function of pressure, p, in GPa given by

$$T_l(p) = a_0 + a_1 p + a_2 p^2 + a_3 p^3, \tag{4.2.6}$$

where the coefficients a_n are given in Table 4.1. Although the slurry model assumes a binary Fe-O alloy, its melting curve is not defined clearly in the literature. The assumed composition of the core may significantly alter the results of this model through the temperature condition at the CSB, but the exact nature of the light elements present in the core remain under debate (see Chapter 1).

Additionally, the solid flux at the ICB remains proportional to the speed of IC

n	0	1	2	3
a_n	1698.55	27.3351	-0.0664736	7.94628×10^{-5}

Table 4.1: Table of interpolation constants a_n used to approximate the liquidus T_l for a core composition of $Fe_{0.82}Si_{0.10}O_{0.08}$ (Pozzo *et al.*, 2013) according to a polynomial fit (4.2.6) given by Davies *et al.* (2015).

growth, v_s, due to accumulating iron particles where

$$j_r = -v_s \rho^s_{Fe} \qquad \text{at } r = r_i, \tag{4.2.7}$$

however v_s is no longer fixed and is an eigenvalue to be determined by the BVP now that there is an extra boundary condition on the CSB heat flux. The solid flux at the CSB is equal to zero as before in the box model (3.4.2e), so we impose

$$j_r = 0 \qquad \text{at } r = r_{sl}, \tag{4.2.8}$$

which is met by invoking a turbulent mixing layer that enhances barodiffusion at the CSB, and the mixing parameter F is an eigenvalue to be determined by the BVP that controls the exponential form of the self-diffusion coefficient of oxygen given by (4.1.6).

4.3 Boundary value problem

In summary the time-independent $\left(\frac{\partial}{\partial t} \to 0\right)$ slurry equations to be solved in a spherical geometry (see equations 4.1.2, 4.1.5, 4.1.7) are

$$\frac{\partial T}{\partial r} = -\frac{T\Delta V_{Fe}^{s,l}}{L} g\rho_{Fe}^{l} - \frac{RT^2 1000}{a_O L}\frac{\partial \xi^l}{\partial r} \tag{4.3.1}$$

$$\xi^l \frac{\partial j_r}{\partial r} = \frac{1}{r^2}\frac{\partial}{\partial r}\left(\frac{r^2 g {\rho_{Fe}^{l}}^2 \bar{D}\Delta V_{Fe,O}^{s,l}}{TR\frac{1000}{a_O}}\right) - \left(v\rho_{Fe}^{l} + j_r\right)\frac{\partial \xi^l}{\partial r} - \frac{2}{r}\xi^l j_r, \tag{4.3.2}$$

$$-k\frac{\partial^2 T}{\partial r^2} = v\rho_{Fe}^{l} c_p \frac{\partial T}{\partial r} + L\frac{\partial j_r}{\partial r} + \frac{2k}{r}\frac{\partial T}{\partial r} + \frac{2L}{r} j_r, \tag{4.3.3}$$

and the self-diffusion coefficient takes an exponential form (4.1.6) given by

$$\bar{D} = D_O \exp\left(\frac{F\left(r - r_i\right)}{d}\right).$$

A side-by-side comparison of the boundary conditions used in the box model and the spherical model is given in Table 4.2. Note that compared with the box model, there is an extra boundary condition on the CSB heat flux that determines the extra free parameter, v_s, that enters the solid flux condition at the ICB. Similarly the mixing parameter, F, is also an eigenvalue to be determined by imposing zero solid flux at the CSB.

The boundary value problem is solved as before using MATLAB function `bvp4c`, and requires formulating the problem as a system of first order differential equations. We label the variables

$$y_1 = T, \tag{4.3.4a}$$

$$y_2 = \xi \tag{4.3.4b}$$

$$y_3 = j, \tag{4.3.4c}$$

Box model	Spherical model
$-4k\pi r_i^2 \frac{\partial T}{\partial z}\big\vert_{z=0} = Q_s^i$	$-4k\pi r_i^2 \frac{\partial T}{\partial r}\big\vert_{r=r_i} = 4\pi r_i^2 v_f \rho_{Fe}^s L$
	$-4k\pi r_{sl}^2 \frac{\partial T}{\partial r}\big\vert_{r=r_{sl}} = Q^{sl}$
$\xi(d) = \xi_T$	$\xi(r_{sl}) = \xi_T$
$j_z(d) = 0$	$j_r(r_{sl}) = 0$
$j_z(0) = -\rho_{Fe}^s v_s$	$j_r(r_i) = -\rho_{Fe}^s v_s$
$T(d) = T_a(d)$	$T(r_{sl}) = T_l(r_{sl})$

Table 4.2: A side-by-side comparison of the boundary conditions applied to box model and the spherical problem.

so equations (4.3.1)–(4.3.3) become

$$\frac{\partial y_1}{\partial r} = y_4, \tag{4.3.5a}$$

$$\frac{\partial y_2}{\partial r} = -\frac{K_1}{K_2 y_1} - \frac{y_4}{K_2 y_1^2}, \tag{4.3.5b}$$

$$\frac{\partial y_3}{\partial r} = \frac{1}{y_2}\left\{-(vK_3 + y_3)\frac{\partial y_2}{\partial r} - \frac{2}{r}y_2 y_3 + K_4\left(\frac{F\bar{D}}{dy_1} - \frac{\bar{D}y_4}{y_1^2} + \frac{2\bar{D}}{ry_1}\right)\right\}, \tag{4.3.5c}$$

$$\frac{\partial y_4}{\partial r} = -vK_3K_5y_4 - \frac{2}{r}y_4 - K_6\frac{\partial y_3}{\partial r} - \frac{2K_6}{r}y_3 \tag{4.3.5d}$$

and are solved subject to boundary conditions

$$y_2(r_{sl}) = \xi_T, \tag{4.3.6a}$$

$$y_1(r_{sl}) = T_l(r_{sl}), \tag{4.3.6b}$$

$$y_4(r_i) = -\frac{v_f \rho_{Fe}^s L}{k}, \tag{4.3.6c}$$

$$y_4(r_{sl}) = -\frac{Q^{sl}}{4k\pi r_{sl}^2}, \tag{4.3.6d}$$

$$y_3(r_i) = -\rho_{Fe}^s v_s, \tag{4.3.6e}$$

$$y_3(r_{sl}) = 0, \tag{4.3.6f}$$

where constants K_1 to K_6 are given by (3.4.6), except that $K_3 = \rho^l_{Fe}$ so that $v = v_f + v_s$ is no longer held constant. Physical and material properties given in Table 3.1 remain the same unless stated otherwise in the text.

4.4 Results and discussion

We vary the CSB heat flux, Q^{sl}, freezing speed, v_f, and the layer thickness, d, to seek stably-stratified solutions that are suitable for initialising the time dependent system in Chapter 5. If we assume that the ICB heat flux, Q^i_s, is between 0.5 and 2 TW (Pozzo *et al.*, 2014), then

$$v_f = \frac{Q^i_s}{4\pi r_i^2 \rho^s_{Fe} L} \tag{4.4.1}$$

gives a freezing speed range of $2.8 \leq v_f \leq 11.2 \times 10^{-12}$ ms^{-1}. The CSB heat flux is a geophysically uncertain value, so we widely vary the CSB heat flux between 1 and 6 TW. The CSB heat flux is added to the secular cooling, Q^l_s, and gravitational power, Q^l_g, of the liquid outer core to obtain the total CMB heat flux. Plausible estimates of the CMB heat flux are in the range of $5 \leq Q^c = Q^{sl} + Q^l_s + Q^l_g \leq 17$ TW (see Table 3.1).

Figure 4.2 shows steady state results for a fixed layer thickness of 150 km and $v_f = 2.8 \times 10^{-12}$ ms^{-1} (which corresponds to an ICB heat flux of 0.5 TW), where the CSB heat flux is varied between 1 and 6 TW. Primarily the oxygen profiles are unstable and decrease from an ICB concentration that is higher than the imposed CSB value for solutions with $1 \leq Q^{sl} \leq 4$ TW. For higher CSB heat flows the oxygen concentration at the ICB is lower than the fixed CSB value, though the layer remains unstable in the region immediately above the ICB and then stabilises part way through the layer as the radius increases. The parameter most responsible for this effect is the freezing speed, v_f, because this sets the ICB temperature gradient and hence the ICB oxygen gradient

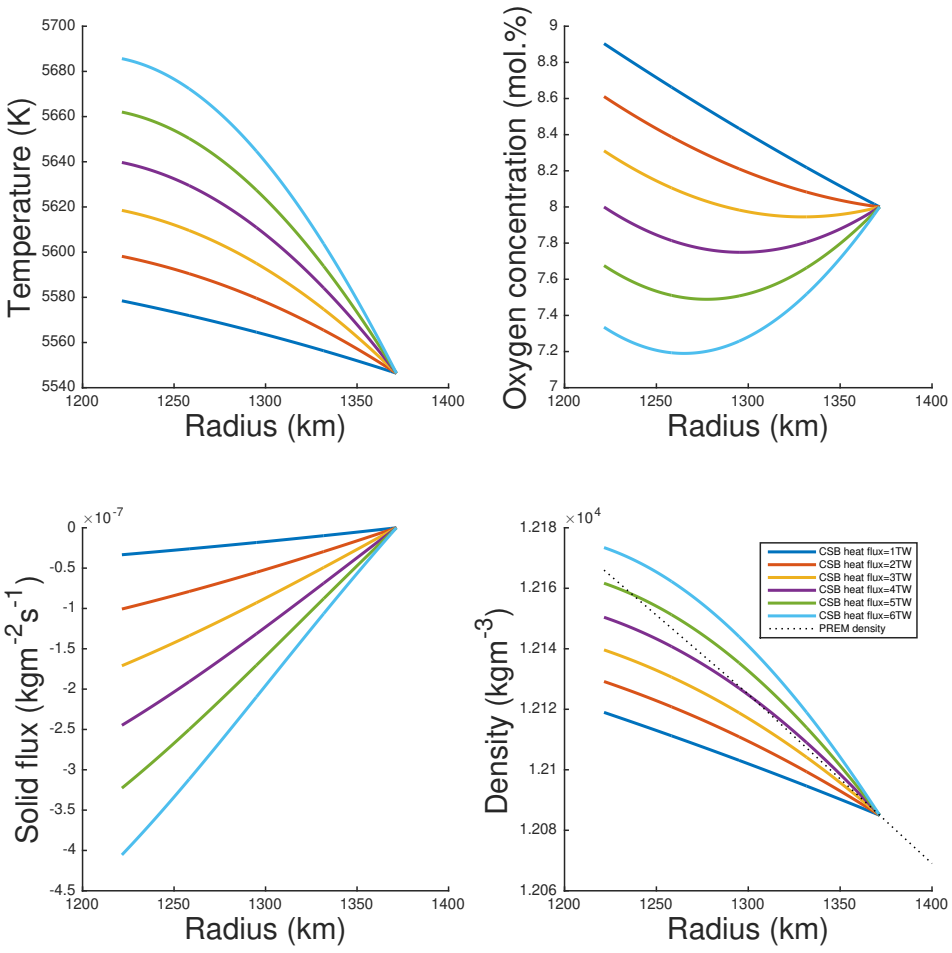

Figure 4.2: Profiles of the temperature, oxygen concentration, solid flux and density over radius for CSB heat fluxes between 1 and 6 TW. Layer thickness is fixed at 150 km and freezing speed is fixed at 2.8×10^{-12} ms^{-1}. (Bottom right) Dotted line refers to the PREM density.

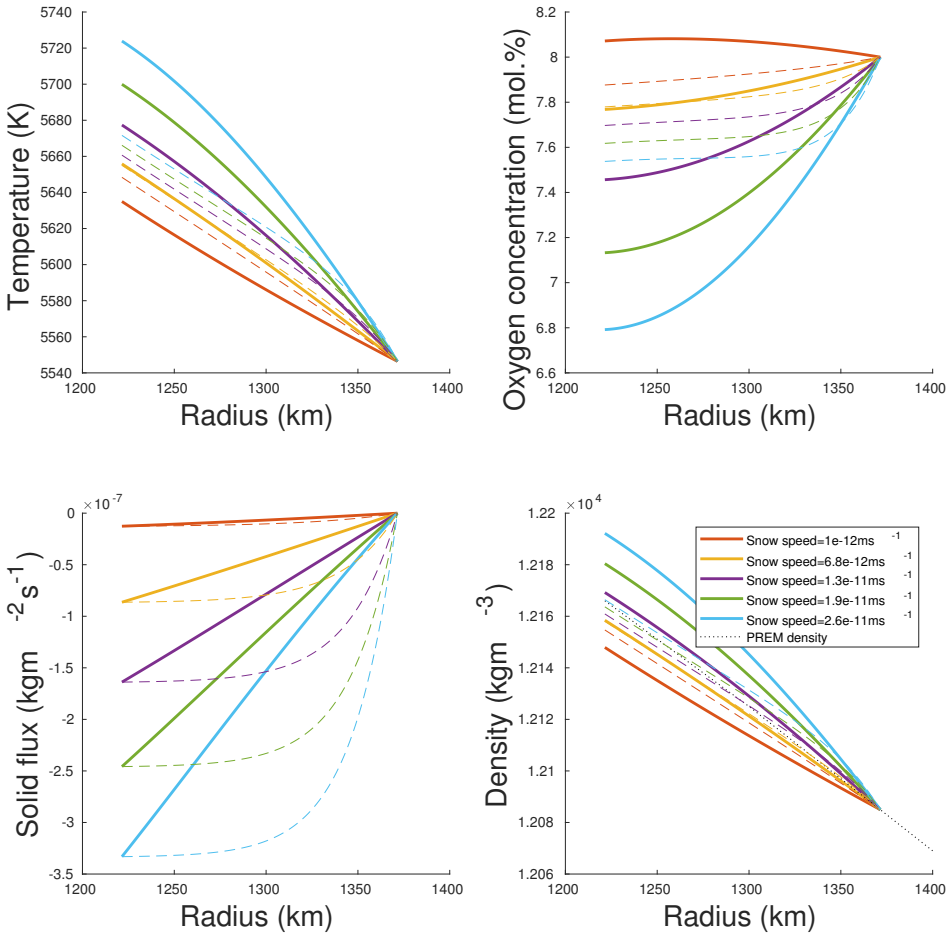

Figure 4.3: Comparison of temperature, oxygen concentration, solid flux and density profiles between the spherical model (solid) and the box model (dashed). CSB heat fluxes between 2 and 6 TW in the spherical case correspond with the same colour key shown in Figure 4.2. Layer thickness, d, is fixed at 150 km and freezing speed, v_f, is fixed at 11.2×10^{-12} ms^{-1}. Snow speeds determined by the spherical model vary between 0.10×10^{-11} ms^{-1} and 2.6×10^{-11} ms^{-11}, which are input as fixed values into the box model. (Bottom right) Dotted line refers to the PREM density.

through the liquidus. The chosen value of the thermal conductivity also affects the ICB temperature gradient, where we have used a value of $k = 107\ \mathrm{Wm^{-1}K^{-1}}$. For a stable oxygen configuration, a positive ICB gradient is desirable. The temperature profiles are related to the oxygen profiles through the liquidus, and monotonically decrease from the ICB temperature to the imposed temperature at the CSB. The solid flux follows a more linear profile, whereas previously in the box model the profile was constant throughout the majority of the layer before sharply decreasing to zero as determined by the turbulent mixing layer (note that the plots in Chapter 3 show the absolute value of the solid flux, whereas it remains negative here). This difference in behaviour is attributed to the treatment of the solid flux condition at the ICB, in which a fixed value is imposed in the box model whereas the solid flux is free to be determined in the spherical system. An overall density stratification steeper than PREM is not observed for most CSB heat fluxes imposed, with most profiles falling below the PREM density except for the case when $Q^{sl} = 6\ \mathrm{TW}$. Steady state solutions obtained with $d = 150\ \mathrm{km}$ and $v_f = 2.8 \times 10^{-12}\ \mathrm{ms^{-1}}$ are therefore not viable initial states for the time-dependent model.

Figure 4.3 shows results for the same parameter values but with a higher freezing speed of $v_f = 11.2 \times 10^{-12}\ \mathrm{ms^{-1}}$ (which corresponds to an ICB heat flux of $2.0\ \mathrm{TW}$). This is compared with solutions from the steady state box model using equivalent boundary conditions: snow speeds, v_s, determined by the spherical problem and an ICB heat flux of $Q_s^i = 2.0\ \mathrm{TW}$ are input as a fixed values into the box model (see Table 4.2). For simulations with a CSB heat flux of $1\ \mathrm{TW}$, positive values of the solid flux are observed so the solution is rejected because the model of mobility (2.7.4) used to solve for ϕ yields complex values. Also a positive value of the solid flux indicates that solid is moving upwards, which is inconsistent with present-day observations of a stably-stratified F-layer. The same general trends for the increasingly linear behaviour

of the temperature and solid flux is observed when the imposed CSB heat flux is lower. Importantly, the oxygen profiles are stable for all values of the CSB heat flow since the value of the freezing speed is high enough to set a steeper ICB temperature gradient that corresponds with a positive oxygen gradient at the ICB through the liquidus. The concentration increases from an ICB value that varies between 6.8 and 7.8 $\mathrm{mol.\%}$, before approaching the imposed CSB value of 8.0 $\mathrm{mol.\%}$. Density stratification above the PREM density is observed for CSB heat fluxes of 4 TW and above, with an increasing ICB density jump as the CSB heat flux increases.

Compared with the box model, the temperature gradient imposed at the CSB in the spherical model is shallower than the temperature gradient that is free to be determined by the box model. Through the liquidus relation, this presents as a shallower oxygen gradient at the CSB compared with the box model. Temperatures at the ICB in the spherical model are more spread and generally higher than the ICB temperatures found in the box model, and similarly oxygen concentrations at the ICB are more spread and lower than the oxygen concentrations encountered the box model. The solid flux profiles are similar between the spherical and box models for $Q^{sl} = 2$ TW and more prominent deviations are observed at higher CSB heat fluxes, which is an outcome of changing the condition on the solid flux at the ICB. Density stratification in the spherical model is much stronger than the box model for CSB heat flows between 4 and 6 TW.

A greater layer thickness of 300 km is also explored. For freezing speeds of 2.8×10^{-12} ms^{-1} all solutions again contained an unstable oxygen profile, whereas for freezing speeds of 11.2×10^{-12} ms^{-1} all solutions contained a desired stable oxygen profile. Figure 4.4 presents a comparison of results obtained from the spherical and box models for a layer thickness of 300 km. Snow speeds obtained vary between 0.18×10^{-11} ms^{-1} and 2.30×10^{-11} ms^{-1}, and are faster compared with $d = 150$ km.

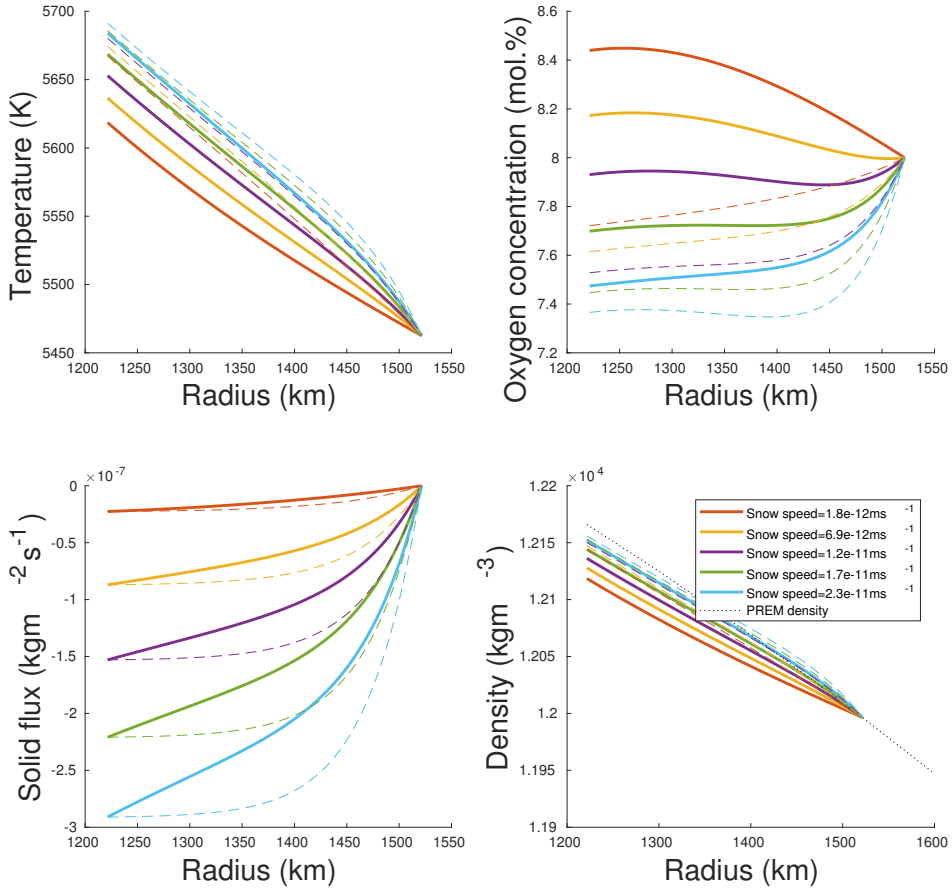

Figure 4.4: Comparison of temperature, oxygen concentration, solid flux and density profiles between the spherical model (solid) and the box model (dashed). CSB heat fluxes between 2 and 6 TW in the spherical case correspond with the same colour key shown in Figure 4.2. Layer thickness, d, is fixed at 300 km and freezing speed, v_f, is fixed at 11.2×10^{-12} ms^{-1}. Snow speeds determined by the spherical model vary between 0.18×10^{-11} ms^{-1} and 2.30×10^{-11} ms^{-11}, which are input as fixed values into the box model. (Bottom right) Dotted line refers to the PREM density.

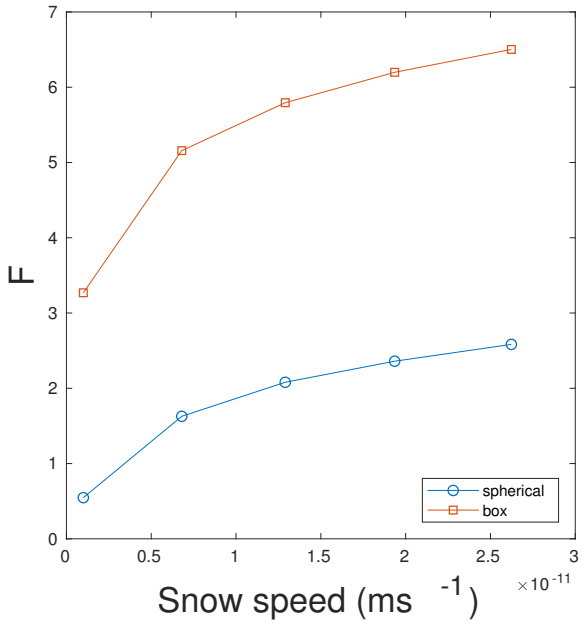

Figure 4.5: Comparing the mixing parameter, F, and snow speed, v_s, between the spherical and box models for $d = 150$ km and $v_f = 11.2 \times 10^{-12}$ ms^{-1}.

The solid flux in the spherical model appears to follow a less linear profile as the CSB heat flow increases for a thicker layer compared with a thinner layer. The CSB temperature is lower when $d = 300$ km because the CSB is located at a lower pressure and corresponds to a lower melting temperature. Overall the temperature curves are less spread at the ICB compared to the case when $d = 150$ km, however the oxygen profiles display a significantly different trend. For $d = 300$ km the oxygen concentration gradient increases more sharply to meet the CSB condition on the oxygen concentration to create an "S" shaped curve, for CSB heat fluxes greater than 2 TW. For $d = 150$ km this shape is significantly less pronounced. In contrast the oxygen gradient decreases as it approaches the CSB for $Q^{sl} = 2$ TW for both layer thicknesses. We proceed with analysing solutions for the thinner layer of 150 km since the oxygen profiles exhibit a more desirable uniform oxygen stratification.

Figure 4.5 shows a comparison of F determined by the box model and the spherical

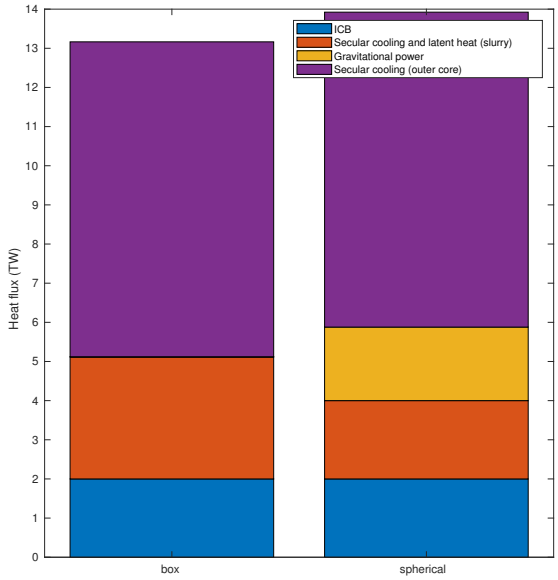

Figure 4.6: Comparing the heat flows between the spherical and box models for $d = 150\ \mathrm{km}$, $v_f = 11.2 \times 10^{-12}\ \mathrm{ms}^{-1}$ and $v_s = 1.3 \times 10^{-11}\ \mathrm{ms}^{-1}$.

model. The mixing parameter F ranges between 0.5 and 2.6 as it increases with a higher snow speed, which corresponds with an increasing CSB heat flux imposed in the spherical model. The greatest difference is found when the snow speed is lowest, whereas the difference lessens at higher snow speeds. The higher values of F in the box model is consistent with the observation that the profiles of the temperature, oxygen concentration and solid flux increase more rapidly towards zero on approach to the CSB compared with the spherical model, due to the enhanced diffusion in the turbulent mixing layer.

Figure 4.6 compares the heat flows between the spherical model and the box model. Layer thickness is fixed at $150\ \mathrm{km}$ and a freezing speed of $v_f = 11.2 \times 10^{-12}\ \mathrm{ms}^{-1}$ is selected, which corresponds to an ICB heat flow of $2.0\ \mathrm{TW}$. Fixing the CSB heat flow in the spherical model at $4.0\ \mathrm{TW}$ yields a snow speed of $v_s = 1.3 \times 10^{-11}\ \mathrm{ms}^{-1}$ that is input into the box model to fix the solid flux condition at the ICB. The proce-

dure for calculating components of the global heat balance is the same as the Cartesian case, where the spherical transform (4.2.1) is applied. The total CMB heat flow adds up to 14.1 TW in the spherical case and 13.2 TW in the box model. The majority of this difference comes from the decrease in gravitational energy in the box model since much shallower gradients in oxygen concentration occur, therefore less compositional energy is released. The gravitational power in the spherical case is 1.9 TW. There is a moderate increase in CSB heat flow to 5.1 TW in the Cartesian geometry, where steeper CSB temperature gradients are encountered compared with the spherical geometry. The secular cooling in the liquid outer core is equal to 8.0 TW in both cases, since the temperature at the CSB determined by liquidus data is evaluated at the same radius since the layer thicknesses are fixed. Hence the adiabat constructed from the CSB to the CMB is the same in both cases, assuming that the core cooling rate, $\frac{\mathrm{d}T_c}{\mathrm{d}t}$, remains the same (see equation 3.3.10) so that an identical amount of specific heat of cooling is computed in the liquid outer core.

4.5 Summary

In this chapter the one-dimensional box model of the steady state slurry outlined in Chapter 3 is extended and transformed into spherical coordinates to reflect the geometry of the core. In anticipation of building a fully time-dependent model, more sophisticated boundary conditions are developed to couple the slurry layer to the inner and outer core volumes in a consistent manner. We assume that the inner core is isothermal, since recent high thermal conductivity estimates suggest that the present-day inner core is not thermally convecting. The heat flux across the ICB is zero for an isothermal inner core, since no temperature gradients exist as heat rapidly leaks from the inner core via conduction. We allow a small amount of interfacial freezing to oc-

cur at the ICB to lift the temperature gradient onto the liquidus in the slurry layer, on account of the fact that in reality the inner core is somewhere between isothermal and adiabatic. Inner core growth associated with interfacial freezing is compounded with the inner core growth related to the accumulation of solid particles produced by the slurry. Hence the ICB speed is composed of two parts: the freezing speed, v_f, and the snow speed, v_s, which is a notable alteration compared with the box model.

Another way that the spherical model differs from the box model is the additional constraint on the CSB heat flux. A prescribed and constant value of the heat flux is imposed on the CSB that in turn specifies the temperature gradient at the CSB. This condition is developed furthermore in Chapter 5 as it becomes regulated by a time-dependent CSB heat flux consistent with the thermal evolution of the entire core. For the purposes of this chapter the CSB heat flux is held constant in order to find a suitable initial condition for the time-dependent system. The total CMB heat flow is calculated by adding the CSB heat flow together with the secular cooling and gravitational power of the liquid outer core.

Other boundary conditions remain the same as the conditions imposed in the box model. This includes imposing a continuous oxygen concentration at the CSB that equals a fixed concentration of $8\ \mathrm{mol.\%}$ found in the bulk of the liquid outer core. The temperature at the CSB is continuous with the melting temperature provided by data from *ab initio* calculations for an $Fe_{0.82}Si_{0.10}O_{0.08}$ alloy. Solid flux at the CSB is set to zero and the solid flux at the ICB remains proportional to the snow speed of accumulating solid particles falling under gravity. In total there are six boundary conditions on the spherical system: two on the heat flux at the ICB and CSB, two on the solid flux at the ICB and CSB, one on the oxygen concentration at the CSB and one on the temperature at the CSB.

The steady state spherical slurry equations form a fourth order system, therefore the

two extra boundary conditions imposed determine the free parameters F, the mixing parameter, and v_s, the snow speed. A boundary value problem is formulated as a series of first order differential equations and solved subject the boundary conditions. We examine the effect of varying the freezing speed, CSB heat flux and layer thickness on the profiles of temperature, oxygen concentration, solid flux and density, as well as on parameters F, v_s and the global heat balance.

For a fixed layer thickness of $150\ \mathrm{km}$, a low freezing speed corresponding to a latent heat flux $0.5\ \mathrm{TW}$ at the ICB resulted in solutions containing unstable oxygen profiles. We identified that a low freezing speed imposed a shallow ICB temperature gradient that relates to a negative ICB oxygen gradient via the liquidus. A high freezing speed corresponding with an ICB latent heat flux of $2\ \mathrm{TW}$ is great enough to overcome negative pressure gradient term in the liquidus and produce a positive oxygen gradient at the ICB. This provided stable oxygen profiles that form suitable initial states for a time-dependent system. Solutions for the high freezing speed are computed for CSB heat fluxes ranging from 1 and $6\ \mathrm{TW}$. The solution for $1\ \mathrm{TW}$ is rejected since positive values of the solid flux were observed, which is inconsistent with the model of mobility and present-day observations of a stably-stratified F-layer.

Profiles were compared with equivalent solutions computed from the box model for CSB heat flows of $2\ \mathrm{TW}$ and above. Snow speeds determined by the spherical problem are input as a fixed value into the box model. The equivalent latent heat flux released by direct freezing in the spherical model is input as a fixed ICB heat flux in the box model, so that a like-for-like comparison can be made. In general temperatures encountered in the spherical case are higher than those found in the Cartesian case, even though they are both fixed at the same liquidus temperature at the CSB. A similar behaviour is observed with the oxygen concentrations, where the spherical model yields lower values than the box model. These effects combine to give a greater density jump in the

spherical model compared with the box model, and a desirable density stratification that exceeds the PREM density is observed for high enough CSB heat flows. Solid flux curves behave more linearly compared to the Cartesian case, where profiles of the solid flux are almost the same in both cases when the snow speed is lowest, and then increasingly deviate from each other as the snow speed increases.

A greater layer thickness of $300\ \mathrm{km}$ is explored and compared with the equivalent system in a Cartesian geometry. Oxygen profiles remain stable for a high freezing speed, though their gradients vary more within the layer to create a prominent "S" shaped curve as the CSB heat flow increases. Deviations in the solid flux solutions obtained in the box model become more prominent as the CSB heat flow increases, even when the imposed values at the ICB and CSB are exactly the same. Solutions for the oxygen concentration in a thinner layer contain a more stable gradient, therefore we continue the analysis using a layer thickness of $150\ \mathrm{km}$ to generate a suitable initial condition for the time-dependent model.

We compare the mixing parameter, F, between the spherical and box models for a fixed layer thickness of $150\ \mathrm{km}$. It was generally found that values in the box model are much higher compared with the spherical solutions, which is reflected in the steeper behaviour of the solid flux as it approaches zero at the CSB where barodiffusion is enhanced in the mixing layer. The heat flow through the core containing a slurry layer $150\ \mathrm{km}$ thick, with a high freezing speed and a moderate snow speed of $v_s = 1.8 \times 10^{-11}\ \mathrm{ms}^{-1}$, is evaluated. The total heat flow in the spherical case is $13.9\ \mathrm{TW}$, where the CSB heat flux is fixed at $5.0\ \mathrm{TW}$. The secular cooling in the liquid outer core is similar in the box model and the spherical model. The major difference stems from the difference in gravitational power as oxygen concentration gradients in the spherical case are significantly greater.

Some of the steady state results obtained in this chapter are able to explain the

present day observations of the F-layer and form a starting point for the time-dependent model developed in the next chapter. We have obtained solutions with a stable oxygen profile and a sufficient density stratification that are consistent with present-day observations of the F-layer. This provides a suitable initial state that can be used to initialise the time-dependent system.

Chapter 5

A time-dependent slurry

Contents

The steady-state models demonstrate that the modern day F-layer can be explained by a slurry that produces stably-stratified layers. In order to understand the possible origin and evolution of the F-layer over time, we develop a one-dimensional, time-dependent slurry system in this chapter. More sophisticated boundary conditions are developed so that the slurry volume is coupled to the thermal evolution of the liquid outer core and solid inner core. A solution from the steady-state problem is used to generate a suitable initial condition for the time-dependent model. Numerical testing is performed to verify that reliable solutions are produced. We examine a couple of test case solutions and present a discussion of the results.

A schematic of the time-dependent model and its boundary conditions is given in Figure 5.1.

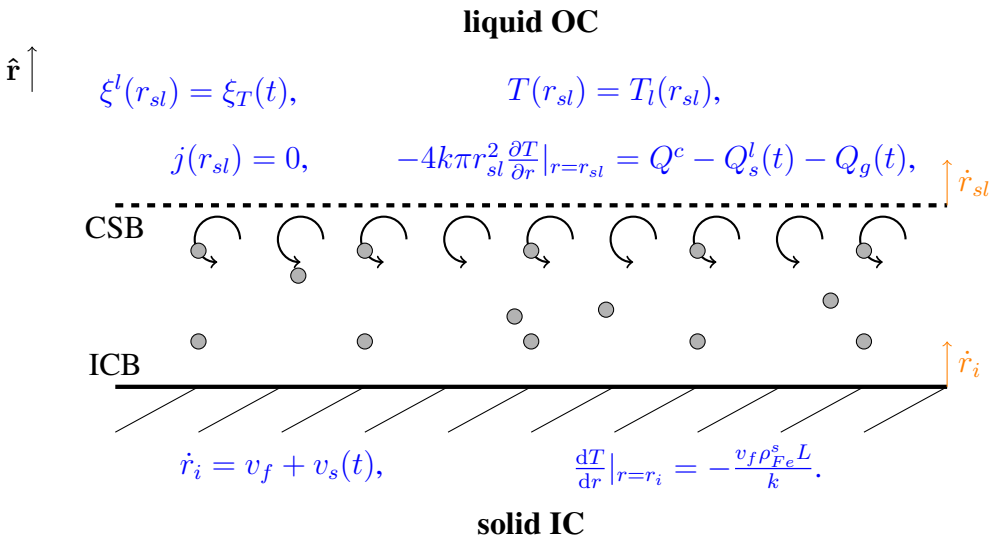

Figure 5.1: A schematic of the boundary conditions imposed on the time-dependent slurry problem.

5.1 Time-dependent equations

Recall that the governing time-dependent, static, slurry equations in spherical coordinates (see 4.1.2, 4.1.5 and 4.1.7) are

$$\frac{\mathrm{D}T}{\mathrm{D}t} = \kappa\frac{\partial^2 T}{\partial r^2} + \frac{2\kappa}{r}\frac{\partial T}{\partial r} + \frac{L}{\rho^l_{Fe}c_p}\frac{\partial j_r}{\partial r} + \frac{2L}{r\rho^l_{Fe}c_p}j, \tag{5.1.1a}$$

$$\rho^l_{Fe}\frac{\mathrm{D}\xi}{\mathrm{D}t} = K_4\left[\frac{\bar{D}}{T^2}\frac{\partial T}{\partial r} - \frac{1}{T}\frac{\partial \bar{D}}{\partial r} - \frac{2}{r}\frac{\bar{D}}{T}\right] + \left(\xi^l\frac{\partial j_r}{\partial r} + j_r\frac{\partial \xi^l}{\partial r} + \frac{2}{r}\xi^l j_r\right) \tag{5.1.1b}$$

$$\frac{\partial T}{\partial r} = -g(r)K_1 T - K_2 T^2\frac{\partial \xi^l}{\partial r}, \tag{5.1.1c}$$

where

$$\bar{D} = D_O \exp\left(\frac{F(r-r_i)}{d}\right), \tag{5.1.2}$$

is the enhanced self-diffusion coefficient.

Note that for the time-dependent problem, both the ICB and CSB boundaries can move at different speeds as the layer thickness is no longer assumed to be fixed. We formulate the equations in the rest frame so that we no longer use the coordinate transforms (3.1.1) in the box model, and (4.2.1) in the spherical model. Instead we transform into a moving frame as outlined in Section 5.3 below.

5.2 Boundary conditions

In the time-dependent model the layer thickness is no longer fixed, so that the locations of the ICB and CSB are able to independently change over time as the inner core grows. Therefore some physical properties, such as gravity, become dependent on radius rather than taken as constant as in the previous steady-state models. The slurry ODEs form a fourth order system, solved subject to six boundary conditions. In the steady case, there are two boundary conditions on the heat flux at the ICB and CSB,

one boundary condition on the light element concentration at the CSB, one boundary condition on the temperature at the CSB and one boundary condition on the solid flux at the CSB. A slightly different boundary condition is used to constrain the position of the moving ICB instead of (but similar to) the solid flux condition on the ICB as before.

The time-dependent global heat balance of the core with no rotation and no magnetic field is given by

$$-4k\pi r_{sl}^2 \frac{\partial T}{\partial r} = Q^c - Q^l(t) - Q_g(t) \qquad \text{at } r = r_{sl}(t), \tag{5.2.1}$$

where the LHS is the heat flux out of the slurry, Q^c is the CMB heat flux, which is prescribed and assumed fixed over time, $Q_s^l(t)$ is the secular cooling of the liquid outer core (OC) volume, which changes over time as the core cools, and $Q_g(t)$ is the gravitational power, which changes over time as the liquid volume decreases. To calculate the secular cooling of the OC, the adiabatic temperature in the OC must be computed.

To calculate the adiabat, the position of the CSB, $r_{sl}(t)$, must be determined. In the steady-state model the layer thickness is fixed so that the liquidus data provided by *ab initio* calculations is evaluated at a fixed CSB radius to yield its temperature

$$T(r_{sl}) = T_l(r_{sl}). \tag{5.2.2}$$

In the time-dependent model this process is reversed, so that the temperature is freely calculated by the time-dependent system which is used to pinpoint the CSB location using the melting data. The CSB speed is then defined by

$$\dot{r}_{sl} = \frac{\Delta r_{sl}}{\Delta t}, \tag{5.2.3}$$

where Δr_{sl} is the change in CSB radius after timestep Δt.

Once $T(r_{sl})$ is determined, an adiabat, T_a, can be constructed from the CSB to the CMB, which then determines the CMB temperature, T_c, so that the core cooling rate can be computed by

$$\frac{\mathrm{d}T_c}{\mathrm{d}t} = \frac{\Delta T_c}{\Delta t}, \tag{5.2.4}$$

where ΔT_c is the change in CMB temperature after timestep Δt. The adiabat is given by

$$T_a(r,t) = T_{csb}(t) \exp\left(- \int_{r_{sl}(t)}^{r} \frac{g\gamma}{\phi} \, \mathrm{d}r \right), \tag{5.2.5}$$

where γ is Grüneisen's parameter and ϕ is the seismic parameter. Grüneisen's parameter quantifies the thermoelastic properties of core material (Vocadlo *et al.*, 2000), and the seismic parameter is given by $\phi = v_p^2$ in the liquid core, in which v_p is the P wave velocity taken from PREM. The adiabat (5.2.5) is used to calculate the secular cooling of the OC volume, given by

$$Q_s^l(t) = - \int_{r_{sl}}^{r_c} 4\pi r^2 \rho c_p \frac{\partial T_a}{\partial t} \, \mathrm{d}r, \tag{5.2.6}$$

where $\frac{\partial T_a}{\partial t}$ is the change in adiabatic temperature over time. Note that compared with the corresponding calculation (3.3.10) in the steady-state, the cooling rate is no longer fixed because this becomes a consistent quantity (5.2.4) within a time-dependent framework now that the adiabatic temperature varies with time.

Gravitational energy, $Q_g(t)$, is liberated when light element from the slurry moves into the convecting liquid outer core and releases heat, which enters into the global energy balance (5.2.1). This is given by

$$Q_g = \int_V \rho \mathbf{u} \cdot \nabla \psi \, \mathrm{d}V, \tag{5.2.7}$$

originally defined in (2.10.16). An equivalent time-dependent expression is given by

$$Q_g(t) = \dot{r}_{sl} \int_{r_{sl}+\delta r}^{r_c} \frac{9 M_O r_{sl}^2}{\left(r_c^3 - r_{sl}^3\right)^2} g(r) r^3 \, \mathrm{d}r, \tag{5.2.8}$$

derived in Appendix A, where M_O is the fixed mass of oxygen contained in the OC. This expression makes use of the CSB speed, $\dot{r}_{sl}$, and accounts for the radially dependent gravitational acceleration, $g(r)$.

The concentration of light element at the CSB, ξ_T, is no longer held constant at 8 mol.%, since the liquid outer core volume is decreasing over time while the inner core and slurry volume grows. Hence $\xi_T \equiv \xi_T(t)$ is time-dependent and is determined by

$$\xi_T(t) = \frac{M_O}{M^l(t)} \qquad \text{at } r = r_{sl}(t), \tag{5.2.9}$$

where M_O is the total oxygen mass, which is fixed throughout time since it cannot be destroyed or created within the core and we assume that oxygen cannot be exchanged with the mantle. The mass of the liquid outer core, $M^l(t)$, shrinks over time as a function of the growing inner core and slurry volume, which is given by

$$M^l(t) = M_{core} - M^s(t) - M^{sl}(t), \tag{5.2.10}$$

where $M_{core} = 1.84 \times 10^{24}$ kg (Dziewonski & Anderson, 1981), $M^s(t) \simeq \rho_{Fe}^s \frac{4\pi r_i^3}{3}$ and $M^{sl}(t) \simeq \frac{4\pi}{3} \rho_{Fe}^l \left(r_{sl}^3 - r_i^3\right)$. For the sake of simplicity we assume that the IC density is constant since it varies by less than 2.6% according to PREM, and that the density across the slurry is close to the reference density, ρ_{Fe}^l.

Instead of a condition on the solid flux at the ICB given by (4.2.7) in the steady-state spherical model, this is replaced by an equivalent condition on the ICB speed

itself given by

$$\dot{r}_i = v_f + v_s(t), \tag{5.2.11}$$

where the snow speed, $v_s(t) = j(r_i, t)/\rho^s_{Fe}$ is similar to (4.2.7) and is free to be determined and the freezing speed, v_f, is prescribed and assumed constant.

For completeness, the solid flux condition on the CSB (4.2.7),

$$j_r(r_{sl}, t) = 0 \tag{5.2.12}$$

and the condition on the ICB heat flux (4.2.3)

$$\left.\frac{\mathrm{d}T}{\mathrm{d}r}\right|_{r=r_i} = -\frac{v_f \rho^s_{Fe} L}{k} \tag{5.2.13}$$

remain the same as in the steady-state spherical case.

5.3 Landau transform

If we consider the problem in the rest frame, then it is numerically difficult to resolve a slurry with two moving boundaries at $r_i(t)$ and $r_{sl}(t)$, since variables would need to be interpolated as the mesh changes with each timestep. We take an alternative approach and perform a Landau transform. This is a common method implemented in Stefan problems, which are a class of moving boundary problems that involve phase change (Alexiades, 1992). In our model of the core, each interface is treated as an infinitesimally thin surface where the ICB separates the inner core from the slurry and the CSB separates the slurry from the outer core. We perform a Landau transform

$$x = \frac{r - r_i(t)}{r_{sl}(t) - r_i(t)}, \qquad t = t' \tag{5.3.1}$$

so that the ICB, $r = r_i(t)$, maps to $x = 0$ and the CSB, $r = r_{sl}(t)$, maps to $x = 1$ at each timestep. There is no change in the transform of the time coordinate. The Landau transform means that the partial derivative for an arbitrary variable a with respect to time in the x coordinate system is

$$\begin{aligned}\frac{\partial a}{\partial t} &= \frac{\partial a}{\partial t'}\frac{\partial t'}{\partial t} + \frac{\partial a}{\partial x}\frac{\partial x}{\partial t} \\ &= \frac{\partial a}{\partial t'} - \frac{\partial a}{\partial x}\cdot\frac{x\dot{r}_{sl} + (1-x)\dot{r}_i}{r_{sl} - r_i},\end{aligned} \tag{5.3.2}$$

where $\dot{r}_i = \partial r_i/\partial t$, $\dot{r}_{sl} = \partial r_{sl}/\partial t$. The partial derivative with respect to r becomes

$$\begin{aligned}\frac{\partial a}{\partial r} &= \frac{\partial a}{\partial t'}\frac{\partial t'}{\partial r} + \frac{\partial a}{\partial x}\frac{\partial x}{\partial r} \\ &= \frac{1}{r_{sl} - r_i}\frac{\partial a}{\partial x},\end{aligned} \tag{5.3.3}$$

and the second derivative is

$$\frac{\partial^2 a}{\partial r^2} = \frac{\partial}{\partial r}\left(\frac{\partial a}{\partial r}\right) = \frac{1}{(r_{sl} - r_i)^2}\frac{\partial^2 a}{\partial x^2}. \tag{5.3.4}$$

This transform is a generalisation of the Gubbins *et al.* (2008) transform employed in Chapters 3 and 4 when a fixed layer depth was assumed.

After performing a Landau transform, and assuming that the slurry is static, then the temperature equation (5.1.1a) becomes

$$\begin{aligned}\frac{\partial T}{\partial t} - \frac{x\dot{r}_{sl} + (1-x)\dot{r}_i}{r_{sl} - r_i}\frac{\partial T}{\partial x} \\ = \frac{\kappa}{(r_{sl} - r_i)^2}\frac{\partial^2 T}{\partial x^2} + \frac{\kappa}{(r_{sl} - r_i)}\frac{2}{r_i + x(r_i - r_{sl})}\frac{\partial T}{\partial x} \\ + \frac{L}{\rho^l_{Fe} c_p (r_{sl} - r_i)}\frac{\partial j_r}{\partial x} + \frac{2Lj_r}{\rho^l_{Fe} c_p [r_i + x(r_{sl} - r_i)]},\end{aligned} \tag{5.3.5}$$

the light element equation (5.1.1b) becomes

$$\frac{\partial \xi^l}{\partial t} - \frac{x\dot{r_{sl}} + (1-x)\dot{r_i}}{r_{sl} - r_i}\frac{\partial \xi^l}{\partial x} = \frac{K_4}{\rho^l_{Fe}}\left\{\frac{\bar{D}}{(r_{sl}-r_i)\,T^2}\frac{\partial T}{\partial x} - \frac{F\bar{D}}{(r_{sl}-r_i)\,T} - \frac{2}{[r_i + x(r_{sl}-r_i)]}\frac{\bar{D}}{T}\right\} + \frac{1}{\rho^l_{Fe}}\left\{\frac{\xi^l}{r_{sl}-r_i}\frac{\partial j_r}{\partial x} + \frac{j_r}{r_{sl}-r_i}\frac{\partial \xi^l}{\partial x} + \frac{2}{[r_i + x(r_{sl}-r_i)]}\xi^l j_r\right\}, \quad (5.3.6)$$

and the liquidus (5.1.1c) becomes

$$\frac{1}{r_{sl}-r_i}\frac{\partial T}{\partial x} = -g(r)K_1 T - \frac{K_2 T^2}{r_{sl}-r_i}\frac{\partial \xi^l}{\partial x}. \quad (5.3.7)$$

5.4 Numerics

We define a regularly spaced mesh for $x \in [0,1]$ by

$$x_m = \frac{m-1}{n_x} \qquad \text{for } m = 1, ..., n_x + 1,$$

with the total number of gridpoints n_x defining the numerical resolution, and a spatial step size of $\Delta x = 1/n_x$. A time mesh is defined by

$$t_n = \frac{n-1}{n_t} \qquad \text{for } n = 1, ..., n_t + 1,$$

where n_t is the total number of points in time and the timestep is given by $\Delta t = 1/n_t$. We solve equations (5.3.5)-(5.3.7) implicitly using the Crank-Nicolson scheme. The Crank-Nicolson method samples the ODE at time $t = t_{n+\frac{1}{2}}$ that is second order in time and unconditionally stable (Morton & Mayers, 2005). The scheme is a combination of the forward Euler method at n, which utilises three points, and a backward Euler

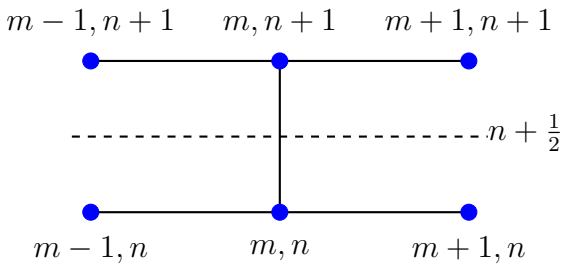

Figure 5.2: A stencil of the Crank-Nicolson scheme applied to a one-dimensional problem.

method at $n+1$, which also utilises three points. Figure 5.2 shows a stencil for the Crank-Nicolson scheme applied to a one-dimensional problem, which utilises all six points. The θ rule is implemented so that the explicit forward and implicit backward schemes can be weighted to either improve accuracy or stability, with $\theta \in [0,1]$. The usual value of θ for the Crank-Nicolson method is 0.5, which gives a second-order accuracy. If $\theta = 0$, then the scheme becomes a less numerically stable explicit forward Euler method, whereas if $\theta = 1$, then the scheme becomes an implicit backward Euler method with improved numerical stability. We write $\xi^l \to \xi$ and $j_r \to j$ henceforth so that indices m and n can be used.

We denote the finite difference approximations by

$$u_m^{n+\theta} = \theta u_m^{n+1} + (1-\theta)\, u_m^n \tag{5.4.1a}$$

$$D_t u_m^{n+\theta} = \frac{u_m^{n+1} - u_m^n}{\Delta t} \tag{5.4.1b}$$

$$D_x u_m^{n+\theta} = \theta \left(\frac{u_{m+1}^{n+1} - u_{m-1}^{n+1}}{2\Delta x} \right) + (1-\theta) \left(\frac{u_{m+1}^{n} - u_{m-1}^{n}}{2\Delta x} \right) \tag{5.4.1c}$$

$$D_x^2 u_m^{n+\theta} = \theta \left(\frac{u_{m+1}^{n+1} - 2u_m^{n+1} + u_{m-1}^{n+1}}{\Delta x^2} \right) + (1-\theta) \left(\frac{u_{m+1}^{n} - 2u_m^{n} + u_{m-1}^{n}}{\Delta x^2} \right) \tag{5.4.1d}$$

where u_m^n is a numerical approximation at mesh point x_m and timestep t_n of an arbitrary function, u, such as the temperature, T, oxygen concentration, ξ, or the solid flux,

j. Thus the temperature equation (5.3.5) becomes

$$D_t T_m^{n+\theta} - \left(\frac{x_m D_t r_{sl}^{n+\theta} + (1-x_m) D_t r_i^{n+\theta}}{r_{sl}^{n+\theta} - r_i^{n+\theta}} \right) D_x T_m^{n+\theta}$$
$$= \frac{\kappa}{\left(r_{sl}^{n+\theta} - r_i^{n+\theta}\right)^2} D_x^2 T_m^{n+\theta} + \frac{2\kappa}{\left(r_{sl}^{n+\theta} - r_i^{n+\theta}\right)\left[r_i^{n+\theta} + x_m\left(r_{sl}^{n+\theta} - r_i^{n+\theta}\right)\right]} D_x T_m^{n+\theta}$$
$$+ \frac{L}{\rho_{Fe}^l c_p \left(r_{sl}^{n+\theta} - r_i^{n+\theta}\right)} D_x j_m^{n+\theta} + \frac{2L j_m^{n+\theta}}{\rho_{Fe}^l c_p \left(r_i^{n+\theta} + x_m\left(r_{sl}^{n+\theta} - r_i^{n+\theta}\right)\right)}$$

for $2 \le m \le n_x$ (5.4.2)

the light element equation (5.3.6) becomes

$$D_t \xi_m^{n+\theta} - \left(\frac{x_m D_t r_{sl}^{n+\theta} + (1-x_m) D_t r_i^{n+\theta}}{r_{sl}^{n+\theta} - r_i^{n+\theta}} \right) D_x \xi_m^{n+\theta}$$
$$= \frac{K_4}{\rho_{Fe}^l} \left\{ \frac{F \bar{D}_m}{\left(r_{sl}^{n+\theta} - r_i^{n+\theta}\right)\left(T_m^{n+\theta}\right)^2} D_x T_m^{n+\theta} - \frac{F \bar{D}_m}{\left(r_{sl}^{n+\theta} - r_i^{n+\theta}\right) T_m^{n+\theta}} \right.$$
$$\left. - \frac{2\bar{D}_m}{\left(r_i^{n+\theta} + x_m\left(r_{sl}^{n+\theta} - r_i^{n+\theta}\right)\right) T_m^{n+\theta}} \right\} + \frac{1}{\rho_{Fe}^l} \left\{ \frac{\xi_m^{n+\theta}}{\left(r_{sl}^{n+\theta} - r_i^{n+\theta}\right)} D_x j_m^{n+\theta} \right.$$
$$\left. + \frac{j_m^{n+\theta}}{\left(r_{sl}^{n+\theta} - r_i^{n+\theta}\right)} D_x \xi_m^{n+\theta} + \frac{2}{\left(r_i^{n+\theta} + x_m\left(r_{sl}^{n+\theta} - r_i^{n+\theta}\right)\right)} \xi_m^{n+\theta} j_m^{n+\theta} \right\}$$

for $1 \le m \le n_x$ (5.4.3)

and the liquidus (5.3.7) becomes

$$\frac{1}{\left(r_{sl}^{n+\theta} - r_i^{n+\theta}\right)} D_x T_m^{n+\theta} = -g_m^{n+\theta} K_1 T_m^{n+\theta} - \frac{K_2 \left(T_m^{n+\theta}\right)^2}{\left(r_{sl}^{n+\theta} - r_i^{n+\theta}\right)} D_x \xi_m^{n+\theta}$$

for $1 \le m \le n_x$ (5.4.4)

where

$$\bar{D}_m = D_O \exp\left(F x_m\right) \tag{5.4.5}$$

is the enhanced self-diffusion coefficient of oxygen at mesh point x_m, and the gravitational acceleration is given by

$$g_m^{n+\theta} \approx g(r_m, t^{n+\theta}), \tag{5.4.6}$$

in which $g(r_m, t^{n+\theta})$ is given by a polynomial fit to the PREM data (Dziewonski & Anderson, 1981).

The temperature equation is second order and parabolic. Therefore (5.4.2) is solved at the interior mesh points $x_2, ..., x_{n_x}$, which gives $n-1$ algebraic equations to solve for the temperature. At endpoints x_1 and x_{n_x+1}, the boundary conditions (5.2.1) and (5.2.13) are imposed. The three-point endpoint finite difference formulae required to implement these conditions are given by

$$D_x^+ u_1^{n+\theta} = \theta\left(\frac{-3u_1^{n+1} + 4u_2^{n+1} - u_3^{n+1}}{2\Delta x}\right) + (1-\theta)\left(\frac{-3u_1^{n} + 4u_2^{n} - u_3^{n}}{2\Delta x}\right) \tag{5.4.7a}$$

$$D_x^- u_{n_x+1}^{n+\theta} = \theta\left(\frac{u_{n_x-1}^{n+1} - 4u_{n_x}^{n+1} + 3u_{n_x+1}^{n+1}}{2\Delta x}\right) + (1-\theta)\left(\frac{u_{n_x-1}^{n} - 4u_{n_x}^{n} + 3u_{n_x+1}^{n}}{2\Delta x}\right) \tag{5.4.7b}$$

so that the condition on the ICB temperature gradient becomes

$$\frac{1}{\left(r_{sl}^{n+\theta} - r_i^{n+\theta}\right)} D_x^+ T_1^{n+\theta} = -\frac{v_f \rho_{Fe}^s L}{k} \tag{5.4.8}$$

and the condition on the CSB heat flux is

$$-\frac{4k\pi\left(r_{sl}^{n+\theta}\right)^2}{\left(r_{sl}^{n+\theta}-r_i^{n+\theta}\right)}D_x^- T_{n_x+1}^{n+\theta}=Q_c-Q_s^l(t^{n+\theta})-Q_g(t^{n+\theta}) \tag{5.4.9}$$

where

$$Q_s^l(t^{n+\theta})=\int_{r_{sl}^{n+\theta}}^{r_o}4\pi r^2\rho c_p D_t T_a^{n+\theta}\,\mathrm{d}r \tag{5.4.10}$$

$$Q_g(t^{n+\theta})=D_t r_{sl}^{n+\theta}\int_{r_{sl}^{n+\theta}}^{r_o}\frac{9M_O\left(r_{sl}^{n+\theta}\right)^2}{\left(r_o^3-\left(r_{sl}^{n+\theta}\right)^3\right)^2}g_m^{n+\theta}(r_m^{n+\theta})^3\,\mathrm{d}r, \tag{5.4.11}$$

in which Simpson's rule is used to perform the integration over the radius of the liquid outer core.

We solve n_x equations in (5.4.3) to determine the solid flux, j, at each timestep. At the mesh point x_{n_x+1}, we impose the condition

$$j_{n_x+1}^{n+\theta}=0, \tag{5.4.12}$$

which ensures that the solid flux at the CSB is zero.

We solve n_x equations in (5.4.4) to obtain the light element concentration, ξ. At mesh point x_{n_x+1}, we impose the condition

$$\xi_{n_x+1}^{n+\theta}=\xi_T(t^{n+\theta}), \tag{5.4.13}$$

where ξ_T is defined by (5.2.9).

The ICB position, r_i, is numerically determined by

$$D_t r_i^{n+\theta} = v_f - \frac{j_1^{n+\theta}}{\rho_{Fe}^s} \tag{5.4.14}$$

where the freezing speed, v_f, is assumed to be constant. The CSB position, r_{sl} is given by

$$T_{n_x+1}^{n+\theta} = T_l(r_{sl}, t^{n+\theta}), \tag{5.4.15}$$

where the temperature at the CSB is freely determined by the system and the liquidus data (4.2.6) is used to find the CSB position.

In total there are $3n_x + 5$ equations to be solved for $3n_x + 5$ unknowns that form a tridiagonal linear system

$$\mathbf{A}\mathbf{y} = \mathbf{y_0}.$$

We use a MATLAB iterative nonlinear solver `fsolve` to solve this system of equations to advance in time, where $\mathbf{A}$ is a $(3n_x+5)\times(3n_x+5)$ matrix, $\mathbf{y}$ are the variables to be determined at the weighted timestep $\theta t^{n+1} + (1-\theta)t^n$, and $\mathbf{y_0}$ are the known variables at the previous timestep. Vectors $\mathbf{y}$ and $\mathbf{y_0}$ are populated by a linear index of the variables T, ξ, j, r_i and r_{sl}, and the equations are re-written in implicit form so that the residual equations can be minimised by the solver.

5.5 Initialisation

We initialise the time-dependent system using a solution from the spherical steady-state problem in Chapter 4. An initial guess, $\mathbf{y_0}$, is provided to the time-dependent system using the selected parameters in Table 5.1. This solution is chosen because the oxygen profile is stable everywhere in the layer with a sufficient density stratification, and the calculated CMB heat flow is moderate (see Figure 4.3). The mixing parameter,

d (km)	Q^{sl}(TW)	Q^c (TW)	v_f (ms^{-1})	F
150	4	13.9	11.2×10^{-12}	2.08

Table 5.1: Selected input parameters used in the initial state.

F, that is provided is fixed throughout time. The CMB heat flux is calculated according to the global heat balance (5.2.1), and then assumed to be constant throughout the time-dependent simulation. Though the initial solution is in a steady-state, there is an underlying time dependence of the moving ICB due the growing inner core given by v in the coordinate transform (4.2.1). We choose a small timestep of $\Delta t = 10^{-6}$ Ga to calculate the secular cooling, Q_s, and the gravitational power, Q_g, according to equations (5.2.6) and (5.2.8) to determine the CMB heat flow, Q^c that will be prescribed in condition (5.2.1). The same timestep will be used to initialise the time-dependent code before increasing to a larger timestep where data is collected.

5.6 Testing

5.6.1 Initial transient phase

To determine whether the time-dependent code is reliable, we aim to reproduce the steady-state solution using a small time-step. Equivalent boundary conditions from the spherical steady-state problem are imposed on the time-dependent system (see Table 5.2), and the simulation is initialised with the solutions computed using the parameters in Table 5.1. We choose a θ value of 0.6 in the Crank-Nicolson scheme, so that the solution method is slightly more implicit than explicit to enhance numerical stability, while retaining close to second order accuracy. We select a small time-step of $\Delta t = 10^{-6}$ Ga to minimise the time-dependent effects and analyse the initial behaviour of the time-dependent code.

Initial state	Time dependent
$-k\frac{\partial T}{\partial r}\big\vert_{r=r_i} = v_f \rho^s_{Fe} L$	$-k\frac{\partial T}{\partial r}\big\vert_{r=r_i} = v_f \rho^s_{Fe} L$
$-4k\pi r^2_{sl}\frac{\partial T}{\partial r}\big\vert_{r=r_{sl}} = Q^{sl}$	$-4k\pi r^2_{sl}\frac{\partial T}{\partial r}\big\vert_{r=r_{sl}} = Q^c - Q^l(t) - Q_g(t)$
$\xi(r_{sl}) = \xi_T$	$\xi(r_{sl}) = \xi_T(t)$
$j(r_{sl}) = 0$	$j(r_{sl}) = 0$
$j(r_i) = -\rho^s_{Fe} v_s$	$\dot{r}_i = v_f + v_s(t)$
$T(r_{sl}) = T_l(r_{sl})$	$T(r_{sl}) = T_l(r_{sl})$

Table 5.2: A side-by-side comparison of the boundary conditions applied to the initial state, created using the spherical steady-state model of Chapter 4 and the time-dependent problem.

Figure 5.3 shows the time-dependent simulation over the first 5 time-steps There is a very small immediate change in the ICB temperature after the first time-step, but the rest of the solution near the CSB closely follows the initial state thereafter. Similar behaviour is observed for the light element concentration, which is expected because temperature and light element are linked through the liquidus relation. We encounter a transient phase in the solid flux during the initial stages of the simulation, where the value of the solid flux at the ICB oscillates between each time-step. The system takes time to settle down to a numerically stable solution. We deal with the initial transience by running the time-dependent model using a small time-step until a numerically stable state is reached. Data from the initial period is ignored in the interpretation of the final results, and the full time-dependent simulation is run for long enough so that the bias effect from the initial transient phase is negligible. A time series of the snow speed, v_s, for the same simulation is run for a longer total time of 10^{-3} Ga. There is a clear initial transient phase observed in the first 1×10^{-4} Ga of the simulation before the system settles to a more steady value. We therefore ignore results from the first 1×10^{-4} Ga of the simulation, as these reflect deviations from the initial condition and are not

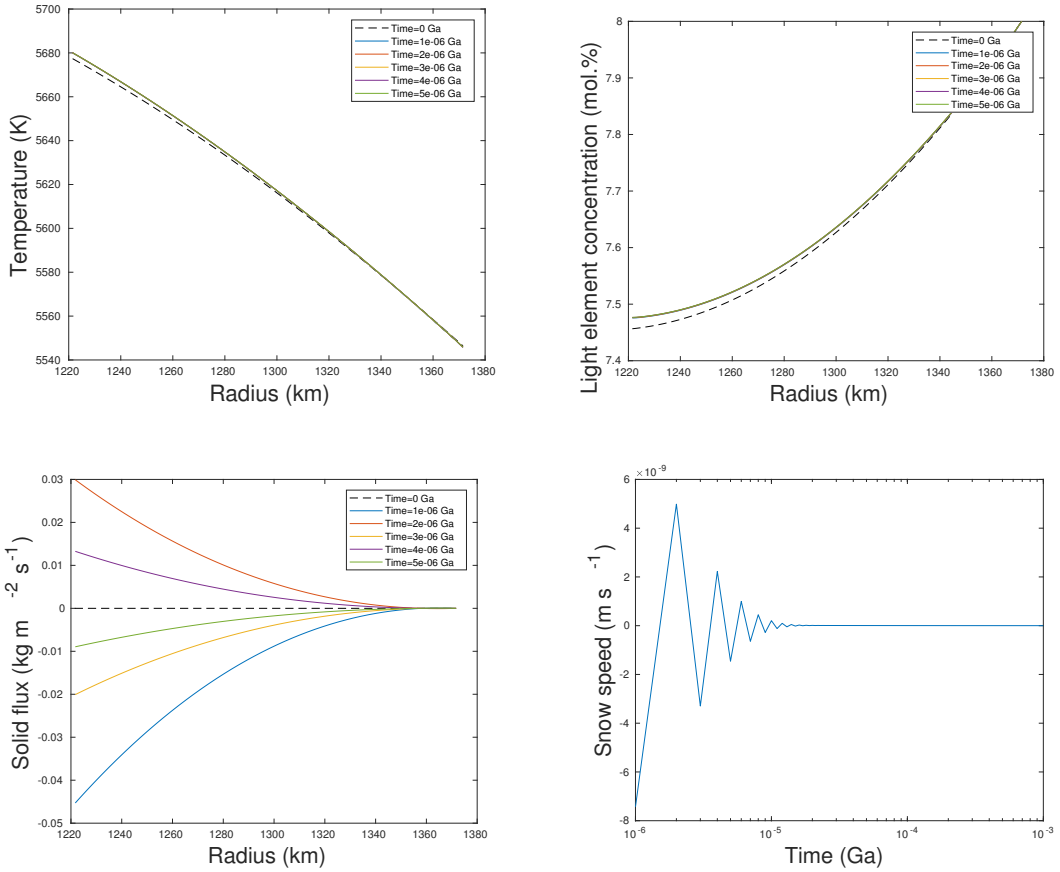

Figure 5.3: Initial stages of the time-dependent simulation over 5 time-steps with $\Delta t = 10^{-6}$ Ga. Initial state (dashed) given by the steady-state solution $d = 150$ km, $Q^{sl} = 4$ TW, $F = 2.08$ and $v_f = 11.2 \times 10^{-12}$ ms^{-1}. (Lower-right) A time series of the snow speed, v_s, over 10^{-3} Ga.

representative of the fundamental dynamics of the slurry system. Figure 5.4 shows the solid flux from the same simulation over a longer time period. This shows the evolution of the solid flux after the initial transient phase has passed and oscillations at the ICB are no longer observed, where $j(r_i)$ smoothly increases over time. We proceed with confidence that the time-dependent scheme is free from initial transient effects after a simulated time of 1×10^{-4} Ga using a small time-step of 10^{-6} Ga.

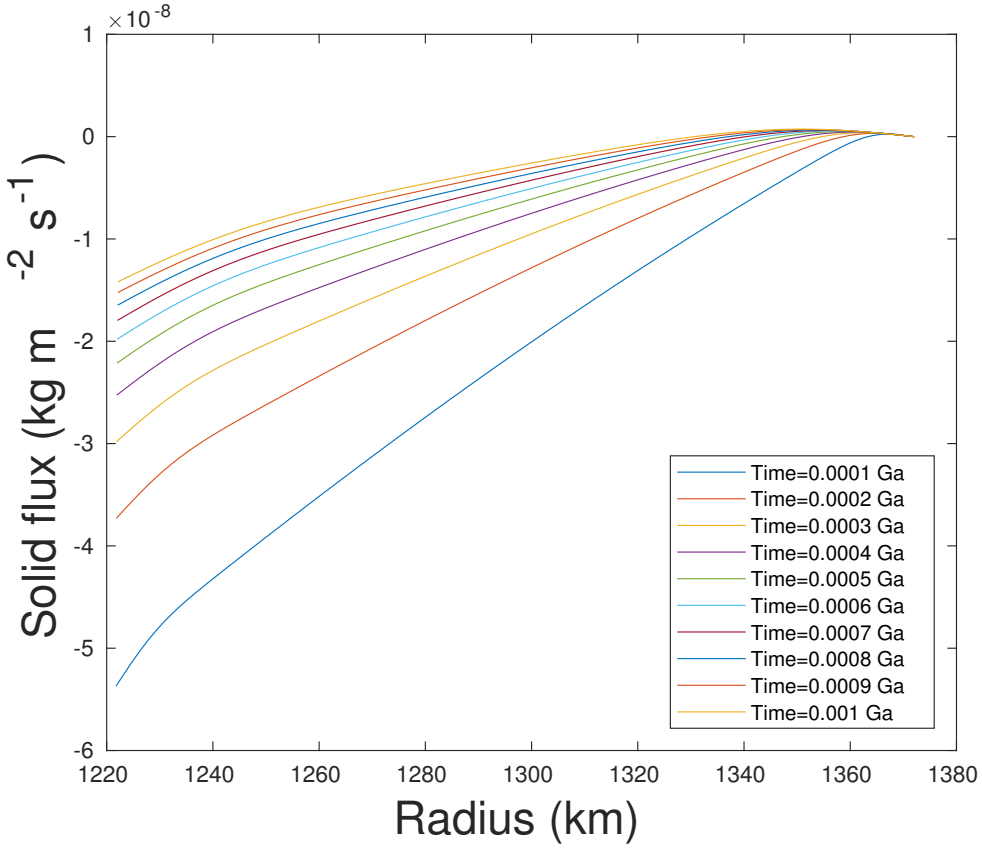

Figure 5.4: Evolution of the solid flux profile after ignoring the initial transient period. Initial state is given by the steady-state solution $d = 150$ km, $Q^{sl} = 4$ TW, $F = 2.08$ and $v_f = 11.2 \times 10^{-12}$ ms^{-1}.

Q^c(TW)	F	v_f (ms^{-1})	n_r	Percent difference
13.9	2.08	11.2×10^{-12}	25	–
13.9	2.08	11.2×10^{-12}	50	0.7000 %
13.9	2.08	11.2×10^{-12}	100	0.0030 %
13.9	2.08	11.2×10^{-12}	200	0.0008%

Table 5.3: Selected input parameters used in resolution test, and the percentage difference in results between each simulation.

5.6.2 Resolution testing

To confirm that the solutions computed by the time-dependent scheme given in Section 5.4 are reliable, the same simulation is performed using different mesh resolutions. A simulation is well-resolved and reliable if the solutions agree with the results of a higher resolution test. A time series of the layer thickness evolution, $d(t)$, is used to compare results, and is performed for every test case to ensure that the results are reliable.

An example of a resolution test is given in Figure 5.5. The numerical resolution is doubled in each simulation until a reliable time series of $d(t)$ is achieved. Table 5.3 shows the input parameters selected for this resolution test. After running the resolution test, we find the maximum percentage difference in the layer thickness, calculated by

$$\max\left(\frac{d_{n_r}(t) - d_{2n_r}(t)}{d_{n_r}(t)}\right) \times 100,$$

For $n_r = 25$ and 50, the difference is less than 0.7%. The percentage difference between the results for $n_r = 50$ and 100 is less than 0.003%. After doubling the resolution to $n_r = 200$ mesh points, there is less than 0.0008% difference compared with $n_r = 100$. We suppose that a difference of less than 0.003% is acceptable, therefore we proceed with confidence that results from this test case using $n_r = 50$ mesh points is reliable.

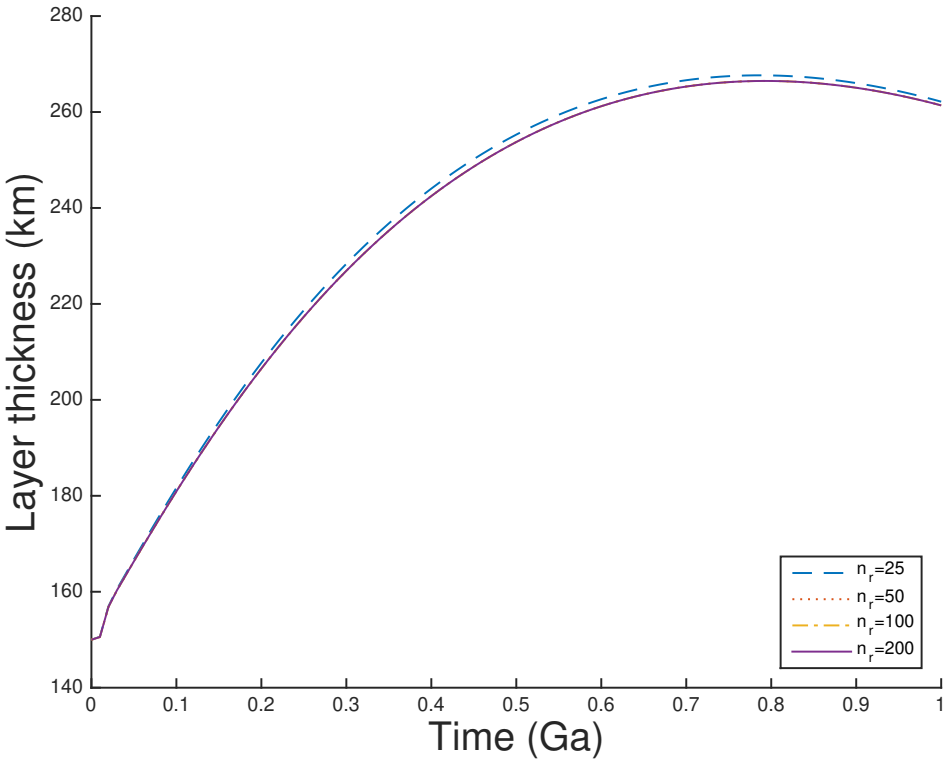

Figure 5.5: A time series of the layer thickness evolution, $d(t)$ for numerical resolution 25, 50, 100 and 200. The percentage difference in results for resolutions 50 and 100 is less than 0.0030%, therefore indicating that the numerical simulations at $n_r = 50$ are reliable for this test case.

5.7 Results and discussion

Input parameters explored include the CMB heat flux, Q^c, mixing parameter, F, and the interfacial freezing rate, v_f. As discussed in the steady-state problem, geophysically plausible estimates of the CMB heat flux lie between 5 and 17 TW (see Table 3.1). The CMB heat flux enters the model via the CSB heat flux condition (5.2.1). The mixing parameter, F, enters the problem in the self-diffusion coefficient, $\bar{D}$ (5.1.2). Currently there is no estimation of what the interfacial freezing speed, v_f, would be according to observations or experiments. The purpose of v_f is to lift the temperature at the ICB onto the liquidus, since we have assumed that the inner core is isothermal. We test values of v_f that correspond with reasonable ICB heat fluxes of 0.5 TW and 2 TW.

Complete solutions of the temperature, oxygen concentration and solid flux simulated over a time of 1 billion years using parameters from the resolution test case described in Table 5.3 are presented in Figure 5.6. The effect of core cooling over time is evident in the decreasing temperatures experienced in the slurry layer, with a decrease of 240 K in the ICB temperature over a billion years. This is fast compared to the calculated core cooling rate of $\frac{\mathrm{d}T_c}{\mathrm{d}t} = -56\ \mathrm{KGa}^{-1}$, which is much smaller than the cooling rate used in steady-state models (see Table 3.1). The temperature gradient at the ICB steepens slightly over time since latent heat release due to interfacial freezing, v_f, scales with the decreasing thermal conductivity across the core. Similarly, the CSB temperature gradient steepens over time as more heat is extracted from the slurry as the core cools. Temperature changes within the layer more or less follows a linear profile.

The evolution of light element concentration within the slurry layer quickly changes from a stable configuration given by the initial state (see Figure 4.3), to an unstable configuration with more light element at the bottom compared with the top of the layer.

As the outer core decreases in volume due to the growing size of the inner core and slurry volume, the concentration of light element in the outer core bulk increases from $7.7\ \mathrm{mol.\%}$ at $t = 0.1\ \mathrm{Ga}$ to $8.8\ \mathrm{mol.\%}$ by $t = 1\ \mathrm{Ga}$. Note that the concentration does not start from the usual value of $8\ \mathrm{mol.\%}$ because of the initial transient phase that has been ignored. The light element concentration at the base of the layer initially increases monotonically over time from a value of $7.9\ \mathrm{mol.\%}$ at time $t = 0.1\ \mathrm{Ga}$ before increasing to $9.5\ \mathrm{mol.\%}$ by $t = 1\ \mathrm{Ga}$.

Profiles of the solid flux in the time-dependent case significantly differ from the profiles presented in Chapter 3. One such feature is that the solid flux behaves more linearly. This is caused in part by the different boundary conditions imposed on the solid flux at the ICB: for the time-dependent case this is free to be determined by the solution whereas in Chapter 3 the solid flux is explicitly related to the inner core growth rate, v_s, which is assumed to be fixed. The solid flux goes to zero at the top of the layer as imposed by the zero solid flux condition at the CSB. The slurry is snowing much harder at the bottom of the layer compared with the top. An increased rate of solidification at the base of the layer leaves more light element in the residual liquid, therefore increasing the oxygen concentration in this region as evidenced by Figure 5.6. Fixing the mixing parameter, F, may have been responsible for this effect, whereas previously in Chapter 3 this was free to be determined and had a higher value (see Figure 4.5). More stable oxygen configurations are attained in the box model since there is a uniform amount of solid produced over the majority of the slurry layer before decreasing sharply to zero at the CSB.

Figure 5.7 shows the ICB and CSB position and speed over time. The ICB starts from a radius of $1262\ \mathrm{km}$ after $0.1\ \mathrm{Ga}$, and then increases to $1663\ \mathrm{km}$ after 1 billion years. The CSB starts from an initial value of $1443\ \mathrm{km}$ and increases to $1924\ \mathrm{km}$ after 1 billion years. From Figure 5.8, it can clearly be seen that the layer thickness under-

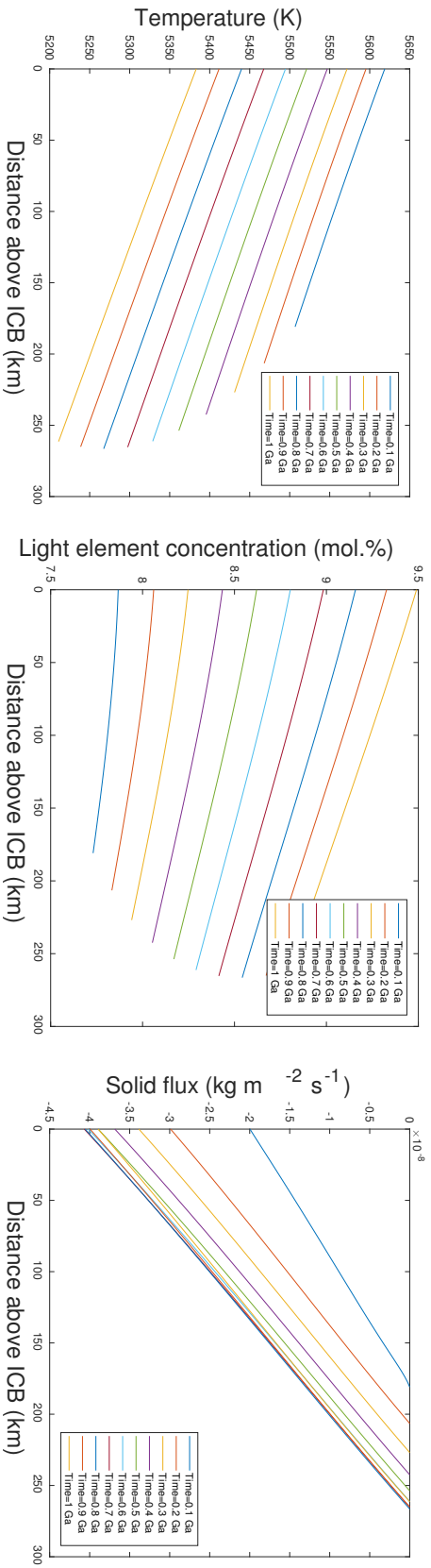

Figure 5.6: Profiles of (left) temperature, (centre) oxygen concentration, (right) solid flux across the slurry layer over 1 billion years. $Q^c = 13.9$ TW, $F = 2.08$ and $v_f = 11.2 \times 10^{-12}$ ms^{-1}.

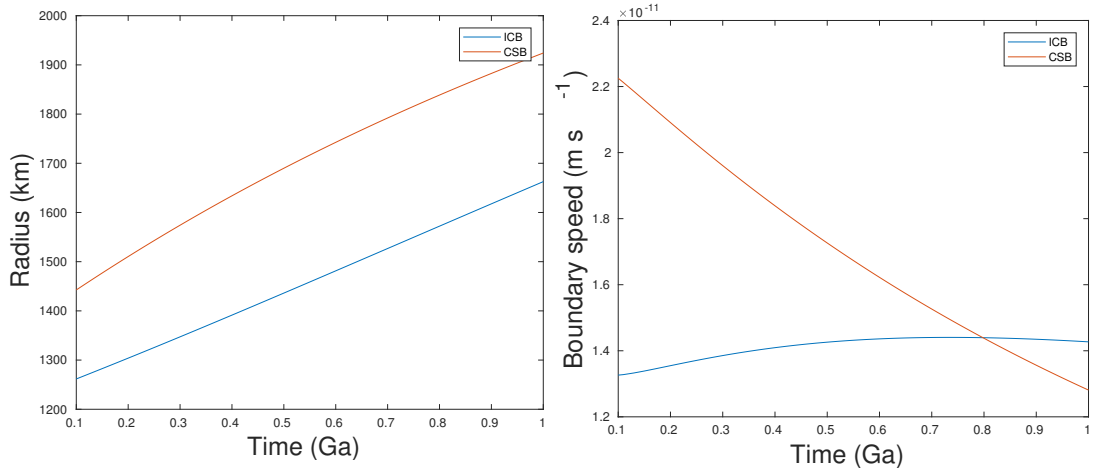

Figure 5.7: ICB and CSB position (left) and speed (right) over 1 billion years. $Q^c = 13.9$ TW, $F = 2.08$ and $v_f = 11.2 \times 10^{-12}$ ms^{-1}.

goes a period of growth before receding at $t = 0.80$ Ga. Relaxing the condition on the layer thickness that was previously fixed at $d = 150$ km allows the layer thickness to rapidly deviate from the initial state. Figure 5.7 shows that the CSB speed continually decreases over time, whereas the ICB speed increases steadily before decelerating at around 0.6 Ga. The boundary speeds concur at $t = 0.80$ Ga, the time at which the layer begins to shrink. Figure 5.8 also shows the evolution of the density profile within the slurry layer. A stably–stratified layer exceeding observations from PREM is barely obtained at $t = 0.1$ Ga and subsequently falls below PREM thereafter. This is primarily a result of the unstable oxygen profiles negatively contributing to the total density.

Evolution of the snow speed can be inferred from the solid flux at the ICB using (4.2.7). The magnitude of v_s is the same order of magnitude as v_f. The sum of v_s and v_f gives $\dot{r}_i \sim 10^{-11}$ ms^{-1}, the ICB speed. From Figure 5.7 it can be seen that the magnitude of $\dot{r}_{sl}$, the CSB speed, is on the order of 10^{-11} ms^{-1} also and continually decelerates. Therefore the balance between $\dot{r}_i$ and $\dot{r}_{sl}$, and hence layer thickness, is partly controlled by v_s and v_f. An increasing amount of snow is produced over time,

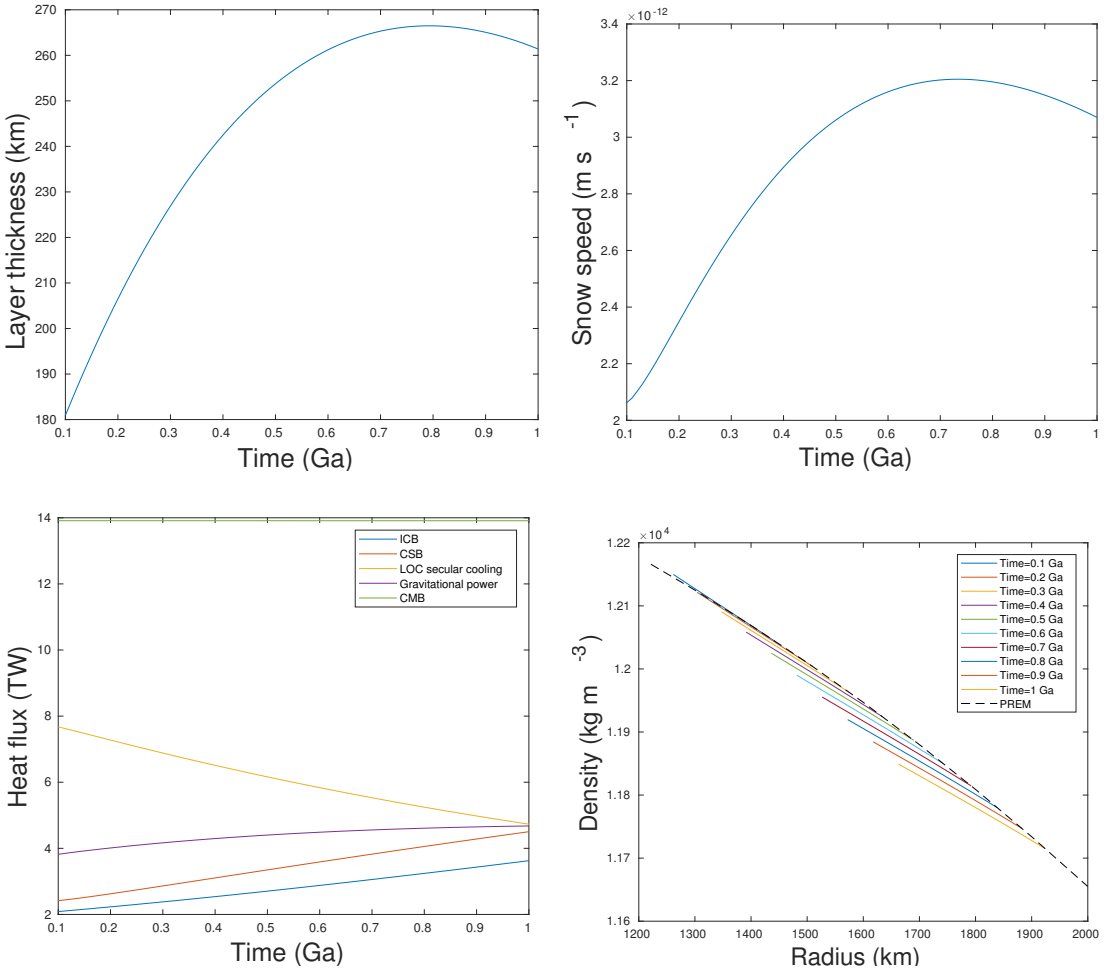

Figure 5.8: (Top left) Slurry layer thickness, (top right) snow speed, (bottom left) components of the core heat flux, (bottom right) density profiles of the slurry layer over 1 billion years. $Q^c = 13.9$ TW, $F = 2.08$ and $v_f = 11.2 \times 10^{-12}$ ms^{-1}.

thereby increasing the rate at which the ICB advances compared with the CSB and so the layer will eventually diminish given enough time.

The CMB heat flux is a parameter assumed to be constant and imposed onto the system that is originally determined by the CSB heat flux selected in the initial state. An initial CSB heat flux of 4 TW corresponds to a CMB heat flux of 13.9 TW after solving the spherical steady-state problem. The rate of heat loss by secular cooling in the liquid outer core decreases from a 7.7 TW to 4.7 TW over the course of the time-dependent simulation. This is balanced by the overall increase in the CSB heat flux and gravitational power over time, with the former increasing from 2.4 TW to 4.5 TW, and the latter increasing from 3.8 TW to 4.7 TW by the end of the simulation. There is a large jump of the CSB heat flux from 4 TW to 2.4 TW during the initial transient phase of the simulation, causing the temperature gradient at the CSB to become more shallow than in the initial state. The increase in CSB heat flux throughout the simulation is predominantly dependent on the geometric increase in CSB radius, r_{sl}, and grows accordingly as the inner core enlarges. Gravitational energy is related to the CSB speed, $\dot{r}_{sl}$ and the CSB radius also. The increasing ICB heat flux is initially set by the freezing speed, v_f, and then mostly scales with the geometric increase of the inner core radius over time.

Figure 5.10 shows the results of the time-dependent code initialised using a steady-state solution with a higher initial CSB heat flow of 6 TW, amounting to a fixed CMB heat flow $Q^c = 21.4$ TW. The freezing speed remains the same at $v_f = 11.2 \times 10^{-12}$ ms^{-1} and the mixing parameter determined by the initial state is $F = 2.58$. Similar behaviour is again observed, where the temperature and solid flux straighten out to a more linear profile while the oxygen concentration quickly becomes unstably stratified. The layer attains a greater thickness since it immediately adjusts from the initialised layer thickness of 150 km to 213 km, and the initial speed at which the

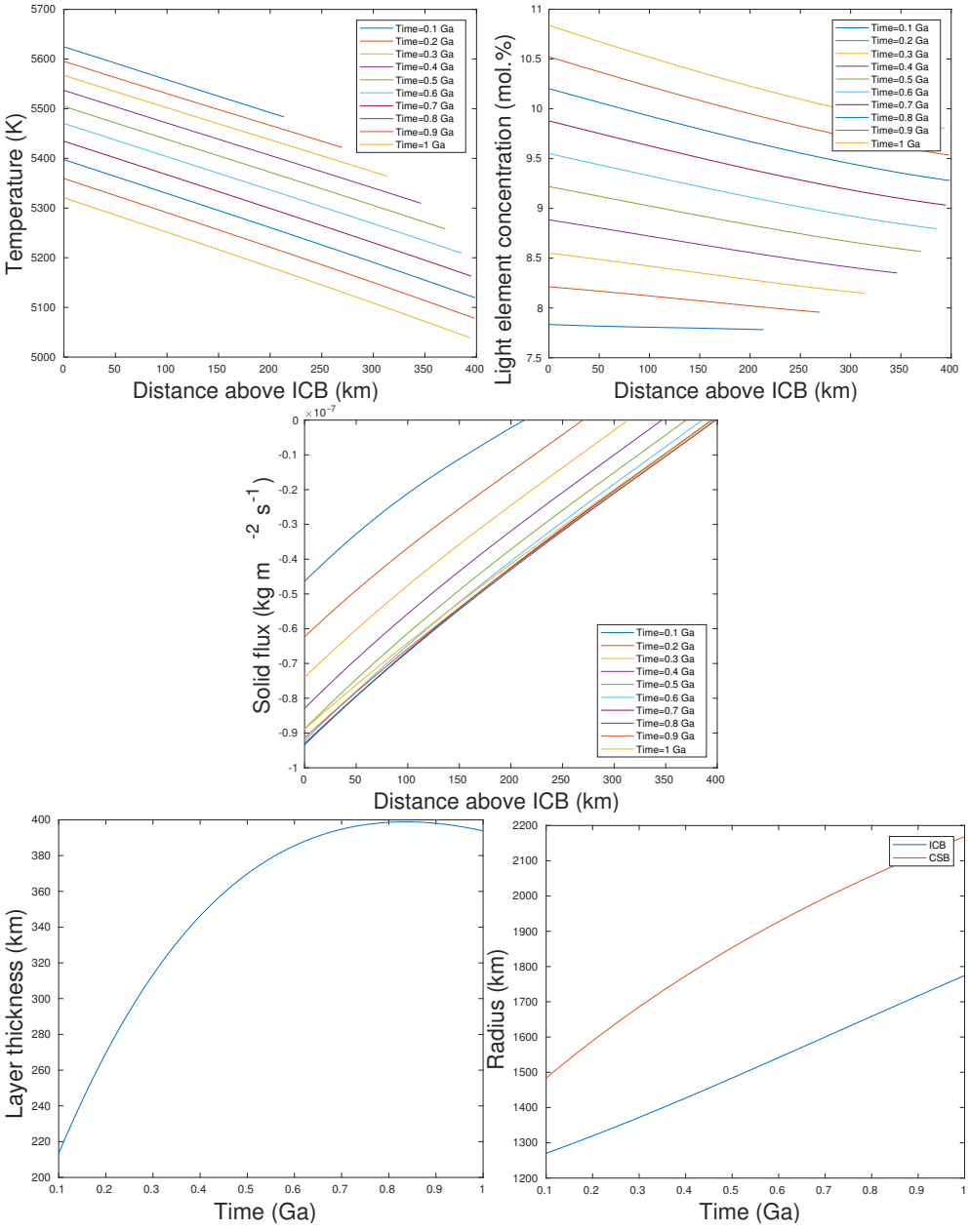
Temperature (K)
Distance above ICB (km)
Time=0.1 Ga
Time=0.2 Ga
Time=0.3 Ga
Time=0.4 Ga
Time=0.5 Ga
Time=0.6 Ga
Time=0.7 Ga
Time=0.8 Ga
Time=0.9 Ga
Time=1 Ga
Light element concentration (mol.%)
Distance above ICB (km)
Solid flux (kg m -2 s -1)
×10-7
Distance above ICB (km)
Layer thickness (km)
Time (Ga)
Radius (km)
ICB
CSB
Time (Ga)

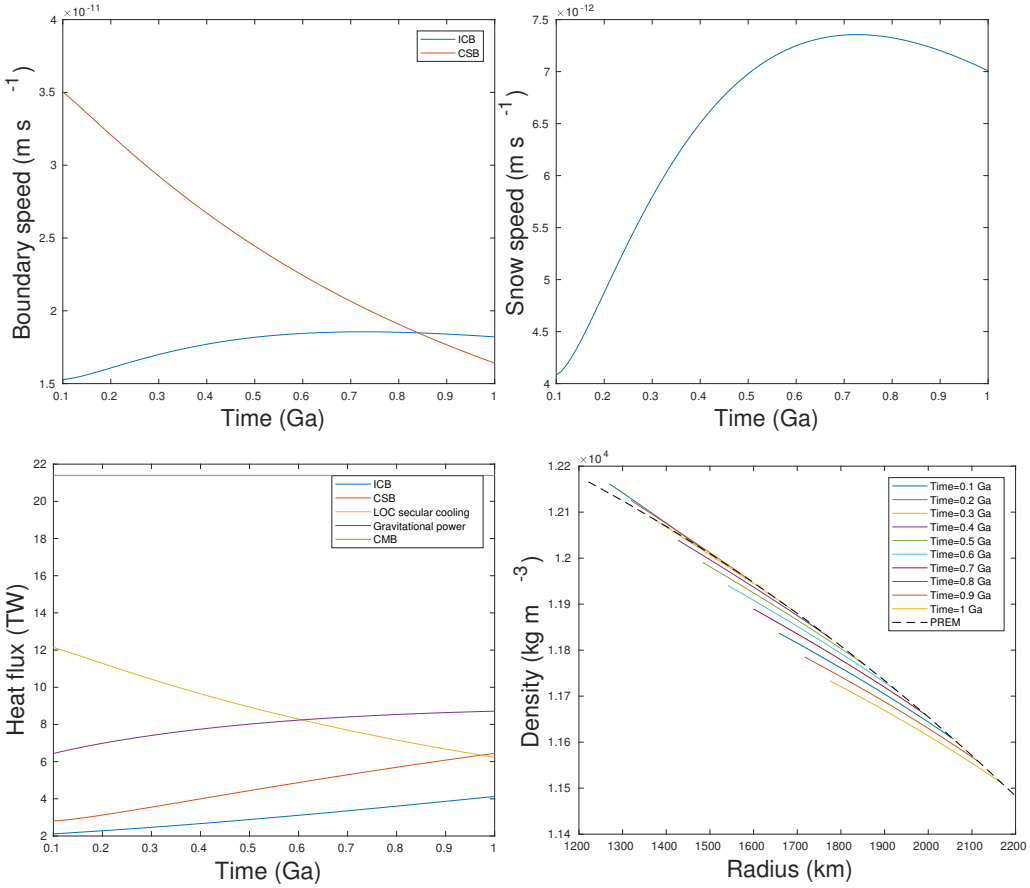

Figure 5.10: Results with a higher CMB heat flow of $Q^c = 21.4$ TW, $F = 2.58$ and $v_f = 11.2 \times 10^{-12}$ ms^{-1}.

CSB speed advances is much greater. The snow speed and hence the total ICB speed, $\dot{r}_i = v_s + v_f$, is also greater than before, but this is dominated by $\dot{r}_{sl}$ to achieve a greater layer thickness overall at $t = 0.1$ Ga. More heat is flowing out of the core than is geophysically plausible, with $Q^c = 21.4$ TW. Nevertheless, by comparing a high heat flow case to a lower heat flow case, key characteristics of the slurry system can be elucidated. The CSB heat flux grows from 2.8 TW at 0.1 Ga to 6.4 TW by 1 Ga, which is almost two terawatts more than at the end of the low heat flow case (see Figure 5.8). Extracting more heat from the slurry steepens the temperature gradient at the CSB even more, so that the light element gradient at the CSB is shallower through the liquidus relation. Therefore if we wish to obtain a more stable oxygen profile, then the heat flow out of the slurry should be large enough to allow a more positive ξ gradient at the CSB through the liquidus. Density stratification above PREM is prolonged and is observed up to 0.2 Ga into the simulation.

5.8 Summary

A time-dependent slurry model is developed to explain the evolution of the F-layer over the course of geological time. The slurry equations are solved in spherical coordinates to account for the geometric effect of large core volumes changing in size over a billion year time-scale. Other physical properties, such as gravity, also become a function of radius over such length-scales. The condition on the oxygen concentration at the CSB becomes dependent on time, because the bulk of the liquid outer core contains a fixed mass of oxygen and the outer core volume significantly reduces over time as the inner core grows, thereby increasing the oxygen density.

The slurry system is coupled to the thermal history of the core by ensuring that the heat flow from the solid inner core and liquid outer core is continuous across the slurry

boundaries. We assume that the inner core is isothermal to prevent it from losing too much heat over time, therefore a freezing speed is introduced at the ICB to release the latent heat necessary to lift the temperature onto the liquidus from an isothermal state. This means the total speed at which the ICB advances due to the flux of solid slurry particles accumulating at the base of the layer also includes this newly introduced freezing speed in addition. No solid flux is allowed at the CSB, since solidification cannot occur outside of the slurry region. We allow a continuous temperature across the CSB so that the liquidus temperature matches with the adiabatic temperature.

A numerical code is developed where a Crank-Nicolson scheme is employed and a Landau transform is applied. This useful transform is commonly used in free boundary problems involving phase change, known as Stefan problems, to deal with boundaries that move in time. Numerical tests were performed to ensure that the time-dependent code is able to reproduce the initial steady-state well. An initial transient phase occurs in the opening 10^{-4} Ga of the time-dependent simulation, as a result of a jump discontinuity in the initial condition. Therefore the initial period of simulation is ignored in the results, since these contain numerical artefacts that do not represent slurry dynamics. A resolution test is applied and it was identified that a mesh resolution using 50 nodes is reliable.

The time-dependent code is initialised using a solution to the steady-state problem modified from Chapter 4 to make the boundary conditions consistent. A condensed list of boundary conditions used to create the initial state compared with the time-dependent problem is presented in Table 5.2.

Results from the time-dependent simulations illustrated prominent features of the slurry system. Solutions of the temperature, light element and solid flux displayed more linear behaviour compared with the previous steady-state results of Chapter 3. Simulations showed that a stable oxygen configuration is difficult to maintain, even

if an initial state containing a stable oxygen profile is input into the system. This is because increased rates of solidification at the base of the layer compared with the top leaves more light element in the residual liquid in this region, therefore destabilising the layer. Barodiffusion remains enhanced using an exponential form, so that the solid flux is able to vanish at the CSB. The F parameter controls how strong the barodiffusive effect is, and is output from the initial state. This parameter is then fixed as an input value throughout the duration of the time-dependent simulation. Limiting the F parameter to a fixed value may contribute to the unstable oxygen configurations determined by the time-dependent system, since this is responsible for the more linear behaviour of the solid flux. In the spherical steady-state set-up, Figure 4.5 shows that the F parameter is sensitive to the CSB heat flux, whereas in the time-dependent system the CSB heat flux varies with time but F does not.

Chapter 6

Conclusion

Contents

6.1 Summary

A self-consistent slurry model was developed and used to explain key features of the F-layer. Previous attempts to explain the F-layer have failed to produce an adequate description of the dynamical processes that allow the layer to remain stably-stratified while simultaneously allowing light material released from freezing out the inner core to pass through it. This thesis has developed a plausible mechanism for explaining the F-layer, and a useful model has been developed so that the possible origin of the F-layer may be explored.

In Chapter 2, the thermodynamics outlined by Loper & Roberts (1977, 1980, 1987) governing the slurry system was extensively examined. Starting from the fundamental conservation laws for mass, energy, and momentum, the governing slurry equations were outlined and a thermodynamically consistent treatment of creating solid phase through freezing a two-component system was derived. The complexity associated with handling a two-component, two-phase, non-equilibrium theory, such as particle history dependence on composition, was discussed. The general non-equilibrium theory was reduced by applying the fast-melting limit, which assumes that the timescale of phase change in the slurry is instantaneous. Consequently, the slurry is in phase equilibrium and is constrained to the liquidus temperature at all times. The liquidus was derived, using the lever rule, that distinctly links the temperature to the light element concentration. The general theory was reduced further by assuming that the slurry mixture is a binary alloy composed of iron and oxygen. By applying a constant solid composition, no oxygen is incorporated into the solid. After assuming both fast-melting and constant solid, the constitutive relations for the diffusive fluxes were elucidated, which completed the conservative equations. A model of mobility was augmented into the solid flux equation to describe the sedimentation of solid parti-

cles according to Stokes' flow. Jump conditions at the layer boundaries were derived from first principles that describe the total mass, solid mass and total energy at the slurry boundaries, which determine the boundary conditions imposed on the system. A global heat balance of the core containing a slurry was established and later used to constrain the results of the model.

A one-dimensional, steady-state box model with a fixed layer thickness was devised in Chapter 3. The slurry was transformed to a frame of reference that moved at the ICB speed as the inner core grows from solid iron particles accumulating at the base of the layer. Approximations were applied to simplify the model, where we assumed that

- the speed of ICB growth was linear, for the sake of simplicity
- light element could not diffuse through the solid so that the self-diffusion coefficient of oxygen became independent of ϕ
- ideal solution theory could be applied so that the thermodynamic derivatives of the chemical potential could be estimated
- gradients of ϕ and the "Soret"-like term in the light element flux were negligible.

The governing equations form a fourth order system of ODEs, and boundary conditions for the box model were developed. We imposed a continuous temperature and oxygen concentration at the CSB, fixing a continuous heat flux at the ICB, as well as a fixing the solid flux at the ICB proportional to the snow speed as iron particles accumulate at the base of the slurry layer. We also forced the solid flux to vanish at the CSB, adding a free parameter that models a turbulent mixing layer at the top of the slurry. Geophysical constraints on the density jump across the layer and the total CMB heat flow were outlined to determine whether solutions to the slurry model are feasible.

Results showed that a steady-state slurry layer can produce a stably-stratified layer that could explain the observed characteristics of the F-layer. Solutions using both high and low thermal conductivities showed that the slurry was compositionally stable and exhibited a total density stratification steeper than PREM.

The box model provided a sound basis for linking the slurry to the rest of the core. In Chapter 4, we modified the geometry and transformed the slurry equations from Cartesian to spherical coordinates, and the appropriate boundary conditions were advanced. We assumed an isothermal inner core that introduced a freezing velocity at the ICB in addition to the previous snow velocity associated with the accumulation of solid particles at the base of the layer. Latent heat release at the ICB lifted the temperature gradient onto the liquidus whilst maintaining an isothermal inner core. An additional constraint on the CSB heat flux was imposed that accounted for the heat extracted from the slurry by the overlying, convective outer core. Melting data from *ab initio* studies was incorporated into the condition on the CSB temperature, so that by fixing the layer thickness the CSB temperature can be matched with the melting data. Other boundary conditions remained the same as in the box model, bringing the total number of boundary conditions to six. As a consequence, the ICB snow speed was an eigenvalue to be determined. Results showed that a sufficient amount of latent heat release at the ICB was required to provide a stable oxygen configuration. Through the liquidus relation, the temperature gradient needed to be large enough to overcome the pressure contribution to provide a positive oxygen gradient. Solutions containing a stable oxygen configuration and a density stratification that exceeded PREM were produced when the freezing speed was equal to $11.2 \times 10^{-12}\ \mathrm{ms}^{-1}$ and the CSB heat flux was higher than $3\ \mathrm{TW}$. The effect of increasing the fixed layer thickness to $300\ \mathrm{km}$ led to an "S" shaped curve in the oxygen profiles. Barodiffusion was less enhanced in the spherical model compared with the box model, resulting in a more linear behaviour

of the solid flux profiles despite having exactly the same conditions on the solid flux imposed at the boundaries. For a specific test case exhibiting a stable stratification, total heat flows between the box and spherical models were compared. This case showed that a slightly steeper CSB temperature gradient in the box model resulted in the generation of more heat coming out of the slurry layer, though the gravitational power was greatly diminished so that the spherical model yielded a higher CMB heat flow overall.

The test case computed from the spherical state model was used as an initial condition for the time-dependent model developed in Chapter 5. Governing time-dependent equations were outlined and boundary conditions were coupled to the thermal history of the core. This was achieved by modifying the condition on the CSB heat flux to admit a time-dependent energy balance, where the cooling adiabat reduces the specific heat lost in the outer core, and the liberation of light elements as core material crystallises increases the gravitational power over time. We assumed that the CMB heat flux was constant, which was calculated from the total CMB heat flux in the initial steady-state. To probe the origins of the F-layer and establish whether it can be formed by a growing slurry layer, the layer thickness was no longer held fixed and was free to be determined by the system. Consequently, the mixing parameter used to enhance diffusion in the turbulent mixing layer was held fixed at its initial state value instead. We assumed that oxygen cannot be created or destroyed in the core, therefore the oxygen concentration at the CSB became variable with time since its density increases as the liquid outer core volume shrinks whilst the inner core grows over geological timescales. Other boundary conditions remained the same as in the spherical steady-state model. We verified the time-dependent code by reproducing the solution from the initial state using a small time-step, however an initial transient period was identified in the solid flux. For a specific test case, we deduced that results from the first 1×10^{-4} Ga

of the simulation should be neglected, to avoid effects of a jump discontinuity from the initial condition, before settling to a more numerically stable state. We also identified that the test case solutions using 50 mesh points was as reliable as using 100 mesh points. Results from the time-dependent model suggested a more linear behaviour of the temperature, oxygen concentration and solid flux profiles compared with the steady box model as a result of fixing the mixing parameter and allowing the layer thickness and ICB solid flux to be freely determined. A stable oxygen profile was difficult to preserve in the few cases tested since more solidification at the base of the layer enriched the residual liquid with buoyant oxygen that destabilises the layer. Over the course of a simulated time period of one billion years, an appreciable amount of growth in layer thickness was detected before it began to diminish. Discovering a regime where the slurry layer was able to grow is a meaningful step towards explaining the origins of the F-layer, though more work is required to determine whether the stratification within the layer can be sustained.

6.2 Project aims revisited

Chapter 1 set out the aims and objectives of the project that guided the research illustrated in this thesis. We revisit these aims and consider whether the objectives have been met:

1. *Derive the governing equations and boundary conditions of a slurry.*

   (a) *Develop a mathematical description of the slurry model based on the general theory of LR77, LR80, LR87, RL87.*

   The thermodynamic foundations of a slurry system were outlined in Chapter 2 and reduced to an idealised fluid dynamical model. This was achieved by applying suitable approximations such as the fast-melting limit and constant solid composition. Conservative equations for the total mass, light element, solid mass, energy and momentum were outlined, and the constitutive equations for the light element, solid mass and entropy flux were derived.

   (b) *Determine appropriate boundary conditions for the slurry layer.*

   Boundary conditions that preserve the conservation laws for energy, mass and momentum were derived from first principles in Chapter 2. Appropriate boundary conditions that were specific to the steady-state box model (Chapter 3), steady-state spherical model (Chapter 4) and the time-dependent model (Chapter 5) were developed further.

2. *Establish a geophysically plausible, one-dimensional, steady-state slurry model.*

   (a) *Derive an idealised, steady-state numerical model that captures the fundamental processes of a slurry.*

   A simple box model was developed in Chapter 3. To ensure the solid flux

vanishes at the CSB, we model a turbulent mixing layer that enhances diffusion, caused by the difference in velocities between the slurry and the vigorously convecting outer core. An equivalent model in spherical coordinates was developed in Chapter 4, wherein more geophysically realistic boundary conditions were advanced. Consequently, this produced some different solutions relative to the box model.

(b) *Explore the parameter space to produce geophysically consistent solutions that explain the F-layer.*

A suite of steady-states was generated by fixing the layer thickness at different values while varying the heat flows and thermal conductivity. Results showed that a slurry is able to produce a stably-stratified layer describing an F-layer that was compatible with the geophysical constraints. Solutions from the spherical steady-state problem formed a suitable initial state for the time-dependent model.

3. *Investigate the geophysical implications of the slurry's presence in the core over time.*

(a) *Present a time-dependent model of the slurry with the relevant boundary conditions that couple the layer to the changing thermal state of the core.*

Chapter 5 retained the time-dependent parts of the slurry equations and allowed the boundaries to move independently from each other so that layer thickness can grow or shrink over time. Boundary conditions were developed so that the CSB heat flow out of the slurry was connected to the evolution of the global heat balance. Numerical tests were implemented to verify the code and establish mesh independence.

(b) *Demonstrate that the F-layer can be formed by a growing slurry layer.*

We have discovered that a time-dependent slurry can undergo a significant period of layer growth over geological time-scales, however the layer quickly destabilises as the light element concentration gradient becomes unstable. Suggestions for how this might be improved have been identified, and a more extensive parameter search is still needed. Recommended further work is provided in Section 6.4.

6.3 Discussion

Several assumptions were made in order to produce a slurry model, and these are appraised in the following discussion. These assumptions include

(i) fast-melting

(ii) constant solid composition

(iii) binary mixture

(iv) ideal solution theory

(v) static slurry

(vi) Stokes' flow model of mobility

(i) The fast-melting limit considerably simplifies the thermodynamics and constrains the system to remain in phase equilibrium, therefore the temperature follows the liquidus in the slurry. Without this limit departures from phase equilibrium must be incorporated into the constitutive relations using a macroscopic measure of the microscopic crystal growth process (Loper, 1992), which is precluded by assuming the fast-melting limit. Nucleation may be a factor that can complicate the slurry model. Classical nucleation theory (Christian, 1965) suggests that critical supercooling rates are as high as $1,000$ K for homogeneous nucleation of the inner core, which is paradoxically so large that the inner core never freezes out (Davies *et al.*, 2019; Huguet *et al.*, 2018). A less extreme position is that the degree of supercooling sufficient for nucleation is attained only at the ICB itself. Though possible it would be difficult to explain the F-layer, since it would not be clear how a consistent thermal and compositional structure could be explained if the layer contained no solid. Alfè *et al.* (2011)

find no evidence of a barrier to melting/freezing using molecular dynamics simulations, and find that the mean waiting time to nucleate iron for a particular supercooling rate decreases as the system size increases. The degree of supercooling required to nucleate solid iron at core conditions during the onset of inner core freezing is poorly constrained, therefore the extent to how nucleation theory applies to the slurry model is unknown in this period of the Earth's history. However once nucleation has occurred there will always be nucleation sites on which iron particles can grow, so supercooling becomes less of an issue. We believe, as did Roberts & Loper (1987), that once nucleation sites have been created the slurry will evolve to a mature slurry state in which fast melting is a reasonable approximation to make compared to other model uncertainties.

(ii) & (iii) Core material is modelled as a simple binary mixture composed of iron and oxygen due to the constant solid assumption. The solid inner core is lighter than if it were composed of pure solid iron (Jephcoat & Olson, 1987) so partitioning light element into the solid phase demands modelling of the composition history within each solid grain. This was not attempted in this study as modelling such a complex particle history significantly complicates the mathematical problem (Roberts & Loper, 1987). However we expect the main dynamical effect within the F-layer is caused by the partitioning of oxygen into the liquid phase when core material freezes, as this creates the compositional density contrast between solid and liquid for light element to rise out of the layer.

We also note that the compositions derived from *ab initio* studies used in the slurry are based on the density jump across the ICB determined by seismology. Since solutions to the slurry model yield differing density jumps across the ICB, then strictly-speaking the composition of the core must be updated to reflect this change. Considering that the model is complicated enough already, this effect has not been studied but could be improved. We think that these approximations are sensible compromises

given the present knowledge of the core and the current complexity of the model.

(iv) Ideal solution theory is used to estimate parameters, such as changes in density and the chemical potential, that are difficult to measure experimentally at the relevant core pressures and temperatures. Ideal solutions exclude the possibility of chemical reactions between iron and light element. Whilst ideal solution theory is accurate for predicting densities, it does not predict the chemical potential or its derivatives well at core conditions (Gubbins *et al.*, 2004). Departures from ideal solution theory may alter the liquidus curve and its intersection with the adiabat that controls the CSB temperature, which may significantly impact our results. Currently, ideal solution theory is sufficient, though we expect parameter estimates to improve with future experiments.

(v) The slurry is assumed to be non-convecting, however coupling the momentum equation (2.9.1i) to the system allows the convecting state to be investigated. Exploring its linear stability may map out the different regimes of slurry convection and provide a deeper understanding of the system. Possible scenarios include a phase instability that can arise when lateral variations of solid phase induce overturning (Loper & Roberts, 1987). Nevertheless, maintaining a net stable stratification will remain a key requirement in such a convecting state in order to be consistent with the geophysical observations.

(vi) Estimating mean solid particle size in models of particle mobility is important in characterising sedimentation. It is unlikely that direct measurements of this property will be made in the Earth's core, however an advantage of the slurry model is that only the solid flux needs to be calculated. If so desired, the model of mobility provides an estimate of the solid fraction, ϕ, using the solid flux, $\mathbf{j}$. Further work investigating the mobility may shed light on the range of admissible particle sizes encountered in the core. Estimates of particle sizes in alternative physical situations may benefit this problem – for example growth and coagulation of raindrops used in the existing slurry

theory (Loper & Roberts, 1977), and helium droplets in Saturn and Jupiter in iron snow models (Rückriemen *et al.*, 2015).

If the model conditions (i)–(vi) are met, then a present-day slurry is likely to exist that can explain the F-layer given the current geophysical observations. If $\mathrm{d}T_a/\mathrm{d}p < \mathrm{d}T_l/\mathrm{d}p < \mathrm{d}T_c/\mathrm{d}p$, where $\mathrm{d}T_l/\mathrm{d}p$ is the liquidus gradient and $\mathrm{d}T_c/\mathrm{d}p$ is the conduction gradient, then a slurry is inevitable (Loper & Roberts, 1977). Current estimates for the thermal conductivity and ICB heat flux satisfy the above inequality. If $\mathrm{d}T_c/\mathrm{d}p < \mathrm{d}T_l/\mathrm{d}p$ then freezing may occur directly onto the inner core and a small conductive sub-layer is possible, but this alone cannot explain the stable stratification inferred from seismology.

Under the fast-melting limit our slurry model idealises that the inner core grows exclusively by solid particles settling at the ICB under Stokes' flow. Alternatively, it has been proposed that the inner core may grow through a mushy layer, where constitutional supercooling ahead of the ICB promotes dendritic crystal growth of solid iron at the interface (Fearn *et al.*, 1981). The solid fraction of a mush is significantly greater than a slurry, as we have assumed $\phi \ll 1$ throughout our model. Deguen *et al.* (2007) conduct a linear stability analysis to find that the interdendritic spacing is at least several metres wide at the ICB in its current state, with an approximate layer thickness of $300\ \mathrm{km}$ extending into the inner core. The top of the mush must be at the ICB to be consistent with the sharpness of the seismic velocity jump (Fearn *et al.*, 1981) and is thought to be strongly influenced by convection, the effect of which is poorly understood. Huguet *et al.* (2016) use experimental methods to suggest that mush convection is the dominant regime in the inner core, leaving a matrix with a solid fraction close to unity without the effect of compaction (a collapsing mush). If the inner core grows dendritically then our model of a slurry layer cannot overlay a mush, since by the fast-melting limit, the dendrites would grow to the point where the liquidus and adiabat

intersect at the CSB. A solid matrix extending to the top of the layer would have been seismically detectable, therefore it is unlikely the slurry and mush combination could explain the F-layer in this situation.

6.4 Further work

This thesis has developed a self-consistent and idealised slurry model that offers a great opportunity for further research. The steady-state models successfully explain the stably-stratified F-layer that is coherent with present-day observations and current understanding of core heat flows. Time-dependent results in Chapter 5 form a preliminary investigation into the origin of the F-layer and its future evolution. Further avenues of research to extend this work are proposed as follows:

1. *Explore the parameter space in the spherical steady-state model*

   A rudimentary parameter search is performed in Chapter 4, however we suspect that many other suitable solutions containing a stable oxygen configuration remain to be found and used to initialise the time-dependent model. A systematic search would map out how layer thickness, CSB heat flow, freezing speed and thermal conductivity may affect slurry behaviour and reveal the conditions in which the slurry layer is stable. A promising route could be to increase the amount of heat that is extracted through the CSB, which steepens the temperature gradient at the CSB. As a result, the oxygen gradient at the CSB becomes more positive because this is linked to the temperature via the liquidus relation, therefore increasing the likelihood of securing a stable oxygen profile. Another key parameter to vary is the thermal conductivity since this also directly impacts the condition on the temperature gradient at the ICB. A smaller thermal conductivity would increase the ICB oxygen gradient, which may increase the likelihood of preserving a stable oxygen profile in the time-dependent cases.

2. *Improve the time-dependent model*

   (a) The time-dependent model is limited by fixing the mixing parameter, F, at a constant value rather than being freely determined as in the steady-state

cases. This parameter is normally controlled by the zero solid flux condition at the CSB. The time-dependent slurry equations form a fourth order system, with two boundary conditions on the heat flux, two on the solid flux, one on the CSB oxygen concentration and one on the CSB temperature. By relaxing the fixed layer thickness condition, the condition on the CSB temperature is no longer a constraint on the temperature but a condition that determines the CSB position. Therefore if the F parameter is not held constant, then an extra condition is required to constrain it. For instance, a simple model of inner core growth could provide a value for the snow speed, v_s, prescribed on the solid flux at the ICB, so that the F parameter becomes free to be computed by the time-dependent model. Otherwise, a systematic search varying this parameter is possible.

(b) Freezing speed, v_f, is arbitrarily fixed and assumed to be constant over time. We could suppose that the freezing speed is related to the snow speed, v_s, by a simple linear relationship so that a feedback mechanism is provided. This would affect the competition between the ICB speed and the CSB speed, which affects the evolution of the layer thickness.

(c) A more sophisticated model of the core that is geophysically realistic could be developed. Effects of the Coriolis force due to the Earth's rotation and the Lorentz force from the electromagnetic field should be included. For the sake of simplicity, these effects are overlooked in this thesis, however a comprehensive study of how a slurry F-layer could potentially impact core dynamics and dynamo operation is warranted.

Appendix A

Gravitational power

Gravitational energy is released when light element from the slurry moves into the convecting liquid outer core. The energy provided helps to power the dynamo, and the heat released, $Q_g(t)$, enters into the global energy balance (5.2.1).

Consider the gravitational force acting on a point particle of mass m_i located at radius r from the centre of a spherically symmetric mass (Figure A.1). Then by Newton's law of gravitation, we have

$$\mathbf{F_i} = -\frac{Gm_iM}{r^2}\hat{\mathbf{r}}, \tag{A.1}$$

where G is the universal gravitational constant, M is the mass contained within radius

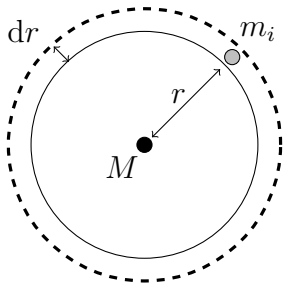

Figure A.1: Point particle with mass m_i is located at radius r from the centre of a spherically symmetric mass, expressed as a point mass in the centre, M. Particle m_i exists within an infinitesimally thin shell of iron of thickness $\mathrm{d}r$.

r, expressed as a point mass at the centre. Loss of gravitational potential energy is equivalent to the work gained, U_i, to bring the point particle from radius r to infinity, therefore

$$U_i = \int_r^\infty \mathbf{F_i} \cdot \mathrm{d}\mathbf{r}' = \int_r^\infty -\frac{Gm_iM}{r'^2}\,\mathrm{d}r' = \frac{Gm_iM}{r}. \tag{A.2}$$

The sum total of the mass in an infinitesimally thin shell of iron with thickness $\mathrm{d}r$ is

$$\mathrm{d}m = 4\pi\rho(r)r^2\mathrm{d}r. \tag{A.3}$$

Therefore the gravitational potential energy of an infinitesimally thin shell of iron is

$$\mathrm{d}U = \frac{GM}{r}\mathrm{d}m = 4\pi\rho(r)rGM\mathrm{d}r. \tag{A.4}$$

To obtain the gravitational energy of the iron in the liquid outer core, we integrate over every infinitesimally thin shell of iron from the CSB to the CMB so that

$$U = 4\pi\int_{r_{sl}}^{r_o} GM\rho(r)r\,\mathrm{d}r = 4\pi\int_{r_{sl}}^{r_o}\rho(r)g(r)r^3\,\mathrm{d}r, \tag{A.5}$$

where $g(r) = GM/r^2$ is the gravitational acceleration.

After time δt, the interface r_{sl} has moved to $r_{sl} + \delta r$, where $\dot{r}_{sl} = \delta r/\delta t$. The change in gravitational potential energy of iron in the liquid outer core is

$$\frac{\mathrm{d}U^l_{Fe}}{\mathrm{d}t} = \frac{4\pi}{\delta t}\left\{\int_{r_{sl}}^{r_c}\rho(r)g(r)r^3\,\mathrm{d}r - \int_{r_{sl}+\delta r}^{r_c}\rho(r)g(r)r^3\,\mathrm{d}r\right\} \tag{A.6}$$

and the change in gravitational potential energy in the slurry is

$$\frac{\mathrm{d}U^{sl}_{Fe}}{\mathrm{d}t} = \frac{4\pi}{\delta t}\left\{\int_{r_i}^{r_{sl}}\rho(r)g(r)r^3\,\mathrm{d}r - \int_{r_i}^{r_{sl}+\delta r}\rho(r)g(r)r^3\,\mathrm{d}r\right\}. \tag{A.7}$$

Though the liquid outer core has lost energy, the slurry has gained exactly the same amount. There is no net change in the gravitational potential energy of the core and

$$\frac{\mathrm{d}U_{Fe}}{\mathrm{d}t} = \frac{\mathrm{d}U^{l}_{Fe}}{\mathrm{d}t} + \frac{\mathrm{d}U^{sl}_{Fe}}{\mathrm{d}t} = 0, \tag{A.8}$$

hence this does not contribute to the global energy balance.

The same argument does not apply to the gravitational potential energy of the light element, since there is work done to move it from the slurry to mix into the convecting liquid outer core. The total gravitational energy of light element in the liquid outer core is

$$U_O = 4\pi \int_{r_{sl}}^{r_o} \rho(r)\xi(r_{sl},t)g(r)r^3 \,\mathrm{d}r = \int_{r_{sl}}^{r_o} \frac{3M_O}{(r_c^3 - r_{sl}^3)} g(r)r^3 \,\mathrm{d}r, \tag{A.9}$$

where

$$\rho(r)\xi(r_{sl},t) = \frac{M_O}{\frac{4\pi}{3}\left(r_c^3 - r_{sl}^3\right)}, \tag{A.10}$$

is the oxygen density in the liquid OC. After time δt, the change in gravitational energy of light element in the liquid outer core is

$$\begin{aligned}
\frac{\mathrm{d}U^{l}_{O}}{\mathrm{d}t} &= \frac{1}{\delta t}\left\{\int_{r_{sl}}^{r_c} \frac{3M_O}{(r_c^3 - r_{sl}^3)} g(r)r^3 \,\mathrm{d}r - \int_{r_{sl}+\delta r}^{r_c} \frac{3M_O}{(r_c^3 - (r_{sl}+\delta r)^3)} g(r)r^3 \,\mathrm{d}r\right\} \\
&\simeq \frac{1}{\delta t}\left\{\int_{r_{sl}}^{r_c} \frac{3M_O}{(r_c^3 - r_{sl}^3)} g(r)r^3 \,\mathrm{d}r - \int_{r_{sl}+\delta r}^{r_c} \frac{3M_O}{(r_c^3 - r_{sl}^3)} g(r)r^3 \,\mathrm{d}r \right. \\
&\qquad \left. - \int_{r_{sl}+\delta r}^{r_c} \frac{3M_O}{(r_c^3 - r_{sl}^3)} \cdot \frac{3r_{sl}^2 \delta r}{(r_c^3 - r_{sl}^3)} g(r)r^3 \,\mathrm{d}r\right\},
\end{aligned} \tag{A.11}$$

where we approximate $(r_{sl} + \delta r)^3 \simeq r_{sl}^3 + 3r_{sl}^2\delta r$. The change in gravitational energy

in the slurry is

$$\frac{\mathrm{d}U_O^{sl}}{\mathrm{d}t} = \frac{1}{\delta t}\left\{\int_{r_i}^{r_{sl}} \frac{3M_O}{\frac{4\pi}{3}\left(r_c^3 - r_{sl}^3\right)} g(r) r^3 \,\mathrm{d}r - \int_{r_i}^{r_{sl}+\delta r} \frac{3M_O}{\frac{4\pi}{3}\left(r_c^3 - r_{sl}^3\right)} g(r) r^3 \,\mathrm{d}r\right\} \tag{A.12}$$

The net change in the gravitational potential energy of light element in the core is

$$\frac{\mathrm{d}U_O}{\mathrm{d}t} = \frac{\mathrm{d}U_O^{l}}{\mathrm{d}t} + \frac{\mathrm{d}U_O^{sl}}{\mathrm{d}t} = -\frac{\delta r}{\delta t}\int_{r_{sl}+\delta r}^{r_c} \frac{9M_O r_{sl}^2}{\left(r_c^3 - r_{sl}^3\right)^2} g(r) r^3 \,\mathrm{d}r, \tag{A.13}$$

which is decreasing over time since work is done to stir light element into the liquid core. The available gravitational energy is converted to heat as it powers the dynamo, therefore positively contributing to the CMB heat flux by

$$Q_g(t) = \dot{r}_{sl}\int_{r_{sl}+\delta r}^{r_c} \frac{9M_O r_{sl}^2}{\left(r_c^3 - r_{sl}^3\right)^2} g(r) r^3 \,\mathrm{d}r, \tag{A.14}$$

where $\dot{r}_{sl} = \frac{\delta r}{\delta t}$ is the CSB speed.

References

ADAM, J.C. & ROMANOWICZ, B. (2015). Global scale observations of scattered energy near the inner-core boundary: Seismic constraints on the base of the outer-core. *Physics of the Earth and Planetary Interiors*, **245**, 103–116. 16, 28

ADAM, J.C., IBOURICHÈNE, A. & ROMANOWICZ, B. (2018). Observation of core sensitive phases: Constraints on the velocity and attenuation profile in the vicinity of the inner-core boundary. *Physics of the Earth and Planetary Interiors*, **275**, 19–31. 22

ALBOUSSIÈRE, T., DEGUEN, R. & MELZANI, M. (2010). Melting-induced stratification above the Earth's inner core due to convective translation. *Nature*, **466**, 744–747. 20

ALEXIADES, V. (1992). *Mathematical Modeling Of Melting And Freezing Processes*. Taylor & Francis. 144

ALFÈ, D. (2009). Temperature of the inner-core boundary of the Earth: Melting of iron at high pressure from first-principles coexistence simulations. *Phys. Rev. B (Rapids)*, **79**, 1–4. xv, 7, 8

ALFÈ, D., GILLAN, M. & PRICE, G. (2002a). Composition and temperature of the Earth's core constrained by combining *ab initio* calculations and seismic data. *Earth Planet. Sci. Lett.*, **195**, 91–98. xvi, 11, 12, 27, 33, 73, 92, 95

ALFÈ, D., GILLAN, M. & PRICE, G. (2002b). *Ab initio* chemical potentials of solid and liquid solutions and the chemistry of the Earth's core. *J. Chem. Phys.*, **116**, 7127–7136. 84, 92, 94

ALFÈ, D., PRICE, G. & GILLAN, M. (2002c). Iron under Earth's core conditions: Liquid-state thermodynamics and high-pressure melting curve from *ab initio* calculations. *Phys. Rev. B*, **65**, 165118. xv, xvii, 7, 8, 91

ALFE, D., VOČADLO, L., PRICE, G. & GILLAN, M. (2004). Melting curve of materials: theory versus experiments. *Journal of Physics: Condensed Matter*, **16**, S973. 7

ALFÈ, D., GILLAN, M.J. & PRICE, G.D. (2007). Temperature and composition of the Earth's core. *Contemp. Phys.*, **48**, 63–80. 94

ALFÈ, D., CAZORLA, C. & GILLAN, M. (2011). The kinetics of homogeneous melting beyond the limit of superheating. *J. Chemical Physics*, **135**, 024102. 179

ANZELLINI, S., DEWAELE, A., MEZOUAR, M., LOUBEYRE, P. & MORARD, G. (2013). Melting of iron at Earth's inner core boundary based on fast X-ray diffraction. *Science*, **340**, 464–466. xv, 7, 8

BADRO, J., CÔTÉ, A. & BRODHOLT, J. (2014). A seismologically consistent compositional model of Earth's core. *Proc. Natl. Acad. Sci.*, **111**, 7542–7545. 11, 13, 27

BELONOSHKO, A., AHUJA, R. & JOHANSSON, B. (2000). Quasi–*ab Initio* molecular dynamic study of Fe melting. *Phys. Rev. Lett.*, **84**, 3638–3641. xv, 7, 8

BIRCH, F. (1952). Elasticity and the constitution of Earth's interior. *J. Geophys. Res.*, **66**, 227–286. 10, 27

BIRCH, F. (1964). Density and composition of mantle and core. *Journal of geophysical research*, **69**, 4377–4388. 11

BOEHLER, R. (1993). Temperatures in the Earth's core from melting-point measurements of iron at high static pressures. *Nature*, **363**, 534. xv, 7, 8

BRAGINSKY, S. (1963). Structure of the F layer and reasons for convection in the Earth's core. *Sov. Phys. Dokl.*, **149**, 8–10. 18, 19, 22

BROWN, J.M. & MCQUEEN, R.G. (1986). Phase transitions, Grüneisen parameter, and elasticity for shocked iron between 77 GPa and 400 GPa. *J. Geophys. Res.*, **91**, 7485. xv, 7, 8

BUFFETT, B., HUPPERT, H., LISTER, J. & WOODS, A. (1996). On the thermal evolution of the Earth's core. *J. Geophys. Res.*, **101**, 7989–8006. 72, 81

BULLEN, K.E. (1953). *An introduction to the theory of seismology*. University Press. 14

CHANDRASEKHAR, S. (1961). *Hydrodynamic and Hydromagnetic Stability*. International Series of Monographs on Physics, Dover. 46, 58

CHESTER, G. & THELLUNG, A. (1961). The law of Wiedemann and Franz. *Proc. Phys. Soc. London*, **77**, 1005–1013. 9

CHRISTIAN, I. (1965). *The Theory of Transformations in Metals and Alloys, 816*. Pergamon Press, Oxford. 179

CHRISTIAN, J.W. (2002). *The theory of transformations in metals and alloys*. Newnes. 21

CLEARY, J. & HADDON, R. (1972). Seismic wave scattering near the core-mantle boundary: a new interpretation of precursors to PKP. *Nature*, **240**, 549. 14

DAVIES, C. (2015). Cooling history of Earth's core with high thermal conductivity. *Phys. Earth Planet. Int.*. 58

DAVIES, C., POZZO, M., GUBBINS, D. & ALFÈ, D. (2015). Constraints from material properties on the dynamics and evolution of Earths core. *Nat. Geosci.*, **8**, 678–687. 13, 28, 93, 94, 95, 98, 104, 120, 121

DAVIES, C., POZZO, M. & ALFÈ, D. (2019). Assessing the inner core nucleation paradox with atomic-scale simulations. *Earth and Planetary Science Letters*, **507**, 1–9. 179

DAVIES, J. & DAVIES, D. (2010). Earth's surface heat flux. *Solid Earth*, **1**, 5–24. 118

DE KOKER, N., STEINLE-NEUMANN, G. & VOJTECH, V. (2012). Electrical resistivity and thermal conductivity of liquid Fe alloys at high P and T and heat flux in Earth's core. *Proc. Natl. Acad. Sci.*, **109**, 4070–4073. 9

DEGUEN, R. (2012). Structure and dynamics of Earth's inner core. *Earth Planet. Sci. Lett.*, **333–334**, 211–225. 20

DEGUEN, R., ALBOUSSIÈRE, T. & BRITO, D. (2007). On the existence and structure of a mush at the inner core boundary of the Earth. *Phys. Earth Planet. Int.*, **164**, 36–49. 21, 22, 182

DEGUEN, R., ALBOUSSIÈRE, T. & CARDIN, P. (2013). Thermal convection in Earth's inner core with phase change at its boundary. *Geophys. J. Int.*, **194**. 20

DEGUEN, R., OLSON, P. & REYNOLDS, E. (2014). F-layer formation in the outer core with asymmetric inner core growth. *Comptes Rendus Geoscience*, **346**, 101–109. 21

DEGUEN, R., ALBOUSSIÉRE, T. & LABROSSE, S. (2018). Double-diffusive translation of Earths inner core. *Geophysical Journal International*, **214**, 88–107. 21

DEUSS, A. (2014). Heterogeneity and anisotropy of Earth's inner core. *Annu. Rev. Earth Planet. Sci.*, **42**, 103–126. 11, 96

DZIEWONSKI, A. & ANDERSON, D. (1981). Preliminary Reference Earth Model. *Phys. Earth Planet. Int.*, **25**, 297–356. xvi, xvii, 3, 14, 15, 17, 79, 85, 89, 92, 94, 97, 143, 149

DZIEWONSKI, A. & ROMANOWICZ, B. (2015). Overview. In G. Schubert, ed., *Treatise on Geophysics 2nd Edn, Vol. 1*, 1–29, Elsevier, Amsterdam. 90

FEARN, D., LOPER, D. & ROBERTS, P. (1981). Structure of the Earth's inner core. *Nature*, **291**, 232–233. 21, 182

GARNERO, E. (Accessed: 04-10-2018). Models of the Earth's interior. `http://garnero.asu.edu`. xvi, 15

GAUSS, C.F. (1877). General theory of Earth magnetism. In *Werke*, 119–193. 3

GLATZMAIER, G.A. & COE, R. (2015). Magnetic polarity reversals in the core. *Treatise on geophysics*, **8**, 279–295. 3, 27

GOMI, H., OHTA, K., HIROSE, K., LABROSSE, S., CARACAS, R., VERSTRAETE, V. & HERNLUND, J. (2013). The high conductivity of iron and thermal evolution of the Earth's core. *Phys. Earth Planet. Int.*, **224**, 88–103. 9, 93, 95

GUBBINS, D. (1977). Energetics of the Earth's core. *J. Geophys.*, **43**, 453–464. 72

GUBBINS, D., ALFE, D., MASTERS, G., PRICE, G. & GILLAN, M. (2003). Can the Earth's dynamo run on heat alone? *Geophys. J. Int.*, **155**, 609–622. xvii, 5, 16, 58, 84, 90, 91, 94, 95, 98, 100

GUBBINS, D., ALFÈ, D., MASTERS, G., PRICE, G. & GILLAN, M. (2004). Gross thermodynamics of two-component core convection. *Geophys. J. Int.*, **157**, 1407–1414. 27, 42, 54, 56, 58, 82, 90, 92, 94, 95, 100, 181

GUBBINS, D., MASTERS, G. & NIMMO, F. (2008). A thermochemical boundary layer at the base of Earth's outer core and independent estimate of core heat flux. *Geophys. J. Int.*, **174**, 1007–1018. xvi, 16, 17, 19, 20, 22, 29, 81, 145

GUBBINS, D., ALFÈ, D. & DAVIES, C. (2013). Compositional instability of Earth's solid inner core. *Geophys. Res. Lett.*, **40**, 1084–1088. 20

HILLS, R., LOPER, D. & ROBERTS, P. (1983). A thermodynamically consistent model of a mushy zone. *The Quarterly Journal of Mechanics and Applied Mathematics*, **36**, 505–540. 21

HIROSE, K., LABROSSE, S. & HERNLUND, J. (2013). Compositional state of Earth's core. *Annual Review of Earth and Planetary Sciences*, **41**, 657–691. 11, 13, 27

HUGUET, L., ALBOUSSIÈRE, T., BERGMAN, M., DEGUEN, R., LABROSSE, S. & LESŒ UR, G. (2016). Structure of a mushy later under hypergravity with implications for Earth's inner core. *Geophys. J. Int.*, **204**, 1729–1755. 182

HUGUET, L., VAN ORMAN, J., HAUCK II, S. & WILLARD, M. (2018). Earth's inner core nucleation paradox. *Earth Planet. Sci. Lett.*, **487**, 9–20. 22, 179

ICHIKAWA, H., TSUCHIYA, T. & TANGE, Y. (2014). The P-V-T equation of state and thermodynamic properties of liquid iron. *J. Geophys. Res.*, **119**, 240–252. 89

JACKSON, J., STURHAHN, W., LERCHE, M., ZHAO, J., TOELLNER, T., ERCAN ALP, E., SINOGEIKIN, S., BASS, J., MURPHY, C. & WICKS, J. (2013). Melting of compressed iron by monitoring atomic dynamics. *Earth Planet. Sci. Lett.*, **362**, 143–150. xv, 7, 8

JACOBS, J. (1953). The Earth's inner core. *Nature*, **172**, 297–300. xv, 4, 28

JAULT, D. & LE MOUËL, J. (1991). Physical properties at the top of the core and core surface motions. *Physics of the Earth and Planetary Interiors*, **68**, 76–84. 5

JAUPART, C., LABROSSE, S. & MARESCHAL, J.C. (2007). Temperatures, heat and energy in the mantle of the Earth. In G. Schubert, ed., *Treatise on Geophysics, Vol. 7*, 254–303, Elsevier, Amsterdam. 3

JEFFREYS, H. (1926). The rigidity of the Earth's central core. *Geophysical Journal International*, **1**, 371–383. 10

JEFFREYS, H. (1939). The times of the core waves (second paper). *Geophysical Journal International*, **4**, 594–615. 14

JEPHCOAT, A. & OLSON, P. (1987). Is the inner core of the Earth pure iron? *Nature*, **325**, 332–335. 11, 180

KANESHIMA, S., HIRAHARA, K., OHTAKI, T. & YOSHIDA, Y. (1994). Seismic structure near the inner core-outer core boundary. *Geophysical research letters*, **21**, 157–160. xvi, 17

KENNETT, B., ENGDAHL, E. & BULAND, R. (1995). Constraints on seismic velocities in the Earth from traveltimes. *Geophys. J. Int.*, **122**, 108–124. 16

KING, D., HADDON, R. & CLEARY, J. (1973). Evidence for seismic wave scattering in the D double prime layer. *Earth and Planetary Science Letters*, **20**, 353–356. 14

KOMABAYASHI, T. (2014). Thermodynamics of melting relations in the system Fe-FeO at high pressure: Implications for oxygen in the Earth's core. *Journal of Geophysical Research: Solid Earth*, **119**, 4164–4177. 7

KOMABAYASHI, T. & FEI, Y. (2010). Internally consistent thermodynamic database for iron to the Earth's core conditions. *Journal of Geophysical Research: Solid Earth*, **115**. xv, 7, 8

KONO, M. & ROBERTS, P. (2002). Recent geodynamo simulations and observations of the geomagnetic field. *Rev. Geophys.*, **40**, 1013–1061. 3

KONÔPKOVÁ, Z., MCWILLIAMS, R., GÓMEZ-PÉREZ, N. & GONCHAROV, A. (2016). Direct measurement of thermal conductivity in solid iron at planetary core conditions. *Nature*, **534**, 99–101. 9, 93, 107

KOPER, K.D. & PYLE, M.L. (2004). Observations of PKiKP/PcP amplitude ratios and implications for Earth structure at the boundaries of the liquid core. *J. Geophys. Res.*, **109**, art. no.–B03301. 11

KUNDU, P., COHEN, I. & DOWLING, D. (2015). *Fluid Mechanics*. Elsevier Science. 58, 70

LABROSSE, S. (2014). Thermal and compositional stratification of the inner core. *C. R. Geosci.*, **346**, 119–129. 20

LANDAU, L. & LIFSHITZ, E. (1959). *Course of Theoretical Physics, Vol.6: Fluid Mechanics*. Pergammon, London. 36, 54, 59

LANDAU, L.D., LIFSHITZ, E.M. & PITAEVSKII, L. (1980). Statistical physics, part i. 6, 40, 53, 64

LARMOR, J. (1919). How could a rotating body such as the sun become a magnet? *Brit. Assn. Adv. Sci. Rep*, 159–160. 3, 27

LAY, T., WILLIAMS, Q. & GARNERO, E. (1998). The core-mantle boundary layer and deep Earth dynamics. *Nature*, **392**, 461–468. 14

LAY, T., HERNLUND, J. & BUFFETT, B. (2008). Core-mantle boundary heat flow. *Nat. Geosci.*, **1**, 25–32. 3, 28, 95

LEHMANN, I. (1936). P, publ. *Bur. Centr. Seism. Internat. Serie A*, **14**, 87–115. 10

LOPER, D. (1992). A nonequilibrium theory of a slurry. *Continuum Mech. Thermodyn.*, **4**, 213–245. 179

LOPER, D. & ROBERTS, P. (1977). On the motion of an iron-alloy core containing a slurry: I. general theory. *Geophys. Astrophys. Fluid Dyn.*, **9**, 289–321. 22, 23, 24, 25, 29, 33, 37, 39, 40, 48, 53, 54, 56, 68, 71, 73, 171, 182

LOPER, D. & ROBERTS, P. (1980). On the motion of an iron-alloy core containing a slurry: II. a simple model. *Geophys. Astrophys. Fluid Dyn.*, **16**, 83–127. 23, 24, 29, 33, 53, 54, 59, 68, 73, 82, 171

LOPER, D. & ROBERTS, P. (1987). A Boussinesq model of a slurry. *Structure and Dynamics of Partially Solidified Systems*, 291–323. 23, 24, 29, 33, 60, 64, 68, 73, 171, 181

LOPER, D.E. & ROBERTS, P.H. (1981). A study of conditions at the inner core boundary of the Earth. *Physics of the Earth and Planetary Interiors*, **24**, 302–307. 21, 22

LYTHGOE, K., RUDGE, J., NEUFELD, J. & DEUSS, A. (2015). The feasibility of thermal and compositional convection in Earth's inner core. *Geophys. J. Int.*, **385**, 764–782. 20

MA, Y., SOMAYAZULU, M., SHEN, G., MAO, H.K., SHU, J. & HEMLEY, R.J. (2004). In situ X-ray diffraction studies of iron to Earth-core conditions. *Physics of the Earth and Planetary Interiors*, **143**, 455–467. xv, 7, 8

MASTERS, G. & GUBBINS, D. (2003). On the resolution of density within the Earth. *Phys. Earth Planet. Int.*, **140**, 159–167. 11

MCDONOUGH, W. & SUN, S.S. (1995). The composition of the Earth. *Chem. Geol.*, **120**, 223–253. 11, 27

MELCHIOR, P. (1986). *The physics of Earth's interior: an introduction*. Permagon Books. 7

MORAN, M.J., SHAPIRO, H.N., BOETTNER, D.D. & BAILEY, M.B. (2010). *Fundamentals of engineering thermodynamics*. John Wiley & Sons. 46, 52

MORARD, G., ANDRAULT, D., ANTONANGELI, D. & BOUCHET, J. (2014). Properties of iron alloys under the Earth's core conditions. *C. R. Geoscience*, **346**, 130–139. xv, 6

MORTON, K. & MAYERS, D. (2005). *Numerical Solution of Partial Differential Equations: An Introduction*. Numerical Solution of Partial Differential Equations: An Introduction, Cambridge University Press. 146

NAKAGAWA, T. & TACKLEY, P. (2007). Lateral variations in CMB heat flux and deep mantle seismic velocity caused by a thermal-chemical-phase boundary layer in 3D spherical convection. *Earth Planet. Sci. Lett.*, **271**, 348–358. 3

NAKAJIMA, Y., IMADA, S., HIROSE, K., KOMABAYASHI, T., OZAWA, H., TATENO, S., TSUTSUI, S., KUWAYAMA, Y. & BARON, A.Q. (2015). Carbon-depleted outer core revealed by sound velocity measurements of liquid iron–carbon alloy. *Nature communications*, **6**, 8942. 13

NGUYEN, J. & HOLMES, N. (2004). Melting of iron at the physical conditions of the Earth's core. *Nature*, **427**, 339–342. xv, 7, 8

NIMMO, F. (2015a). Energetics of the core. In G. Schubert, ed., *Treatise on Geophysics 2nd Edn, Vol. 9*, 31–65, Elsevier, Amsterdam. 18, 27, 28, 58, 95, 98

NIMMO, F. (2015b). Thermal and compositional evolution of the core. In G. Schubert, ed., *Treatise on Geophysics 2nd Edn, Vol. 9*, 201–219, Elsevier, Amsterdam. 3

OHTA, K., KUWAYAMA, Y., HIROSE, K., SHIMIZU, K. & OHISHI, Y. (2016). Experimental determination of the electrical resistivity of iron at Earths core conditions. *Nature*, **534**, 95. 9, 93

OHTAKI, T. & KANESHIMA, S. (2015). Independent estimate of velocity structure of Earth's lowermost outer core beneath the northeast Pacific from PKiKP- PKPbc differential traveltime and dispersion in PKPbc. *Journal of Geophysical Research: Solid Earth*, **120**, 7572–7586. 16, 28

OLDHAM, R.D. (1906). The constitution of the interior of the Earth, as revealed by earthquakes. *Quarterly Journal of the Geological Society*, **62**, 456–475. 10

POIRIER, J.P. (1994). *Introduction to the physics of Earth's interior*. Cambridge University Press, 2nd edn. 11, 27

POUROVSKII, L., MRAVLJE, J., FERRERO, M., PARCOLLET, O. & ABRIKOSOV, I. (2014). Impact of electronic correlations on the equation of state and transport in ϵ-Fe. *Phys. Rev. B*, **90**, 155120. 9

POZZO, M., DAVIES, C., GUBBINS, D. & ALFÈ, D. (2012). Thermal and electrical conductivity of iron at Earth's core conditions. *Nature*, **485**, 355–358. 9

POZZO, M., DAVIES, C., GUBBINS, D. & ALFÈ, D. (2013). Transport properties for liquid silicon-oxygen-iron mixtures at Earth's core conditions. *Phys. Rev. B*, **87**, 014110. xvii, 92, 95, 120, 121

POZZO, M., DAVIES, C., GUBBINS, D. & ALFÈ, D. (2014). Thermal and electrical conductivity of solid iron and iron-silicon mixtures at Earth's core conditions. *Earth Planet. Sci. Lett.*, **393**, 159–164. 80, 95, 118, 124

RAHMAN, M. & SAGHIR, M. (2014). Thermodiffusion or Soret effect: Historical review. *International Journal of Heat and Mass Transfer*, **73**, 693–705. 54

ROBERTS, P. & LOPER, D. (1987). Dynamical processes in slurries. In *Structure and dynamics of partially solidified systems*, 229–290, Springer. 6, 23, 24, 29, 33, 68, 73, 180

RÜCKRIEMEN, T., BREUER, D. & SPOHN, T. (2015). The Fe snow regime in Ganymede's core: A deep-seated dynamo below a stable snow zone. *J. Geophys. Res.*, **120**. 182

SHAMPINE, L.F., KIERZENKA, J. & REICHELT, M.W. (2000). Solving boundary value problems for ordinary differential equations in MATLAB with bvp4c. *Tutorial notes*, **2000**, 1–27. 102

SHEN, G., PRAKAPENKA, V.B., RIVERS, M.L. & SUTTON, S.R. (2004). Structure of liquid iron at pressures up to 58 GPa. *Physical Review Letters*, **92**, 185701. xv, 7, 8

SHIMIZU, H., POIRIER, J. & LE MOUËL, J. (2005). On crystallization at the inner core boundary. *Physics of the Earth and Planetary Interiors*, **151**, 37–51. 22

SOLA, E., BRODHOLT, J.P. & ALFÈ, D. (2009). Equation of state of hexagonal closed packed iron under Earth's core conditions from quantum Monte Carlo calculations. *Phys. Rev. B*, **79**, 024107. xv, 7, 8

SOLOMATOV, V.S. (2007). Magma oceans and primordial mantle differentiation. *Treatise on geophysics*, **9**, 91–120. 60

SONG, X. & HELMBERGER, D.V. (1995). Depth dependence of anisotropy of Earth's inner core. *Journal of Geophysical Research: Solid Earth*, **100**, 9805–9816. 16

SOURIAU, A. & POUPINET, G. (1991). The velocity profile at the base of the liquid core from PKP(BC+Cdiff) data: an argument in favor of radial inhomogeneity. *Geophys. Res. Lett.*, **18**, 2023–2026. xvi, 14, 16, 17, 28

STACEY, F. & ANDERSON, O. (2001). Electrical and thermal conductivities of Fe-Ni-Si alloy under core conditions. *Phys. Earth Planet. Int.*, **124**, 153–162. 9

STACEY, F. & DAVIS, P. (2008). Physics of the Earth (Cambridge). 18, 20, 89

STACEY, F. & LOPER, D. (2007). A revised estimate of the conductivity of iron alloy at high pressure and implications for the core energy balance. *Phys. Earth Planet. Int.*, **161**, 13–18. 9

STORCHAK, D.A., SCHWEITZER, J. & BORMANN, P. (2003). The IASPEI standard seismic phase list. *Seismological Research Letters*, **74**, 761–772. 14

SUMITA, I., YOSHIDA, S., KUMAZAWA, M. & HAMANO, Y. (1996). A model for sedimentary compaction of a viscous medium and its application to inner-core growth. *Geophysical Journal International*, **124**, 502–524. 81

TARDUNO, J., COTTRELL, R., WATKEYS, M., HOFMANN, A., DOUBROVINE, P., MAMAJEK, E., LIU, D., SIBECK, D., NEUKIRCH, L. & USUI, Y. (2010). Geodynamo, solar wind, and magnetopause 3.4 to 3.45 billion years ago. *Science*, **327**, 1238–1240. 3

TKALČIĆ, H., KENNETT, B. & CORMIER, V. (2009). On the inner–outer core density contrast from PKiKP/PcP amplitude ratios and uncertainties caused by seismic noise. *Geophys. J. Int.*, **179**, 425–443. 11

TURNER, J. (1973). *Buoyancy effects in fluids*. Cambridge University Press. 46

UMEMOTO, K. & HIROSE, K. (2015). Liquid iron-hydrogen alloys at outer core conditions by first-principles calculations. *Geophysical Research Letters*, **42**, 7513–7520. 13

VOCADLO, L., POIRER, J. & PRICE, G. (2000). Grüneisen parameters and isothermal equations of state. *American Mineralogist*, **85**, 390–395. 142

WILLIAMS, Q. (2018). The thermal conductivity of Earth's core: A key geophysical parameter's constraints and uncertainties. *Annual Review of Earth and Planetary Sciences*. xv, 9, 10, 28

WILLIAMS, Q., JEANLOZ, R., BASS, J., SVENDSEN, B. & AHRENS, T.J. (1987). The melting curve of iron to 250 gigapascals: A constraint on the temperature at Earth's center. *Science*, **236**, 181–182. xv, 7, 8

YOO, C., HOLMES, N., ROSS, M., WEBB, D.J. & PIKE, C. (1993). Shock temperatures and melting of iron at Earth core conditions. *Physical Review Letters*, **70**, 3931. xv, 7, 8

ZOU, Z., KOPER, K. & CORMIER, V. (2008). The structure of the base of the outer core inferred from seismic waves diffracted around the inner core. *J. Geophys. Res.*, **113**, B05314. 16, 22, 28